Use of CO_2 Foam to Increase CO_2 Storage and Oil Recovery for CCUS

Master Thesis in Reservoir Physics

By

Amalie Rott Ellingsen

Department of Physics and Technology

University of Bergen

June 2022

Summary

CCUS (Carbon Capture, Utilization, and Storage) plays an essential role in mitigating climate change and reducing the emission of greenhouse gas (GHG). A major part of CCUS is combined CO2 enhanced oil recovery (EOR) and CO2 storage in geological formations. Implementation of CO_2 EOR with combined CO_2 Storage makes it possible to increase oil recovery and simultaneously store anthropogenic CO_2. However, injection of CO_2 can suffer from poor sweep efficiency due to high CO_2 mobility compared to reservoir fluids resulting in limited oil recovery and CO_2 storage potential. Application CO_2 foam can reduce CO_2 mobility, which could improve sweep efficiency, oil recovery, and CO_2 storage potentials.

This thesis reports a combination of core-scale experimental work and field-scale numerical simulations investigating the use of CO_2 foam mobility control in CO_2 EOR and CO_2 storage. The main objectives were to identify foaming solutions which generated strong foam and implement them with various injection strategies for increasing oil recovery and CO_2 retention. Foam generation and propagation were also investigated with in-situ visualization by PET/CT imaging. The experimental work consisted of three parts: steady-state foam quality and rate scans, CO_2 EOR and CO_2 Storage core floods, and in-situ imaging of foam flow. The numerical simulation work included field-scale sensitivity studies on the impact of injection strategy on foam generation, oil recovery, and CO_2 retention.

Steady-state foam quality and rate scans investigated CO_2 foam strength at different gas fractions and injection rates for foaming solutions with surfactant and a combination of surfactant and nanoparticles. The strongest foam was generated for the foaming solution with surfactant alone, and nanoparticles did not improve foam strength when added to foaming solution with surfactant. The optimal gas fraction was in the same range for all the tested foam systems and was not affected by the presence of nanoparticles.

Unsteady-state CO_2 and surfactant injections were performed to investigate oil recovery and CO_2 retention for different injection strategies on the core scale. Alternating aqueous and CO_2 injections were performed both as a single cycle and by rapidly alternating cycles. All injections with surfactant generated foam, with the highest oil recovery being 84% and 71% CO_2 retention for rapidly alternating injection. Stronger foam with higher apparent viscosity increased CO_2 retention but had little effect on oil recovery.

In-situ imaging from PET/CT was also conducted to investigate foam generation and determine the difference in CO_2 propagation into cores saturated with foaming solution or brine. Generation of CO_2 foam reduced CO_2 mobility for improved sweep efficiency compared to pure CO_2 injection. The CO_2 displacement front with foam was more stable and displaced more liquid compared to experiments without foam.

Field-scale numerical simulations of different injection strategies were performed to investigate the effect of injection strategy on oil recovery and CO_2 retention. Foam improved both oil recovery and CO_2 retention through increased CO_2 mobility control, independent of injection strategy. The rapid SAG injection scheme showed the largest increase in oil recovery and CO_2 retention.

Acknowledgments

First of all, I would like to express my gratitude to my supervisors, Dr. Zachary Paul Alcorn and Professor Arne Graue, for the opportunity to be a part of this research project. Thank you, Zach, for your excellent guidance, positivity, and valuable discussions. Thank you, Arne, for all your contributions to the Reservoir Physics group, for motivation and guidance.

I would also like to thank Dr. Bergit Brattekås for assistance with experimental work and guidance along the way. Thanks to Dr. Jaquelin Cobos Mora for valuable discussions and feedback.

A special thanks to my lab partner, Ph.D. Aleksandra Sæle, for willingly sharing knowledge and for collaboration on laboratory work. The endless hours spent in the lab this last year would not have been the same without you.

I would also like to thank all my friends and fellow students for contributing to five fun and memorable years at the University of Bergen.

Finally, I would like to thank my family for endless support and for always believing in me.

Bergen, June 2022

AmalieR Ellingsen

Table of Contents

Summary III

Acknowledgments V

Table of Contents VI

Part I. Introduction and Theory 2

1 Introduction 3

2 Fundamentals of Reservoir Engineering 5

2.1 Relative Permeability and Wettability 5

2.2 Capillary Pressure 6

2.3 Stages of Oil Recovery 7

2.4 CO_2 for Enhanced Oil Recovery 8

3 CCUS (Carbon Capture, Utilization, and Storage) 9

3.1 CO_2 Properties 9

3.2 Miscible Displacement/ Miscibility 10

3.3 Diffusion and Dispersion 11

3.4 Oil Swelling 12

3.5 CO_2 Storage 12

3.6 CO_2 Mobility Control 14

4 Foam 16

4.1 Foam Characteristics 16

4.2 Foam Generation 18

4.3 Foam Stability 20

4.4 Surfactants as Foaming Agents 21

4.5 Nano Particles in Foam 21

4.6 Foam Modelling 22

5 In Situ Imaging 23

5.1 Computed Tomography (CT) imaging 23

5.2 Positron Emission Tomography (PET) imaging 24

6 Reservoir Simulation 25

6.1 Fundamental Principles 25

6.2 Basic Equations 25

6.3 Foam modeling in ECLIPSE 26

Part II. Experimental and Numerical Procedures 28

7 Experimental Procedures 29

7.1 Preparation and Core Material 29

7.2 Cleaning and Preparation Procedure 29

7.3 Fluid Properties 30

7.4 Experimental Set-Ups 31

7.5 Steady-State Foam Quality and Rate Scans 36

7.6 Unsteady State EOR and CO_2 Storage Experiments 37

7.7 In-Situ Imaging Experiments 39

7.8 Experimental Overview 42

8 Numerical Modelling Methods 43

8.1 Model Description 43

8.2 Fluids in the Model 44

8.3 Foam Modeling 47

8.4 Injection Strategies 49

Part III. Results and Discussion 51

9 Steady-State Co-Injections – Foam Quality and Rate Scans 52

9.1 Baseline - Without Foaming Agent 52

9.2 Surfactant Stabilized Foam 54

9.3 Surfactant and Nanoparticle Stabilized Foam 57

9.4 The Effect of Injection Rate and Nanoparticles on Surfactant Stabilized Foam 59

10 Unsteady-State CO_2 EOR and CO_2 Storage 60

10.1 Single-Cycle WAG and SAG 60

10.2 Rapid WAG and SAG 63

10.3 The Effect of Injection Strategy and Surfactant Concentration on Oil Recovery and CO_2 Storage 66

11 In-Situ Imaging – Foam Generation and Propagation 69

11.1 Quantification of Core Properties with PET/CT 69

11.2 Baseline – Single-Cycle WAG 72

11.3 Single-Cycle SAG 74

11.4 The Effect of Surfactant on CO_2 Propagation 76

12 Numerical Simulation – Injection Strategy Sensitivity 77

12.1 Base Case – Rapid WAG and SAG 77

12.2 Single-Cycle WAG and SAG 82

12.3 Co-Injection of Aqueous Phase and CO_2 86

12.4 The Effect of Injection Strategy 90

13 From Core to Field Scale – Observations and Reflections 92

Part IV. Conclusions and Future Work 93

14 Conclusions 94

15 Future Work 96

Part V. Nomenclature, Abbreviations, References and Appendix 97

Nomenclature 98

Abbreviations 99

References 100

Appendix 104

A. Differential Pressure Development During WAG and SAG Injection 104

B. Pressure Fluctuations During Steady-State Co-Injection 105

C. Numerical Simulation File – Co-injection of Surfactant and CO_2 105

Part I. Introduction and Theory

1 Introduction

In a world where the energy demand is constantly increasing alongside increased anthropogenic greenhouse gas (GHG) emissions, measures must be taken to reduce the effect of climate change. Immediate action must be taken to comply with the long-term 1.5°C temperature goal set in the Paris Agreement and restrict global warming (Skea et al., 2022). The energy sector is a major contributor to GHG emissions. The International Energy Agency has advocated efforts to reach net-zero CO_2 emissions by 2050, and countries and companies are starting to follow up (Bouckaert et al., 2021). Development of renewable energy sources and improvement to the current petroleum industry must be completed to mitigate climate change and reduce greenhouse gas emissions.

Carbon Capture and Storage (CCS) enables the use of hydrocarbons as an energy source and still complies with the goals set for reduced emissions (Skea et al., 2022). The capture of anthropogenic CO_2 and subsurface storage has been performed since the 1970s with success. In 1996 Statoil established a CO_2 storage project at the Sleipner field in the Utsira formation on the Norwegian Continental Shelf, which is still ongoing today (Eiken et al., 2011). Many CCS projects are needed to reach net-zero by 2050, but the projects are very costly. Therefore, to improve the feasibility of large-scale CO_2 storage for the industry and create revenue, utilization of the captured CO_2 is necessary.

Implementation of CCUS can offset the large costs of CCS by providing a revenue to the industry in the form on increased hydrocarbon production. In this context CCUS involves capture of anthropogenic CO_2, transportation, and injection of CO_2 foam into mature oilfields for CO_2 storage and increased oil production. CO_2 can improve oil recovery by oil swelling and obtaining miscibility with the oil (Grogan & Pinczewski, 1987; Skjæveland & Kleppe, 1992). However, a major challenge with CO_2 injection is the low density and viscosity of CO_2, compared to reservoir fluids. These adverse CO_2 properties can result in viscous fingering and gravity override, often leading to poor sweep efficiency and rapid CO_2 breakthrough (Zolotukhin & Ursin, 2000). However, improved CO_2 mobility control can increase oil recovery for increased revenue and CO_2 storage potential.

CO_2 mobility control can be realized through the generation of CO_2 foam. CO2 foam injection involves injecting CO_2 and a foaming agent, either simultaneously or in alternating slugs. However, foam is thermodynamically unstable and will collapse over time. The stability of foam can be significantly increased by foaming agents such as surfactants (Sheng, 2013). CO_2 foam has significantly higher viscosity than pure CO_2, which provides a more favorable mobility ratio for displacement of oil and water. When more oil is produced, the revenue increases, and when water production increases more space is available for CO_2 storage.

This thesis presents experimental and numerical work to investigate CO_2 foam for improved oil recovery and CO_2 retention. Foam strength was studied during steady-state co-injection experiments with non-ionic surfactant and nanoparticles at different concentrations and injection rates. Foam generation and propagation were determined by in-situ imaging techniques with PET/CT applied during injection of CO_2 with surfactant present. The effect of injection strategy was investigated for increased oil recovery and CO_2 retention, through core flooding experiments and numerical simulations, applying foaming solutions proven to generate strong foams.

2 Fundamentals of Reservoir Engineering

2.1 Relative Permeability and Wettability

Relative permeability describes the flow of a fluid in a porous media when more than one fluid is present. The concept relates to the absolute permeability of the media (K_a) and the effective permeability (k_{eff}) of a given fluid. If only one fluid is present, the effective permeability equals the absolute (William G. Anderson, 1987; Zolotukhin & Ursin, 2000). The relative permeability (k_r) is defined by Equation 2.1:

$$k_r = \frac{k_{eff}}{K_a} \tag{2.1}$$

Relative permeability largely depends on the porous media and properties of the flow, such as wettability, geometry, fluid saturation, and saturation history. The relative permeability of a fluid increases when its fraction increases (William G. Anderson, 1987). Figure 2.1 illustrates the relative permeability of oil and water for an oil-wet system in (a) and a water-wet system in (b). The relative permeability of the fluids increases with increased saturation. Given that the fluids in the system are immiscible, such as water and oil, the system will have irreducible and residual saturations. The residual saturations depend on the wettability of the system.

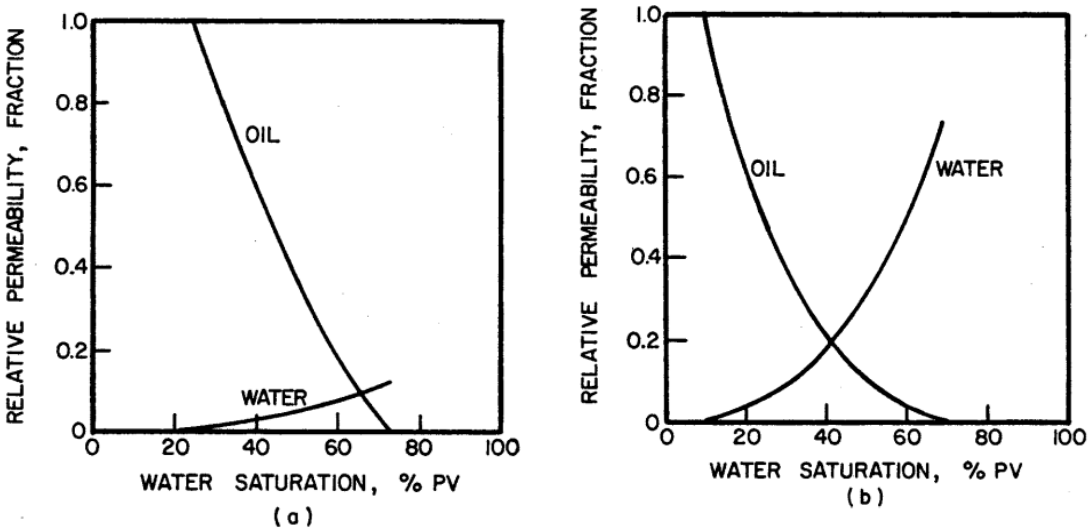

Figure (2.1) Relative permeability change for oil and water, based on increasing water saturation for a typical oil-wet (a) and water-wet (b) porous media (William G. Anderson, 1987).

When two immiscible fluids are present on a surface, the wettability is determined by which fluid adheres to the surface. The wetting phase adheres to the pore walls in a porous media, while the non-wetting phase repels from it and occupies the pores' center. Due to capillary forces, the wetting phase will enter the smallest pores where the capillary forces are large. The non-wetting phase will enter the largest pores first, where the threshold pressure is lowest. The fluid distribution due to wettability is essential to understanding the fluid flow in the system and the impact of electrical properties, capillary pressure, residual saturations, and oil recovery (Anderson, 1986).

2.2 Capillary Pressure

Capillary pressure is defined as the molecular pressure difference at the interface of two immiscible fluids (William G Anderson, 1987; Zolotukhin & Ursin, 2000). It depends on the system's wettability and is defined based on the fluids in the system. Given a water and oil system that is water-wet, the capillary pressure (P_C) is defined in Equation 2.2:

$$P_C = P_O - P_W \tag{2.2}$$

Where P_o and P_w are the pressures in the oil and water phase, respectively.

On a microscopic scale, such as a pore within a porous media, the capillary pressure is defined in Equation 2.3 as a relation between the interfacial tension (σ), wetting angle (θ), and the pore radius (r).

$$P_C = \frac{2\sigma \cdot \cos(\theta)}{r} \tag{2.3}$$

According to the definition of capillary pressure, Pc increases when the non-wetting phase replaces the wetting phase in a drainage process. The opposite happens when the wetting phase enters the system, and the capillary pressure declines during an imbibition process (William G Anderson, 1987). The capillary pressure curve for a water-wet system is presented in Figure 2.2. Curve 1 shows an increase in capillary pressure as the oil enters the system in a drainage process, and curve 2 shows spontaneous imbibition when the wetting phase displaces oil from the system.

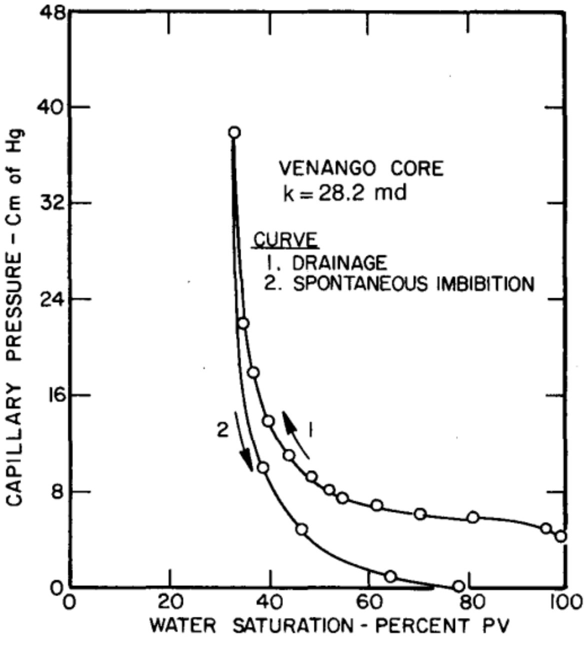

Figure 2.2 Capillary pressure curve for a strongly water-wet system shows drainage and spontaneous imbibition (William G Anderson, 1987).

2.3 Stages of Oil Recovery

The development of an oil field can be divided into three phases of production: primary, secondary, and tertiary. Primary production is from natural drive mechanisms, such as pressure depletion or water influx and usually recovers around 10%of the original oil in place (OOIP). Secondary production involves the injection of reservoir fluids, where water or gas injection is widely used. The expected oil recovery is between 20% and 40%of the OOIP before tertiary recovery. Tertiary recovery, often called enhanced oil recovery (EOR), is all recovery techniques applied after secondary recovery (Lake et al., 2014). EOR mobilizes remaining oil by injection of fluids or materials that are not naturally present in the system. EOR methods aim to increase the reservoir's energy or interact with the fluid system to improve oil recovery. Improvements can be made both microscopically and macroscopically by reducing interfacial tension and capillary forces. In addition, methods for mobility control of injection fluids are commonly applied to improve sweep efficiency (Romero-Zerón, 2012). The tertiary recovery stage can increase oil production by up to 60% and, in some cases, even more (Energy.gov, 2022).

Most oil and gas production worldwide comes from mature fields, and there has been a significant decline in discoveries over the last decades. Therefore, EOR is essential to ensure that the world's energy demands are met (Alvarado & Manrique, 2010). Furthermore, increased oil recovery from developed resources benefits both companies and the environment by saving costly time and limiting emissions related to well-site construction, which requires large quantities of materials. Recently, there has been an increased focus on clean energy and reduction in emissions, especially related to CO_2. To reach the 1.5-degree goal from the Paris Agreement, the CO_2 emissions must be reduced significantly, and EOR could be a part of the solution.

A wide range of EOR methods exists, and some are used commercially. These methods can be divided into thermal, chemical, and gas methods. A commonly used thermal method is a steam injection to produce heavy oil by breakage into smaller components to ease production. Moreover, gas injection can be either a miscible or immiscible displacement method, dependent on the gas used, but usually have poor sweep efficiency due to an unfavorable mobility ratio of the injected gas to reservoir fluids. Chemical EOR methods target the volumetric and areal sweep (Alvarado & Manrique, 2010). Injection of water-soluble polymers, the viscosity of the water that displaces the oil is increased, and the relative permeability of the water is reduced. Polymers improve the mobility ratio and can block high permeable streaks with water channeling. A disadvantage of polymers is that they permanently impact the reservoir, and thereby cause permanent changes, or damage, to the system. Surfactants reduce the interfacial tension between oil and water, enabling capillary trapped oil droplets to mobilize for production (Zolotukhin & Ursin, 2000). CO_2 foam injection has similar abilities to gas and chemical EOR methods and will be further discussed in chapter 2.4 and has been experimentally and numerically investigated in this thesis.

2.4 CO_2 for Enhanced Oil Recovery

Since the early 1970s, CO_2 injection has increased oil recovery from mature oil reservoirs. When CO_2 pipelines were installed in the Permian basin in the 1980s, the supply and demand proliferated. In the late 1980s, the method increased residual oil recovery in a range of pilot tests both at miscible and immiscible conditions (Brock & Bryan, 1989). Over the years, CO_2 flooding has been applied as an EOR method in many projects in various geological formations and rock types. An EOR screening conducted by Al Adasani and Bai in 2010 indicated that miscible CO_2 injection is the second most used method in 652 independent EOR projects worldwide (Al Adasani & Bai, 2011).

Gas injection with CO_2 has many advantages in field applications. Due to oil swelling, CO_2 can mobilize capillary trapped oil and improve the microscopic sweep efficiency (Grogan & Pinczewski, 1987). CO_2 can displace a significant amount of residual oil, theoretically 100% at miscible conditions, due to its miscibility with the reservoir oil. CO_2 reduces the oil viscosity and could result in favorable mobility conditions for increased oil displacement. (Skjæveland & Kleppe, 1992; Verma, 2015). However, CO_2 injection can lead to production problems such as corrosion and leaks. Also, precipitation of heavy hydrocarbon components due to a vaporization process between the CO_2 and oil can cause production problems (Skjæveland & Kleppe, 1992). Challenges arise with CO_2 injection due to the low viscosity and high mobility of CO_2 at reservoir conditions. The sweep efficiency is often poor because of gravitational instability due to viscous fingering and reservoir heterogeneity (Zolotukhin & Ursin, 2000). A typical CO_2 injection process consists of alternating slugs of CO_2 and water (Figure 2.3).

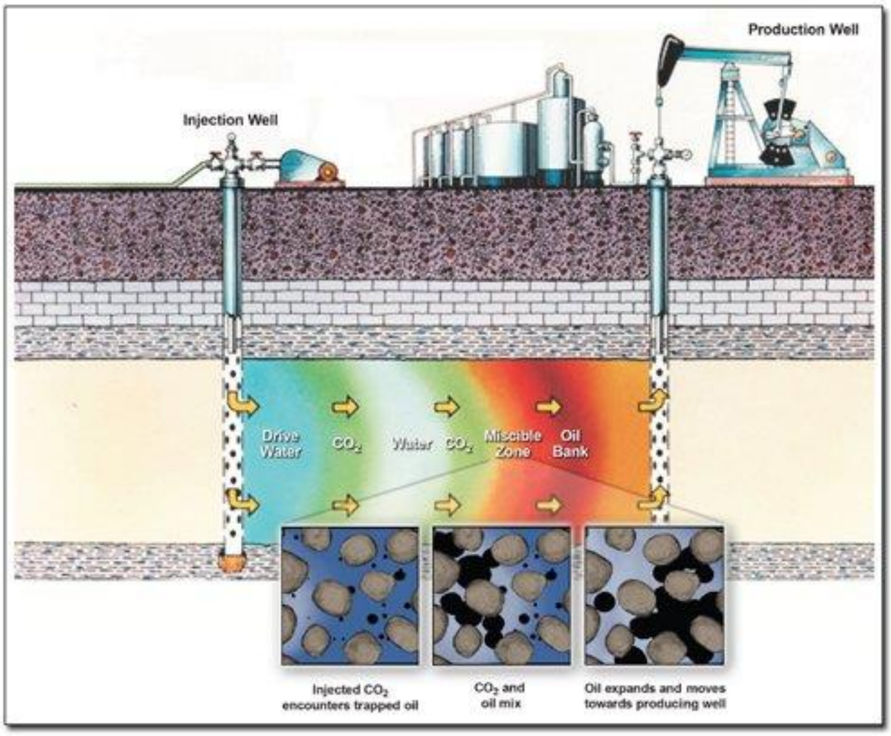

Figure 2.3 Cross-section illustration of CO_2 in enhanced oil recovery on the field and pore-scale where CO_2 and water is injected in alternating slugs (Energy.gov, 2022).

3 CCUS (Carbon Capture, Utilization, and Storage)

3.1 CO_2 Properties

Carbon dioxide is a chemical compound present in the atmosphere in low concentrations. It is a natural part of the carbon cycle, both in biological processes like photosynthesis and from sources like volcanic activity. CO_2 is in the gaseous phase at ambient conditions, but it becomes a solid, liquid, or supercritical fluid with increased pressure and temperature, dependent on the conditions (Freund et al., 2005). The phase changes for pure CO_2 are shown in Figure 3.1 based on the pressure versus temperature changes.

Under supercritical conditions, the temperature and pressure are above the substance's supercritical value. Gas cannot be separated from the liquid, and the fluid has properties from both states (Sihvonen et al., 1999). At reservoir conditions, CO_2 is often supercritical given sufficient pressure and temperature. The phase diagram for CO_2, including supercritical conditions, is illustrated in Figure 3.1. Given supercritical conditions, the viscosity and density of CO_2 are high compared to other gases, which is favorable for increased front stability and can reduce viscous fingering to some degree (Lee & Kam, 2013). At supercritical conditions, CO_2 can often obtain miscible conditions with the reservoir fluids and lessen the capillary entrapment of oil. CO_2 can then reduce the residual oil saturation and theoretically displace all the oil in the system (Lee & Kam, 2013).

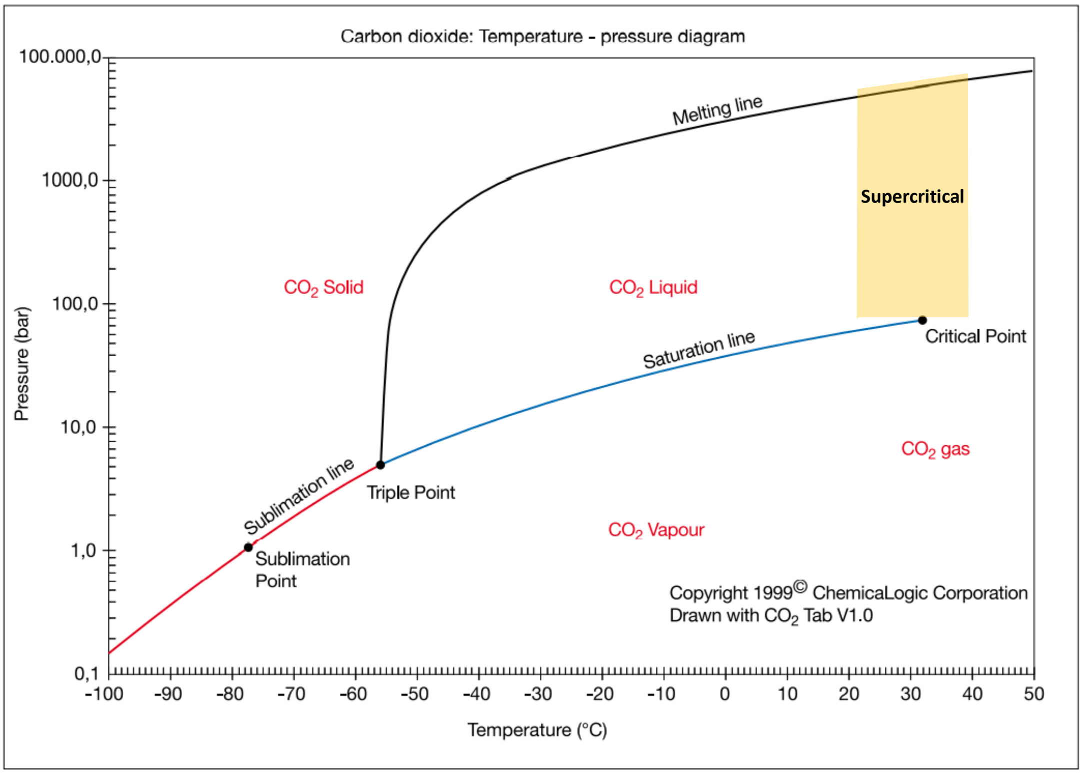

Figure 3.1 CO_2 phase diagram illustrating state based on temperature and pressure(Freund et al., 2005).

3.2 Miscible Displacement/ Miscibility

Miscibility is when two fluids completely mix and become a homogenous phase, where it is impossible to distinguish between the fluids, and there is no interfacial tension between them (Holm, 1986). In theory, a miscible CO_2 displacement can recover 100% of the oil in the system. However, heterogeneity and instabilities often cause a substantial volume of hydrocarbons to remain in the reservoir after the displacement. Viscous fingering and water shielding result in unswept areas where the solvent cannot reach the remaining oil. In water-wet systems, the water film along the pore walls will result in many capillary trapped oil droplets easily bypassed by the solvent. Capillary trapped oil is especially an issue in tertiary recovery due to significant water saturations, which lead to increased water blocking (Muller & Lake, 1991). In the case of immiscible displacements, such as water displacing oil, the capillary forces in the system will lead to irreducible saturation due to bypassed oil and snap-off, which result in capillary entrapped oil droplets (Holm, 1986).

Miscibility between substances can be either first-contact or multi-contact miscible. First-contact miscible compounds mix with initial contact. Multi-contact miscibility work by two mechanisms, vaporizing- and condensing gas drive. Both methods consist of transferring components from one fluid to the other. Vaporizing gas drive is the injection of gas with light components that vaporize light components in the reservoir oil as it moves through the reservoir. After some time, the gas will become miscible with the remaining oil and become a miscible displacement front (Holm, 1986).

On the contrary, a condensing gas drive consists of an enriched gas consisting of hydrocarbon molecules with more than one carbon atom. Some of the components in the gas will dissolve in the oil and make the oil composition lighter. The new oil composition will become miscible with the pure injection gas (Holm, 1986).

To obtain miscibility, the pressure in the system must be higher than the minimum miscibility pressure (MMP) for gas to develop miscibility with the fluids in the system (Song et al., 2011). This thesis's experimental work uses the mineral oil n-decane as the oil phase. For a CO_2 and n-Decane slim tube system, the MMP is reported to be 8.2-6.6 mPa, equivalent to 82-86 bar, at 37.8°C (Song et al., 2011). The MMP depends on temperature, which is presented in Figure 3.2.

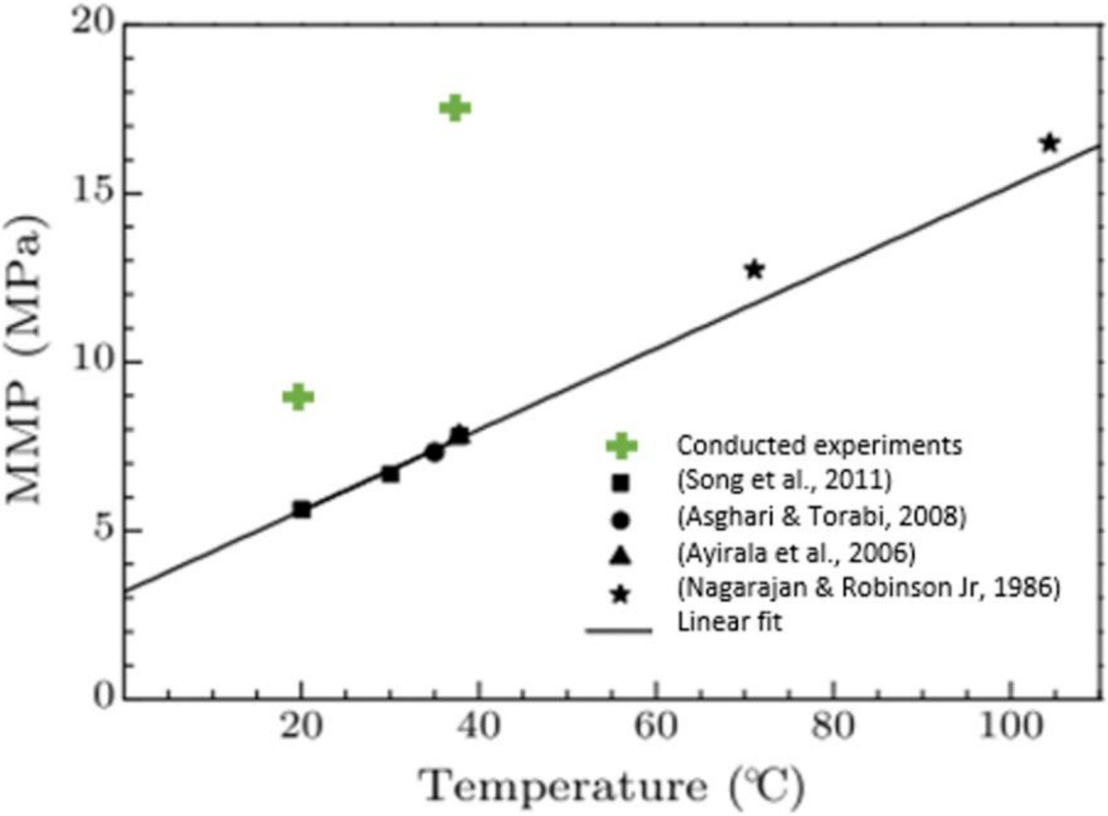

Figure 3.2 Measured minimum miscibility pressure for n-decane and CO_2 under different experimental conditions (Asghari & Torabi, 2008; Ayirala et al., 2006; Nagarajan & Robinson Jr, 1986; Song et al., 2011). The experimental conditions used in this thesis are marked green and called conducted experiments on the figure.

3.3 Diffusion and Dispersion

Diffusion and dispersion are essential to understanding a miscible displacement. Diffusion is the process that spontaneously occurs on the surface between two miscible fluids. Due to molecular movements, the fluids will mix on the interface and create a diffuse border, or mixing zone, between them (Perkins & Johnston, 1963). Diffusion occurs in gas, liquid, and dense phases, where dense phases include supercritical fluids. The process is vital in miscible displacement because it describes the mixing between the fluids in the reservoir (Skjæveland & Kleppe, 1992). When fluid is in movement, dispersion causes additional mixing between fluids from diffusion and convection forces. Diffusion decreases the gradients that separate the fluids and work transversally to and in the flow direction. Dispersion is defined on all scales: microscopic, macroscopic to megascopic, or pore, core to the reservoir (Skjæveland & Kleppe, 1992).

3.4 Oil Swelling

Oil swelling occurs when gas is dissolved in oil, so the oil phase increases in size and obtains reduced viscosity. The swelling generates favorable conditions for increased oil production by improving the mobility ratio between oil and water and increasing the oil volume. In water-wet systems, the oil swelling is especially favorable because the relative permeability of the wetting phase is larger than for the non-wetting oil (Mungan, 1981). If the capillary trapped or stagnant oil is exposed to injected gas, diffusion will cause oil swelling (Figure 3.3). The swelling could be significant enough to mobilize the oil and increase oil production. The process consists of gas displacement by water that thins the water film along the pore walls. The thinning of the film has to be sufficient for gas to contact the oil over time to have oil mobilization. (Grogan & Pinczewski, 1987; Skjæveland & Kleppe, 1992).

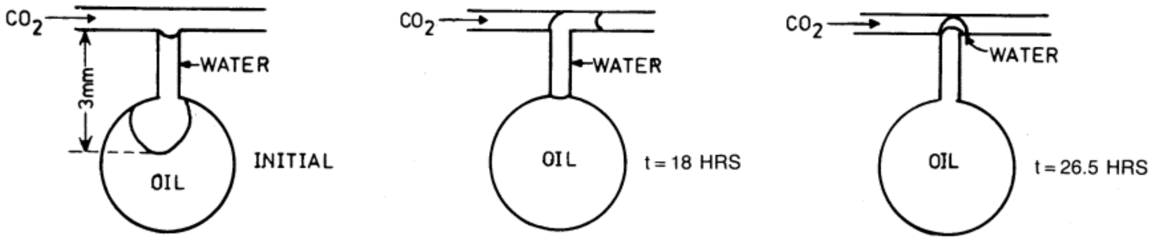

Figure 3.3 Oil swelling from CO_2 injection in a dead-end pore (Grogan & Pinczewski, 1987).

Oil swelling occurs when CO_2 gas is injected. Swelling is affected by oil composition, temperature, and pressure. The effect increases for high pressure and decreases with temperature, given that it is higher than the critical point (Mangalsingh & Jagai, 1996).

3.5 CO_2 Storage

Over the last decade, CO_2 storage has been widely discussed to sequester anthropogenic CO_2 and reduce emissions. Large measures must be taken to reach the global goals to limit CO_2 emissions set in the Paris Agreement (Heleen van Soest, 2018). CO_2 storage is a part of the solution, and quite a few pilot projects have been conducted or are under development. CO_2 storage has been performed with success since the 1970s. The first commercial CCS activity was conducted by Statoil (now Equinor) in 1996, storing CO_2 in the Utsira formation in the Sleipner field (Eiken et al., 2011). In 2024 the CCS project, named Longship, will be the first full-scale project ever conducted. CO_2 gas will be captured from a cement factory and permanently sequestered in the Utsira formation on the Norwegian continental shelf (Equinor, 2022).

CO_2 storage in geological formations depends on four trapping mechanisms (Figure 3.4): structural and stratigraphic, residual, solubility, and mineral trapping. The mechanisms are time-dependent and consist of mechanical and chemical trapping (Metz et al., 2005). Directly after CO_2 injection, structural and stratigraphic trapping is the dominant mechanism where CO_2 gets trapped by impermeable seals or caprocks. Capillary forces govern residual trapping within the pore network resulting in the immobilization of dispersed CO_2. Moreover, the CO2 will dissolve during dissolution trapping in the in-situ water phase. This process is rapid when CO_2 and water occupy the same pore space. With time chemical reactions between the dissolved CO_2 and rock minerals result in mineral trapping. However, the process is prolonged and can take thousands of years (Metz et al., 2005).

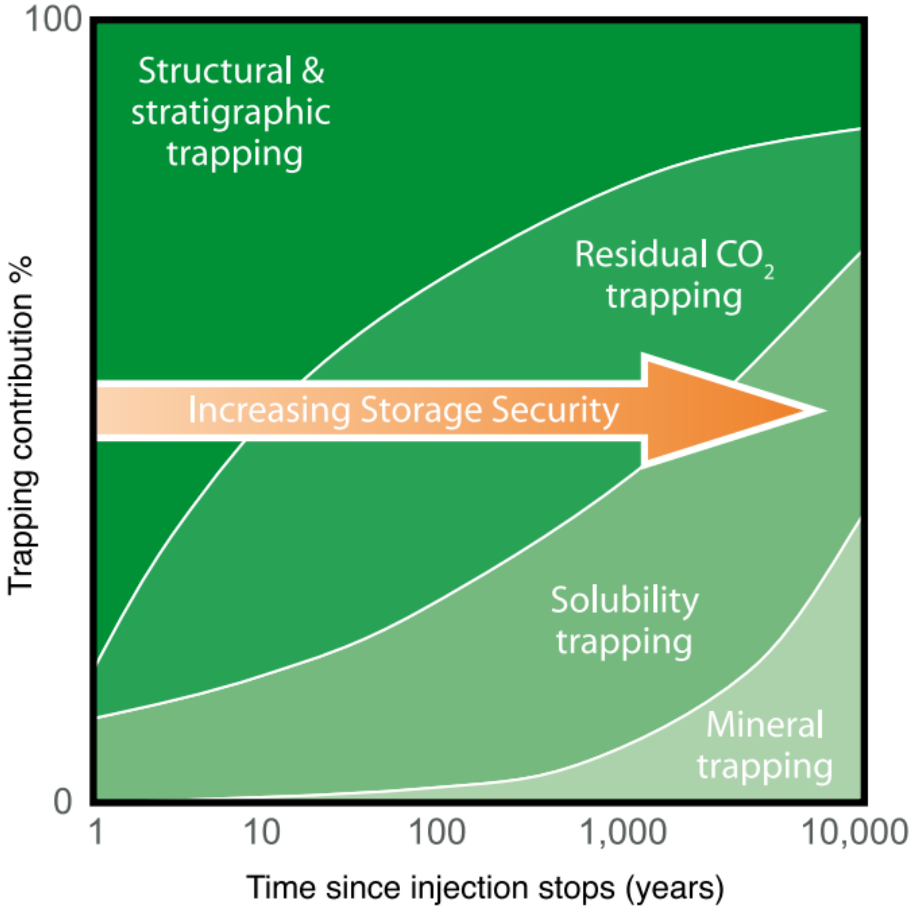

Figure 3.4 Trapping contribution as a function of time since injection for CO_2 trapping mechanisms in an underground aquifer (Metz et al., 2005).

In joint EOR and CO_2 storage projects, CO_2 retention determines how much CO_2 is stored in the reservoir. CO_2 storage can be calculated if the purchased volume of CO_2 is known. The exact volume must be known to determine the amount of lost CO_2, but the operators do not disclose the purchased volumes due to confidentiality agreements on the sale of CO_2 (Melzer, 2012). Therefore, CO_2 retention instead estimates how much of the injected CO_2 remains in the subsurface (Azzolina et al., 2015). The retention can be calculated for all cases where CO_2 is injected, and the volumes injected and produced are known. The CO_2 retention factor ranges from 0 to 1, where one is equal to 100% CO_2 storage (Melzer, 2012). It is defined by CO_2 volume (V_{CO_2}) that is injected and produced:

$$(3.1) \qquad CO_2 retention = \frac{V_{CO_2} injected - V_{CO_2}\, produced}{V_{CO_2} injected}$$

3.6 CO_2 Mobility Control

CO_2 has been used for EOR purposes for more than 50 years. However, pure CO_2 injection can result in poor sweep efficiency. Phenomena like viscous fingering and gravity override can occur due to the high mobility of CO_2 compared to reservoir fluids at reservoir conditions. Increased displacement stability is obtained by injection strategies such as water alternation gas (WAG) or adding foams, thickeners, or gels to the injection fluids (Enick et al., 2012). The most commonly used CO_2 mobility reduction method is WAG, which has been used for decades. Injection of alternating CO_2 and water slugs causes the saturation of CO_2 to decrease in the pore space due to the presence of water. As a result, the relative permeability of CO_2 is reduced, although the viscosity remains low and mobility high. WAG processes typically displace between 35% to 65% of the original oil in place (OOIP) (Enick et al., 2012).

The objective of polymer thickeners is to increase the viscosity of a fluid by direct dissolution in fluids. Unfortunately, the structure of the CO_2 molecules makes it a poor solvent. However, liquid or supercritical CO_2 systems have shown success in the lab but have not been implemented on the field scale (Enick et al., 2012). Water-soluble polymers have been implemented in many field-scale projects. Polymers are used to improve the mobility ratio by increasing the viscosity of the displacing phase, thereby improving the sweep efficiency and reducing viscous fingering. The polymer also agglomerates in high permeability streaks, diverting flow to other reservoir parts (Green & Willhite, 1998). Using water-soluble thickeners with CO_2 could enable CO_2 to contact a larger reservoir volume, increasing the sweep efficiency. A disadvantage of polymers is that they absorb in the formation and often cause a permanent reduction in the effective permeability (Green & Willhite, 1998).

Foams have similar advantages to polymers and are usually implemented as a surfactant-alternating gas (SAG) injection strategy. Foam generation is largest in high permeable layers with low oil saturation, resulting in the diversion of flow to lower permeable zones (Rossen, 1996). The foam also reduces the interfacial tension between oil and water because of the surfactant in the water solution, which improves the microscopic sweep efficiency (Farajzadeh et al., 2012). In addition, the displacement front is more stable with foam because the high apparent viscosity of foam develops a more favorable mobility ratio than pure gas injection (Figure 3.5). A more detailed description of foam behavior is included in Chapter 4.

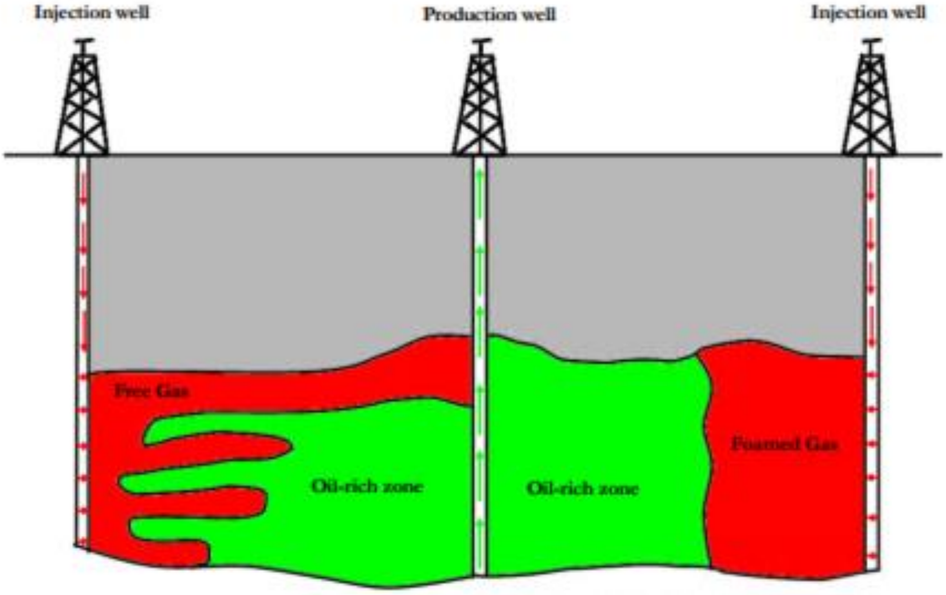
Injection well
Production well
Injection well
Free Gas
Oil-rich zone
Oil-rich zone
Foamed Gas

Figure 3.5 Schematic of free gas injection (a) dominated by gravity override and viscous fingering and foamed gas injection (b) with a piston-shaped displacement due to mobility reduction of CO_2 (Farajzadeh et al., 2012).

4 Foam

4.1 Foam Characteristics

Foam is an agglomeration of gas bubbles where a thin liquid film separates gas bubbles (Bikerman, 2013). It can be described as a gas dispersion in a liquid, where gas is separated by a continuous liquid film called lamellae (Figure 4.1) (Schramm, 1994). Foam is thermodynamically unstable, and the foam will collapse over time. Foam stability is defined regarding kinetics and depends on the foam composition and outside factors that affect the foam (Sheng, 2013). Foaming agents, such as surfactants, are used to increase foam stability. Due to the large surface area of a bubble, the surface tension is high and will cause the foam to break down. Foaming agents like surfactants increase foam stability by reducing the surface tension between the gas and the lamellae (Schramm, 1994).

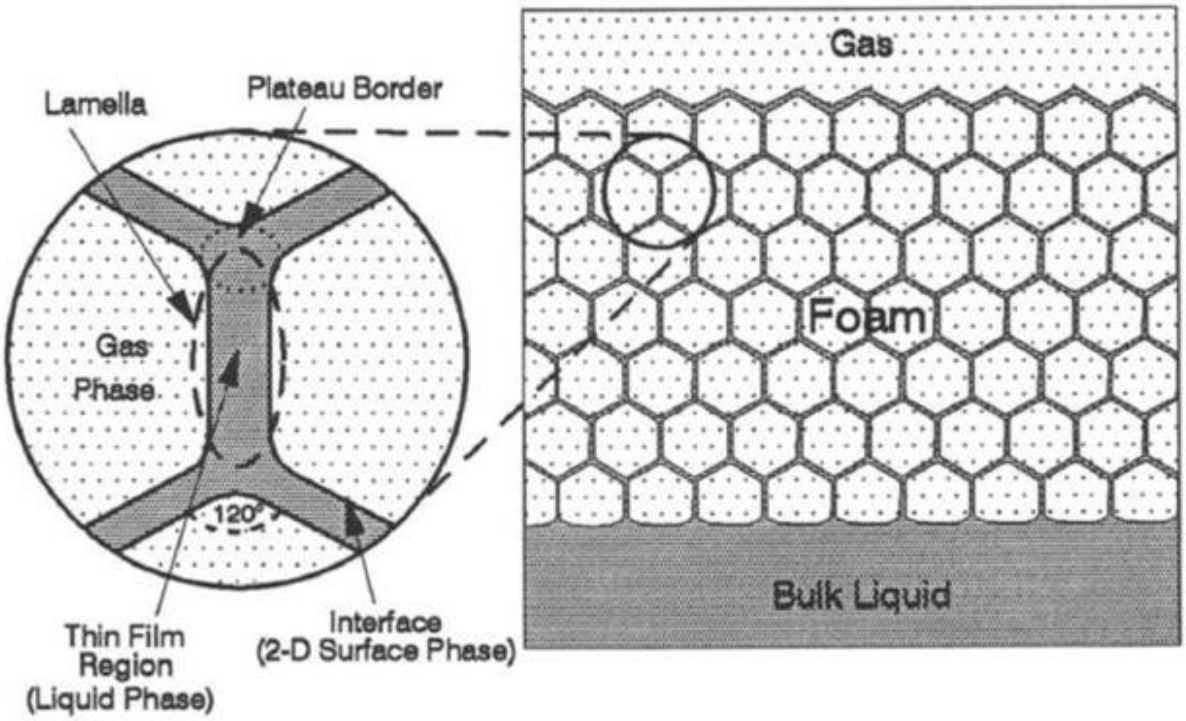
Lamella
Plateau Border
Gas Phase
120°
Thin Film Region (Liquid Phase)
Interface (2-D Surface Phase)
Gas
Foam
Bulk Liquid

Figure (4.1) Idealized two-dimensional illustration of foam. (Schramm, 1994)

A range of mathematical descriptions can be used to quantify foam characteristics. This thesis evaluated foam based on foam quality to separate water-gas fraction and apparent viscosity to describe foam strength.

Gas Fraction or Foam Quality

Gas fraction (or foam quality) is the fraction of gas to the total amount of gas and liquid in a foam (Equation 4.1). With increasing gas fraction, foam transitions from low to high quality (Farajzadeh et al., 2012). The high-quality foam regime describes high gas fractions where the foam strength decreases with an increasing gas fraction (Boeije & Rossen, 2013). The foam quality is closely related to foam texture or bubble size, and high foam quality results in larger bubbles, which reduce the foam strength(Sheng, 2013).

$$(4.1) \qquad f_{gas} = \frac{q_{gas}}{q_{gas} + q_{liquid}}$$

Where f_{gas} is the gas fraction, (q_{gas}) is gas flow rate and $\left(q_{liquid}\right)$ is liquid flow rate.

Apparent Viscosity

Apparent viscosity is used to quantify foam strength in laboratory experiments. It describes the relationship between the flow rate and the pressure drop of foam through a capillary (Hirasaki & Lawson, 1985). High apparent viscosity indicates strong foam. Given a sufficiently high-pressure gradient, the apparent viscosity (μ_{APPV}) can be defined by Darcy's law (Equation 4.2) (Falls et al., 1989):

$$(4.2) \qquad \mu_{APPV} = \frac{KA\Delta P}{QL}$$

Where K is permeability, A is the cross-sectional area, ΔP is the pressure gradient. Q is the flow rate, and L is the length.

4.2 Foam Generation

In porous media, foam can be generated by both co-injection of gas and foaming solution and alternating injection of aqueous solution and gas (Farajzadeh et al., 2012). Three main mechanisms generate foam; snap-off, lamella leave behind, and lamella division (Ransohoff & Radke, 1988). Figures 4.2-4.4 illustrate the different mechanisms for foam generation in porous media.

Leave-behind occurs when gas enters an adjacent pore body from two directions (Rossen, 1996). The two gas fronts squeeze the liquid present between them until it becomes a thin liquid film, lamellae. Leave-behind dominates foam generation at low velocities and frequently occurs in well-interconnected pore networks. The foam generated is often weak and does not form separate bubbles (Ransohoff & Radke, 1988). Foam is only generated from leave-behind at high water saturations and remains in a continuous phase with high mobility. The foam generated by leave-behind often ruptures during drainage due to the high gas mobility.

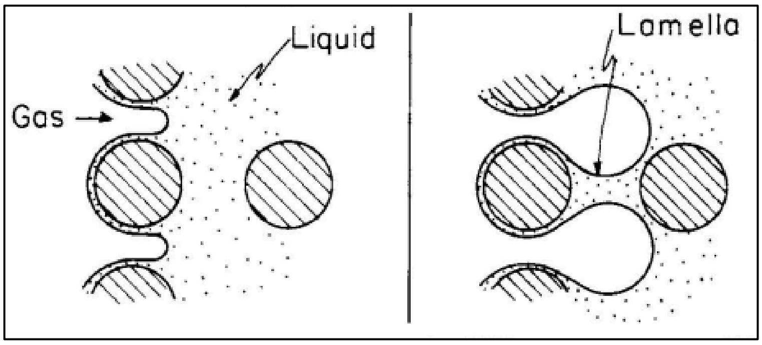

Figure 4.2 Foam generation by leave-behind (Ransohoff & Radke, 1988).

The dominant mechanism for foam generation in porous media is snap-off (Figure 4.3). Snap-off occurs when gas penetrates a pore throat, followed by a rapid capillary pressure drop (Ransohoff & Radke, 1988; Schramm, 1994). Due to capillary forces, the wetting phase has a strong presence in small and narrow pores, promoting pressure drops to displace the gas from the pore throat. As a result, the generated gas bubbles are isolated, significantly reducing gas mobility. During drainage, snap-off also occurs if liquid moves against the flow direction from a large pore to a smaller pore throat. A bubble will then be created in the pore connected to the narrow pore throat. (Rossen, 1996).

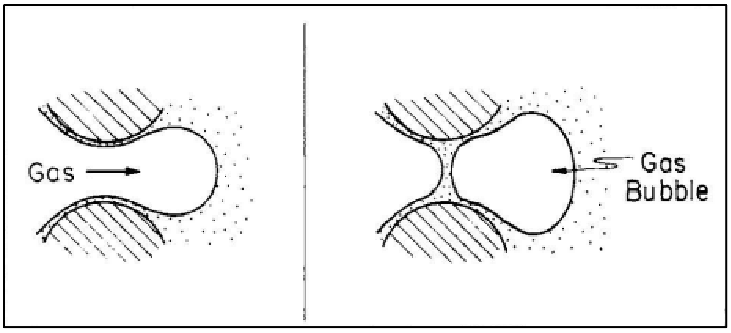

Figure 4.3 Foam generation by snap-off (Ransohoff & Radke, 1988).

The third mechanism of foam generation is lamellae division (Figure 4.4), which describes foam created from existing lamellae. When a gas bubble approaches a pore with more than one pore throat, the lamella will stretch and divide into more lamellae creating new bubbles. The mechanism works similar to snap-off, and the bubble created either continues to propagate or stays behind as a blockage (Ransohoff & Radke, 1988; Rossen, 1996).

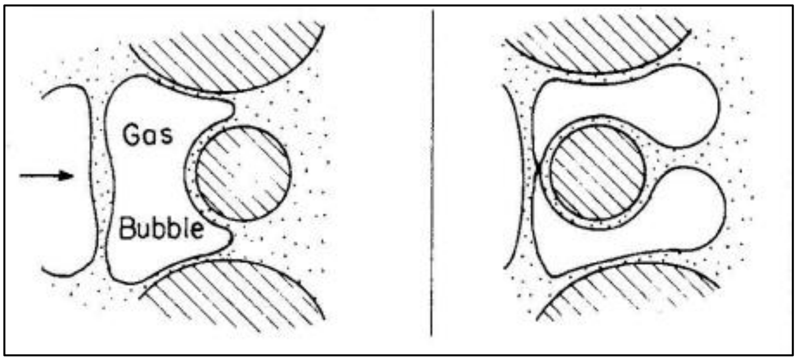

Figure 4.4 Foam generation by lamellae division (Ransohoff & Radke, 1988).

4.3 Foam Stability

The stability of foam can be described as the ability to withstand the coalescence and collapse of the bubbles (Chambers, 1994). Foam is thermodynamically unstable, and bubbles are created and break down continuously over time (Wasan et al., 1994). Therefore, the foam stability depends on the stability of the lamellae and several external factors. Foam stability in porous media is primarily governed by factors such as permeability, pressure, temperature, and the presence of oil (Farajzadeh et al., 2012).

The Effect of Permeability

Foam is firstly generated in areas with high permeability because of the low capillary entry pressure (Khatib et al., 1988). Over time, the foam becomes fine-textured, less mobile, and diverts fluid flow to other reservoir regions. Most reservoirs are heterogeneous, and a lot are layered and consist of zones with permeability variations. Given sufficient foam generation in a high permeable zone, flow is diverted into areas with lower permeability, thereby increasing the volumetric sweep efficiency (Farajzadeh et al., 2012).

The Effect of Pressure and Temperature

The pressure and temperature are often higher at reservoir conditions than in ambient conditions. Increased pressures result in smaller bubbles and a more compact foam, which increases foam stability (Friedmann & Jensen, 1986). The reduction in bubble size means that a more significant part of the system consists of lamellae which reduces foam drainage. Very high pressures destabilize the foam and cause the foam to collapse. (Sheng, 2013). Solubility increases with increasing temperature, which results in more extensive dissolution of the foaming agent in the aqueous phase. As a result, fewer molecules are present on the gas-liquid interface, which reduces foam stability. Foaming agent must be present on the gas-liquid interface to lower interfacial tension. Increasing temperature, thereby decreasing the foam stability (Sheng, 2013).

The Effect of Oil

The effect of oil on foam is essential to understand when using foam in EOR applications. When oil contacts a foam composed of aqueous lamellae,

The effect of oil on foam composed of aqueous lamellae is essential for EOR applications. The oil destabilizes the foam and creates an unstable boundary between the phases (Sheng, 2013). Lighter oils that consist of shorter hydrocarbon molecules have a more significant destabilization effect on foam than heavier oil. The presence of the foaming agent can also create oil and water emulsions which can break down the foam (Rossen, 1996). The oil saturation must be lower than a critical value for the foam to generate in a system with oil present (Friedmann & Jensen, 1986). The generation of emulsions leads to mixing of formerly immiscible oil and gas phases. Emulsions can reduce the relative permeability of the water phase and increase the oil recovery. Like foam, it accumulates in the large pores and diverts flow to lower permeability areas in time, resulting in increased sweep efficiency (McAuliffe, 1973).

4.4 Surfactants as Foaming Agents

Surfactants are often used as foaming agents because of their stabilizing effect on the fluid interfaces and surfaces by reducing the interfacial tension between the phases. The molecules consist of a hydrophilic head and a hydrophobic tail (Figure 4.5) (Schramm & Marangoni, 2000). Surfactants occupy the interface between two fluids, like oil and water, with the head in the water phase and the tail in the oil phase. Thus, reducing the interfacial tension. Surfactants are divided into groups based on the electrical charge of the head and are either anionic (negative), cationic (positive), or nonionic (no charge)(Schramm & Marangoni, 2000). In foam, the surfactant molecules are present on the interface between the gas and lamellae, increasing its stability.

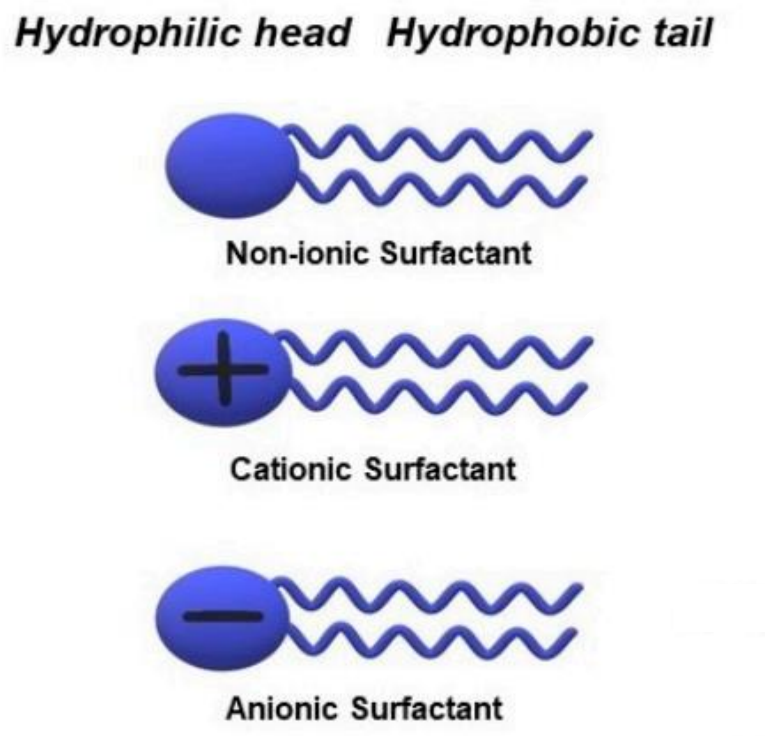

Figure 4.5 Surfactants with different surface charges (Soleimani Zohr Shiri et al., 2019).

4.5 Nano Particles in Foam

Nanoparticles are molecules sized up to 100 nm and can be used with a surfactant to increase foam stability (Espinosa et al., 2010). Spherical silica nanoparticles have been used for EOR purposes and have shown promising results. Adsorption of nanoparticles on the rock surface is very low, and they maintain stability at high temperature and salinity over time without agglomeration (Alcorn, Føyen, Gauteplass, et al., 2020b). When surfactants are not sufficiently stabilizing foam, nanoparticles can be added to increase stability (Espinosa et al., 2010).

4.6 Foam Modelling

Foam behavior can be modeled in porous media by two main methods: population balance and local equilibrium. First, the population balance model accounts for the lamellae density and material balance at different points in the reservoir. The model describes foam generation and flows on a pore level. An extra differential equation is required in each step to calculate a balanced value for the lamella that includes generation, destruction, and convection (Kovscek & Radke, 1993; Rossen, 2013). On the contrary, the local-equilibrium model assumes that the generation and destruction of foam are always in equilibrium. The mobility reduction of the gas due to foam is based on the bubble size, foaming solution, and saturation, among other factors. The mobility reduction is represented in the model with a decrease in the relative permeability of gas without considering the mechanisms and effects of foam generation and destruction (Kular et al., 1989; Rossen, 2013). This thesis uses the local equilibrium model in performed simulations in the Schlumberger ECLIPSE reservoir simulator, where the method will be further discussed in Chapter 6.

5 In Situ Imaging

5.1 Computed Tomography (CT) imaging

Computed tomography (CT) imaging was first invented for medical use but was later used to visualize fluid flow inside porous media at the core scale, enabling core and flow characterization and measuring properties like porosity (Akin & Kovscek, 2003; Hove et al., 1987). CT comprises radiological x-ray images where the x-ray source or the object being imaged rotates. Three-dimensional images can be generated by interpolation among cross-sectional images. The resolution is on the millimeter scale, enabling visualization on the pore scale of porous media (Akin & Kovscek, 2003). During a CT scan, x-rays penetrate a small section of the scanned object, and sensors measure the intensity of the transmitted x-rays. The rotation of the source supplies many slices of x-ray images that can be composed into a 3D figure. Beer`s law (Equation 5.1) is used to quantify the measurements by the basic quantity measured for each volume element, or voxel, that makes up a linear attenuation(Akin & Kovscek, 2003). Beer`s law is defined:

$$(5.1) \qquad \frac{I}{I_0} = \exp^{\mu h}$$

Where *I* is the remaining intensity of the x-ray after it passes through the thickness h of a homogenous sample, I_0 is the incident x-ray intensity, and μ is the linear attenuation coefficient (Akin & Kovscek, 2003).

When the scanned material is not uniform, the composed images often appear blurred, and additional reconstruction is necessary. Convolutions can filter and improve the images, but the complex functions depend on many variables. When the images have been reconstructed, each pixel obtains a value for linear attenuation. Then, the values are normalized based on the linear attenuation of water and converted to CT numbers (Equation 5.2).

$$(5.2) \qquad CT_{number} = 1000 \cdot \frac{\mu - \mu_{water}}{\mu_{water}}$$

Where μ_{water} is the linear attenuation for water, and μ is the reconstructed linear attenuation. The unit for CT_{number} is Hounsfield units (H), where each unit represents a change of 0.1% in density based on the calibration density scale (Akin & Kovscek, 2003).

5.2 Positron Emission Tomography (PET) imaging

Positron Emission Tomography (PET) was developed for medical use but has also been used to visualize the flow in porous media (Brattekås et al., 2021; Brattekås et al., 2016). A PET scanner comprises several rings of detectors that detect photons from annihilation events. PET works by measuring the annihilation of photons created when a positron is emitted during radioactive decay. A radioactive tracer must be in place during the scan (Schmitz et al., 2013). Different radioactive tracers can be used if they do not alter the biological activity. For example, fluorodeoxyglucose (FDG) is water-soluble and often used as a water tracer, while C-11 can be used to trace CO_2. The half-life of isotopes used for PET scans is often short because they are used for medical procedures, which means that the signal decay could be significant. Therefore, the half-life of the isotopes should be considered (Zahasky et al., 2019).

The data acquisition is based on the PET scanner's interactions with high-energy photons (511 keV). When annihilations occur, two photons are emitted in the exact opposite direction and will be registered by the PET sensors at two places. The observed coincidences determine the annihilation location by the line of response (LOR) that describes the path of the photons after the annihilation has occurred. The LOR can select the exact location of the annihilation from the difference in arrival time to the PET sensors (Schmitz et al., 2013).

6 Reservoir Simulation

6.1 Fundamental Principles

The ECLIPSE simulator contains two simulators named ECLIPSE 100 (E100) and ECLIPSE 300 (E300). E100 is a black oil simulator and can be used to simulate one to three phases. The simulator does not account for compositional changes and assumes that reservoir fluids do not change composition with time. On the contrary, E300 is a compositional simulator based on an equation of state where the components of the fluids in the model are defined and change in composition through time (ECLIPSE, 2016; Schlumberger, 2016).

6.2 Basic Equations

A set of equations is solved in each grid cell, representing a three-dimensional discrete unit at each timestep in the simulation. The governing equations are Darcy's law and Material balance. The first of the equation is Darcy's law (Equation 6.1), excluding the gravity term:

$$(6.1) \qquad q = -\frac{K}{\mu}\,\nabla P$$

Where q is volumetric flow, K is the absolute permeability, μ is the viscosity of the injection fluid, and P is the pressure gradient. Next, the material balance equation (Equation 6.2) describes the mass flux equal to the accumulation in the system and the injected and produced fluids.

$$(6.2) \qquad -\nabla \cdot M = \frac{\delta}{\delta t}\,(\phi\,\rho) + \mathrm{Q}$$

In the equation, M is the mass-flux, it is time, ϕ is the porosity, ρ the fluid density, and Q is the volumetric flow. The ECLIPSE simulator combines the equations 6.1 and 6.2 to a flow equation (Equation 6.3), including a gravity term:

$$(6.3) \qquad \nabla \cdot \left[\frac{K}{\mu\beta}(\nabla P - \gamma\nabla z)\right] = \frac{\delta}{\delta t}\left(\frac{\phi}{\beta}\right) + \frac{Q}{\rho}$$

Where β is the volume factor.

The calculated values determine the flow for each grid cell, but the surrounding cells affect the results. The model considers the flow between grid blocks into well completions, wells, and surface networks (Schlumberger, 2014).

6.3 Foam modeling in ECLIPSE

The local-equilibrium model described in Section 4.6 is used to model foam in ECLIPSE. The E300 compositional simulator was used in this thesis, but it is also possible to model foam with the E100 simulator. The local-equilibrium foam model uses an implicit texture approach that captures the effect of fluid saturations, surfactant concentration, and shear-thinning behavior foam (Sharma, 2019). An additional water component was added to model surfactant for the foam model. The E300 model accounts for decay and adsorption of the surfactant with chemical reactions. The main objective of the foam is to reduce gas mobility. ECLIPSE has two models for gas mobility reduction, where one is based on the tabular model that consists of specified mobility reductions for given concentrations of oil, water, and foam. The capillary number determines the system's net mobility reduction factor (Schlumberger, 2016).

The model used in this thesis uses an implicit-texture approach based on an empirical relation that includes fluid saturations and the shear-thinning effect of foam with increasing flow rates (Sharma et al., 2020). With increasing foam strength, the relative permeability of gas is decreased. The reduction in permeability is calculated by multiplying the gas's relative permeability (k_{rg}^{f}) with the mobility reduction factor (MRF) (Equation 6.4):

$$(6.4) \qquad k_{rg}^{f} = k_{rg}^{nf} \cdot MRF$$

The mobility reduction factor is defined (Equation 6.5)

$$(6.5) \qquad MRF = \frac{1}{1 + FMMMOB \cdot F_{water} \cdot F_{oil} \cdot F_{shear} \cdot F_{surfactant}}$$

Where FMMMOB is the maximum mobility reduction of gas which is possible to obtain for the given factors F_{water}, F_{oil}, F_{shear} and $F_{surfactant}$ they are defined below. The factors represent the effect of water (Equation 6.6) and oil saturation (Equation 6.7), shear rate (Equation 6.8), and surfactant concentration (Equation 6.9) which all range from 0 and 1. The capillary number (N_{ca}) accounts for the effect of capillary and viscous forces. The foam parameters: EPDRY, FMDRY, FMOIL, FMCAP, EPSURF, and FMSURF are used in the foam model. The parameters are based on previous studies derived from laboratory foam quality and rate scans (Sharma, 2019).

$$(6.6) \qquad F_{water} = 0.5 + \frac{\arctan\left[EPDRY(S_W - FMDRY)\right]}{\pi}$$

Where S_w is water saturation.

$$(6.7) \qquad F_{oil} = \left(\frac{FMOIL - S_o}{FMOIL}\right)^{EPOIL}$$

Where S_o is oil saturation.

$$(6.8) \qquad F_{shear} = \begin{cases} \left(\frac{FMCAP}{N_{ca}}\right)^{EPCAP} & if\ N_{ca} > FMCAP \\ 1 & if\ N_{ca} \leq\ FMCAP \end{cases}$$

$$(6.9) \qquad F_{surfactant} = \left(\frac{C_{surf}}{FMSURF}\right)^{EPSURF}$$

Where C_{surf} is the surfactant concentration.

Part II. Experimental and Numerical Procedures

7 Experimental Procedures

The experimental work in this thesis is divided into three parts:

1. Steady-state Foam Quality (FQ) and Rate Scans (RS)
2. Unsteady-state EOR and CO_2 storage experiments
3. In-situ Imaging of foam generation and propagation

7.1 Preparation and Core Material

All the experiments presented in this thesis have been conducted on Bentheimer Sandstone cores. Bentheimer sandstone is homogenous with constant pore size distribution and porosity, good lateral continuity, and high permeability. The exact values for the samples used in this thesis are listed in Table 7.1. The mineral composition consists of roughly 92% quartz, 5% feldspar, and 3% clay (Peksa et al., 2015). Bentheimer sandstone is favorable for conducting core flooding experiments due to its stable rock properties and minimal rock-fluid interactions. All cores had the same diameter with varying lengths. Core preparations and measurements were performed in collaboration with Ph.D. candidate Aleksandra Sæle.

Table 7.1 Rock properties for Bentheimer cores used in the experimental work.

Core ID	**SS1**	**SS2**	**SS3**	**SS4**
Experiment	FQ + RS	EOR, FQ*	In-situ baseline	In-situ foam
Length (cm)	16.05	15.55	6.43	6.73
Diameter (cm)	3.87	3.89	3.88	3.88
Pore Volume (mL)	41.99	41.14	16.73	16.87
Porosity (%)	22.24	22.29	22.00	21.21
Permeability (mD)	2262	2470	1210	1160

*Only for 3 of the experiments, specified when the results are presented

7.2 Cleaning and Preparation Procedure

After each experiment, a cleaning procedure was performed to ensure that the rock properties were restored. First, Isopropanol solution (IPA, Table 7.2) was injected for at least 3 pore volumes (PV) at 100 mL/h. Then, distilled water or brine was injected for a minimum of 10 PV, first at 100 mL/h and then at 10 mL/h. Finally, brine was injected for at least 2 PV. After the cleaning procedure, the permeability was measured to assure that the core was entirely clean, and the permeability was restored. If the permeability measurements were lower than before the experiment, IPA and brine were injected until the original properties were restored.

7.3 Fluid Properties

Different fluids were used for the experimental work, where Tables 7.2 shows fluid compositions, and Table 7.3 shows fluid properties. The fluid composition and properties are given at experimental conditions (40°C,180-185 bar, and 20°C, 90 bar). CO_2 with a purity of >99.99% was used in all experiments. Brine composed of distilled water with 3.5 wt.% dissolved sodium chloride was used as the aqueous phase in all experiments. In the experiments with a surfactant, the nonionic surfactant SURFONIC L24-22 was used at different concentrations, as shown in Table 7.2. This surfactant was selected because the absorption on the rock surface was low, as determined by Jian et al. 2016 (Jian et al., 2016). The SURFONIC L24-22 surfactant was also used in the recently completed field pilot (Alcorn, Føyen, Zhang, et al., 2020). Some experiments also had nanoparticles (Levacil) in the foaming solution, which are spherical silica nanoparticles. In the experiments with oil in porous media, the mineral oil n-Decane was used, and injection was performed through a separate pump.

After each experiment, the core was cleaned with an isopropanol solution and brine to remove all fluid residue from the core plug. The solution consisted of 87 wt.% isopropanol and distilled water. A more detailed cleaning procedure is given in Section 7.2.

Table 7.2 Fluid composition for injection fluids used in experiments

Fluid	**Composition**
Brine	Distilled water + 3.5 wt.% NaCl
CO_2	>99.99 % CO_2
n-Decane	$C_{10}H_{22}$
IPA	Distilled water + 87 wt.% Isopropanol (CH_3CHOCH_3)
SF-0.25	0.25 wt.% 24-22 Surfonic
SF-0.50	0.50 wt.% 24-22 Surfonic
NP-0.015	Levacil
NP-0.15	Levacil

Table 7.3 Fluid Properties at experimental conditions

Fluid	**Pressure (bar) and Temperature (°C)**	**Viscosity (cP)**	**Density (g/mL)**
Brine	180 bar, 40°C	1.016 $^{(1)}$	0.655 $^{(1)}$
Brine	90 bar, 20°C	1.09 $^{(1)}$	1.05 $^{(1)}$
CO_2	180 bar, 40°C	0.075 $^{(2)}$	0.82$^{(2)}$
CO_2	90 bar, 20°C	0.08 $^{(3)}$	0.84 $^{(3)}$
n-Decane	180 bar, 40°C	0.84 $^{(2)}$	0.73 $^{(2)}$

(El-Dessouky & Ettouney, 2002)$^{(1)}$ (Huber & Perkins, 2005)$^{(2)}$ (Lemmon, 2022)$^{(3)}$

7.4 Experimental Set-Ups

This section describes the experimental set-ups that were used in this thesis. All the experiments were performed with a similar set-up, but they are described individually to provide a detailed description of the different experiments. Set-up *I* was used for the Foam Quality, Rate Scan, and EOR experiments, while Set-up *II* was used for the in-situ imaging experiments.

Set-Up I: Foam Quality-, Rate Scan, CO_2 EOR and CO_2 Storage Experiments (Steady- and Unsteady State Experiments)

Figure 7.1 shows the set-up used to perform foam quality, rate scan, and CO_2 EOR and CO_2 storage experiments. A core plug of Bentheimer sandstone was wrapped in nickel foil, placed in a rubber sleeve, and mounted in the biaxial Hassler core holder. The nickel foil was used to prevent radial diffusion of CO_2, which could cause damage to the rubber sleeve surrounding the core. The core was placed vertically in the core holder. Fluids were injected through the inlet on the top and produced through the outlet on the bottom. The core holder was mounted inside a heating cabinet with a constant temperature of 40°C. An ISCO pump was used to control the core's confinement pressure by injecting hydraulic oil surrounding the rubber sleeve with the core inside. The confinement pressure was set to 240 bar for all the experiments to obtain an overburden pressure of 60 bar.

The pressure in the system was maintained by two back pressure regulators (BPR), which were connected to a nitrogen gas (N_2) tank. The first BPR was set to the desired system pressure of 180-185 bar, and the second was set to around 150 bar to reduce pressure fluctuations in the system. Four ESI pressure transducers with a pressure range of 0-400 bar and 0-250 bar were mounted in various parts of the system, as shown in Figure 7.1, to monitor the pressure. The differential pressure was continuously measured across the core and plotted in real-time on the computer using the software Raport 2.0.

The three pumps (Figure 7.1) were used to inject different fluids into the core and were controlled with the Quizix PumpWorks software. The Quizix QX6000 pump was only used in the EOR experiments to inject oil (n-Decane). The Quizix Q5000-10K and Q6000-10K were used in all the experiments to inject CO_2 and aqueous solution, respectively. The aqueous solution varied between brine and surfactant, depending on the experiment. Distilled water and isopropyl alcohol were injected with the same pump to clean the system and the core. The bypass tubing was used to divert flow away from the core. It was used before injecting a new fluid into the core and when the liquid in the Quizix Q6000-10K pump was changed for rinsing the tubing before the core inlet. The produced fluids at the system's outlet were depressurized by the BPRs and separated at atmospheric conditions. The EOR experiments were analyzed and separated in a measuring cylinder marked B in Figure 7.1. The foam quality and rate scan experiments followed the tubing marked A, where the weight of the produced fluids was measured, and CO_2 was vented through the adsorption column. A complete list of equipment used in the experiments is listed in Table 7.4.

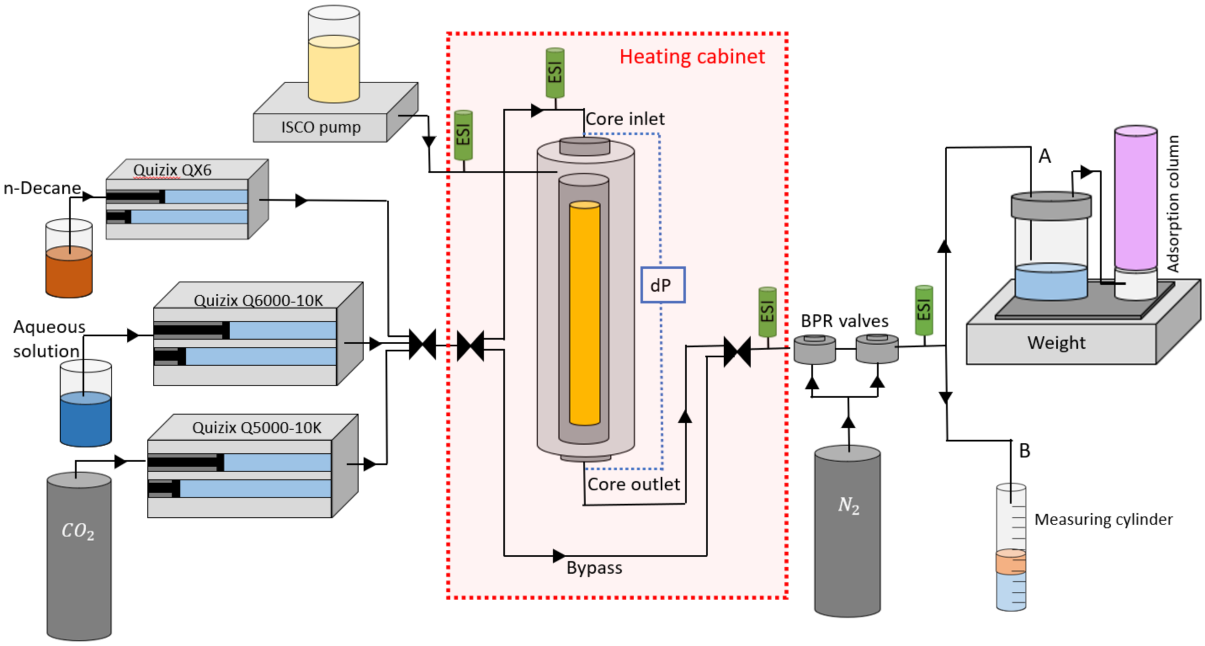
ISCO pump
Heating cabinet
ESI
Core inlet
n-Decane
Quizix QX6
dP
Aqueous solution
Quizix Q6000-10K
Quizix Q5000-10K
CO_2
Core outlet
Bypass
BPR valves
N_2
A
Adsorption column
Weight
B
Measuring cylinder

Figure 7.1 Illustration of the experimental set-up where n-Decane, aqueous solution, and CO_2 are injected, and the arrows indicate the flow direction. Produced fluids from the core go into set-up marked A for the steady-state Foam Quality and Rate Scan experiments and B for unsteady-state EOR and CO_2 storage experiments. All experiments were conducted at 180 bar and 40°C.

Table 7.4 Equipment included in set-up I

Equipment for set-up I	**Function**
Quizix QX600 pump	Oil injection
Quizix Q6000-10K pump	Water injection
Quizix Q5000-10K pump	CO_2 injection
ISCO syringe pump	Confinement pressure
CO_2 tank	
Swagelok tubing, fittings, and valves	
Autoclave fittings and valves	
Automatic valves	
Heating cabinet	
Hassler Core Holder	
ESI Pressure Transducers	for pressure measurements (0-250, 0-400 bar)
Differential Pressure transmitter	Range 0-16 bar
Equilibar Back Pressure Regulator	
Nitrogen tank	To pressurize the BPRs
Weight	Measure produced fluids
Adsorption Column	
Production Beaker	For Foam Quality and Rate Scan experiments
Production Cylinder	For EOR experiments
Computer	to operate the pumps, read the pressure transducers, differential pressure, and weight, and operate automatic valves

Set-Up II: In-Situ Imaging Experiments

A schematic of the experimental set-up used to perform in-situ imaging experiments is presented in Figure 7.2, and a list of equipment in Table 7.5. A Bentheimer core plug was wrapped in aluminum foil, and the endpieces were connected to the ends by aluminum tape. The core and endpieces were placed in a rubber sleeve and mounted in a horizontal core holder. The core holder was custom-made to fit in the PET/CT scanner. After the core holder was placed on the mechanical arm and driven into the PET/CT scanner, a CT scan was conducted to confirm that the core was in the correct position. A radioactive tracer, Fluorodeoxyglucose F-18 (FDG), was added to the aqueous solution prior to injection to be able to trace the flow pattern of brine or foaming solution inside the core. A computer controlled two pumps to control fluid injection, a Quizix Q5000-10K pump for brine and foaming solution, and a Sanchez 1000/300 pump for CO_2 injection. PET scans were performed for all parts of the experiments described in Section 7.7. The confinement pressure was obtained by an ISCO pump and set to 130 bar to provide 40 bar of overburden. The system pressure was 90 bar and was controlled by a back pressure regulator (BPR) valve. Finally, fluids were produced and depressurized through the BPR.

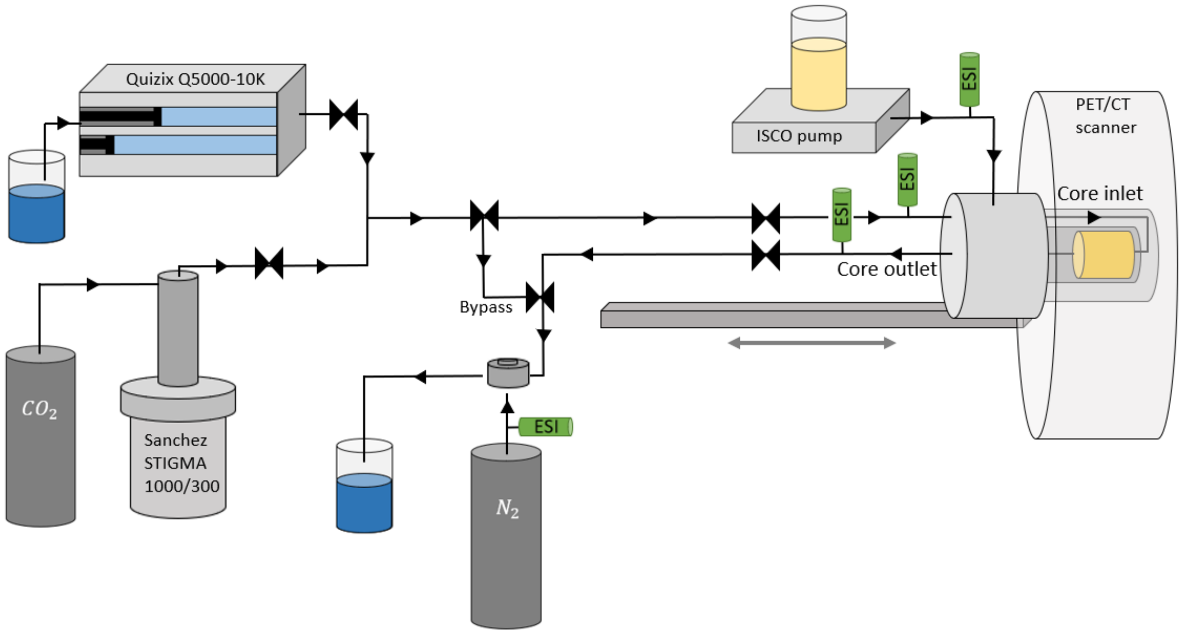

Figure 7.2 Schematic of the experimental set-up where aqueous solution and CO_2 are injected, and the arrows indicate the flow direction. The core holder is placed inside a PET/CT scanner, which was continuously scanned. Fluids are produced from the system through a depressurizing BPR valve because experiments were performed at 90 bar and 20°C.

Table 7.5 Equipment included for set-up II

Equipment for set-up II	**Function**
PET/CT scanner	Visualize the front development and fluid displacement processes
Sanchez STIGMA 1000/300	CO_2 injection
Quizix Q5000-10K	brine and foaming solution
ISCO syringe pump	confinement pressure
CO_2 tank	gas injection
ESI Pressure Transducers	pressure measurements (0-250 bar)
Nitrogen tank	pressurizing the BPRs
Computer	operate the pumps, read the pressure transducers, differential pressure, and weight, and operate automatic valves
Automatic valves	
Swagelok tubing, fittings, and valves	
Autoclave fittings and valves	
PEEK tubing	
Differential Pressure transmitter	Range 0-16 bar
Equilibar Back Pressure Regulator	
Custom core holder	
Production cylinders	

7.5 Steady-State Foam Quality and Rate Scans

Steady-state co-injection experiments investigated foam strength at different gas fractions and flow rates. Two kinds of experiments were performed, foam quality and foam rate scans. The conditions for all the experiments were 180 bar and 40 °C. In both experiments, supercritical CO_2 and aqueous solution were injected into a brine saturated core simultaneously until steady-state conditions were reached for the given gas fraction. The aqueous solutions used were brine or foaming solutions, with concentrations given in Table 7.2. At least 3 PV were injected for each gas fraction and flow rate to achieve a steady-state for apparent viscosity calculations. When steady-state was obtained, the last PV injected before changing gas fraction was used to calculate the apparent viscosity, and the standard deviation was used to quantify uncertainty. The differential pressure, injected fluid, and weight of produced fluids was continuously monitored during the experiments.

During the foam quality scans, the injected gas fraction increased from low to high, by increments of 0.10 or 0.05, starting at a gas fraction of 0.30 until a gas fraction of 1.0, where 100% supercritical CO_2 was injected. The objective of the experiments was to find the gas fraction with the highest measured apparent viscosity to investigate the increase in foam strength until coarsening of the foam with increasing gas fraction. Different foaming solutions were used with a nonionic surfactant or a combination of nanoparticles and nonionic surfactant. Different solutions were used to investigate the effect of concentration on the foam strength and coarsening behavior. All the injected solutions are listed in Figure 7.2. All the solutions consisted of brine with added 0.25 wt.% Surfonic L24-22 surfactant, except in the baseline experiments where only brine was injected. Two foam quality and rate scans were also conducted with nanoparticles (NP) and surfactant (SF), with different concentrations of nanoparticles, 0.15 and 0.015 wt.%, respectively. The nanoparticles used were Levacil, described in chapter 4.5.

The foam rate scans were performed to investigate the foam's shear-thinning behavior and determine the foam strength dependency at different flow rates. Each foam rate scan was performed using the same injection fluids and core after a corresponding foam quality scan. The optimal foam quality, identified from the foam quality scans, was used and was injected from low to high flow rates starting at 1 or 2 ft/day and then increasing to 4, 8, and 12 ft/day. The experiments were conducted with the same fluid compositions as the foam quality scans to analyze the foam flow behavior at increasing injection rates.

7.6 Unsteady State EOR and CO_2 Storage Experiments

Unsteady-state EOR experiments were performed to investigate oil recovery performance and CO_2 retention with various injection strategies at a pressure of 180 bar at 40 °C. The core was initially saturated with 100% brine and was flooded with n-decane at 13 ft/day to drain the brine from the core. The drainage was conducted until the water production subsided and the oil saturation ranged from 0.50 to 0.70 at irreducible water saturation (S_{wi}). Afterward, different injection strategies were imposed to displace oil from the core. The Bentheimer sandstone core used during the EOR experiments was SS2, described in Table 7.1.

During the single-cycle WAG/SAG (Figure 7.3), 1 PV of the aqueous solution was injected into the core at a superficial velocity of 4 ft/day. Brine was used as the injection fluid for the WAG and foaming solution with a concentration of 0.25 wt.% Surfonic L 24-22 for the SAG injection. Next, supercritical CO_2 was injected at 4 ft/day for approximately 9 PV. The goal was to reach irreducible water and residual oil saturation and obtain the maximum gas saturation.

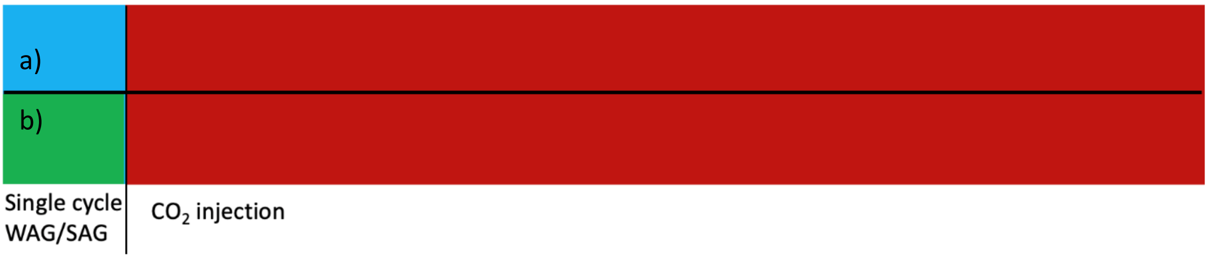

Figure 7.3 Single-cycle WAG and SAG injection where a) represents the WAG injection with brine and b) represents the SAG injection. The total injected volume is equivalent to 10 pore volumes.

The rapid WAG/SAG (Figure 7.4) process was first imposed after injecting 1 PV of brine at a superficial velocity of 4 ft/day to mimic conditions after waterflooding. Next, approximately 3.5 PV of rapid WAG or SAG were imposed. The Rapid WAG/SAG consisted of several cycles, where a cycle consisted of the injection of the aqueous solution followed by CO_2. The aqueous solution was brine during the WAG injection, and foaming solutions with a concentration of 0.25 wt.% or 0.50 wt.% Surfonic L 24-22 was injected during the rapid SAG experiments. The total volume of each cycle was equal to 0.2 pore volumes and targeted a foam quality of 60% CO_2 by injection of aqueous solution and CO_2 at a fraction of 0.40 and 0.60, respectively.

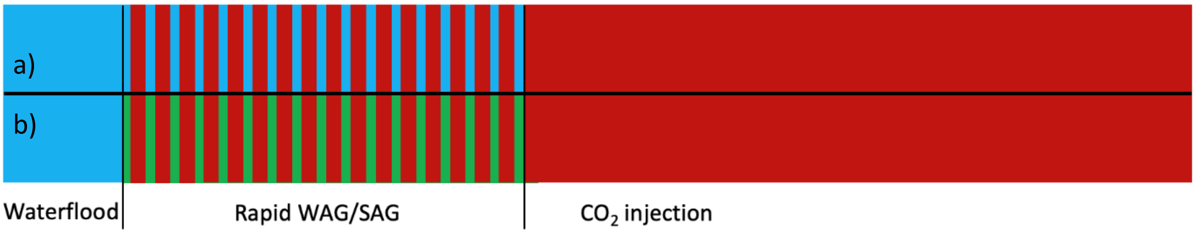

Figure 7.4 Rapid WAG and SAG injection pattern where a) represents the rapid WAG injection and b) represents the rapid SAG injections.

The differential pressure and produced fluids were measured during the single-cycle and Rapid WAG/SAG experiments. The measured differential pressures were used to calculate apparent viscosity (Equation 4.2) for the duration of the experiments, and the produced fluids were used to calculate the recovery factor for oil and CO_2 retention to determine CO_2 storage potential.

7.7 In-Situ Imaging Experiments

The in-situ imaging experiments were conducted to visualize and further investigate foam flow in porous media. Several subsequent floods, each with added tracer, were performed.

The core was initially saturated with brine, and a CT scan was conducted before any injection to ensure the exact placement of the core plug. Then, the in-situ imaging experiments were conducted in two parts, as listed below:

1. Baseline brine and CO_2 injection
2. Single-cycle SAG with the injection of foaming solution and CO_2

During brine, surfactant, and CO_2 injections, PET scans were conducted to visualize the front development and fluid displacement processes in the core sample. Only the phase with the radioactive tracer is visible on the PET scan. The radioactive tracer 18-F-FDG, commonly used for in-situ imaging of porous media, was used to trace the aqueous solution in all performed experiments (Zahasky et al., 2019). The PET signal explicitly gives the position of the traced fluid in three dimensions as a function of time. The absence of signal represented the fluid without tracer, which was either initial brine saturation or CO_2. The differential pressure across the core was also measured to calculate apparent viscosity and quantify foam generation. The production of the water and foaming solution was measured during CO_2 injection to calculate the saturations in the core from material balance.

Baseline Single-Cycle WAG

Before the baseline experiment (Figure 7.5), the radioactive tracer was added to the injection brine. The radioactively traced brine was injected at 4 ft/day for approximately 2 PV. A PET scan was conducted for the entire injection duration to capture the displacement process and flow patterns within the core plug. The PET scanner detects the photons emitted due to the radioactive decay, and only the injected brine will be visible for the PET reconstructions. Therefore, the absence of signal represents the brine initially in place.

The core was saturated with radioactive brine at the second injection stage when CO_2 injection was initiated. The injection rate of the CO_2 was 4 ft/day, and CO_2 was injected for approximately 1PV. The absence of a PET signal determines the flow patterns of the CO2 because the water phase in the core is radioactively traced.

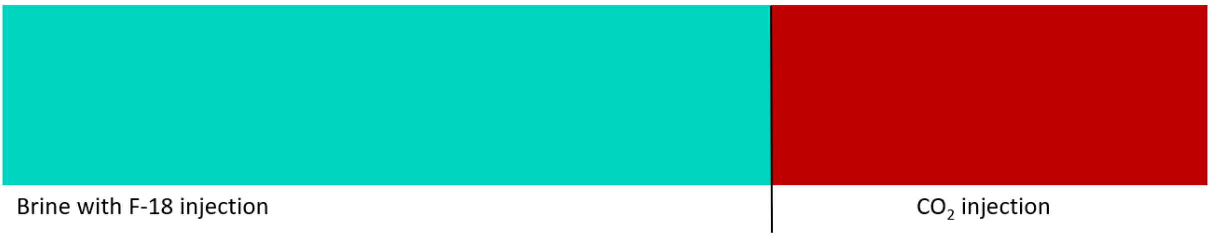

Figure 7.5 Schematic of the baseline injection of 2PV of brine, followed by 1 PV of CO_2.

Surfactant and CO_2 Injection

The radioactive tracer was added to a foaming solution with 0.50 wt.% Surfonic L24-22. All injections were performed with the traced foaming solution (Figure 7.6). First, the foaming solution was injected at 4 ft/day into a brine-saturated core for approximately 2 PV to saturate the core with the foaming solution. The brine displacement by the foaming solution was miscible, and the core was assumed to be completely saturated with traced foaming solution after the flooding. Next, 2 PV of CO_2 were injected at 4 ft/day. The fluid production was measured to calculate the saturation in the core from material balance.

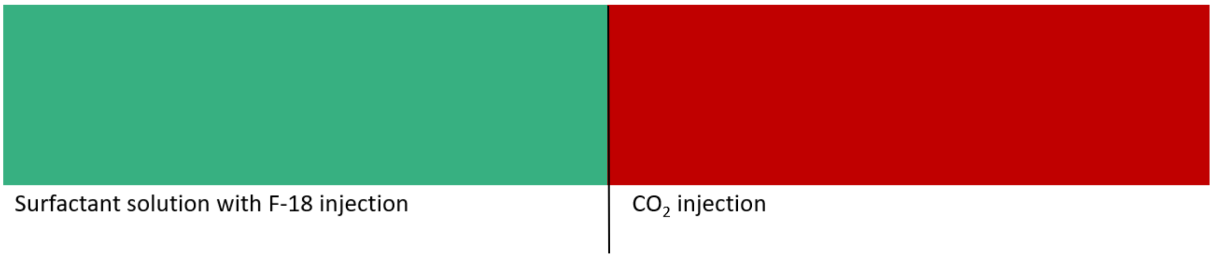

Figure 7.6 Schematic of the injection pattern with 2 PV injected of foaming solution and 2 PV of CO_2.

Volumes of Interest (VOI) and Regions of Interest (ROI)

To analyze the distribution of PET signal from the core plug, VOI and ROIs were defined (Figure 7.7). A VOI consists of a selected volume, while an ROI consists of a two-dimensional area, where a single value represents all the signals in the defined area. Both VOI and ROI values are time-dependent and change with time, based on the signal variations in the defined area. In the performed Single Cycle WAG and SAG, a VOI was defined as the volume of the entire core (white box). Also, seven ROIs covering the core axial cross-section were placed through the length of the core.

The first one (ROI1, white line) was placed 0.5 cm from the inlet, and the last (ROI7, orange line) was placed 0.5 cm from the outlet. The remaining five were equally spaced with 0.9 cm between them from ROI1 to ROI7, increasing numbers from the inlet to the core outlet and providing dynamic insight into saturation development along the core length. To eliminate signal noise, seven ROIs were placed in proximity of the core (ROI11, red circle).

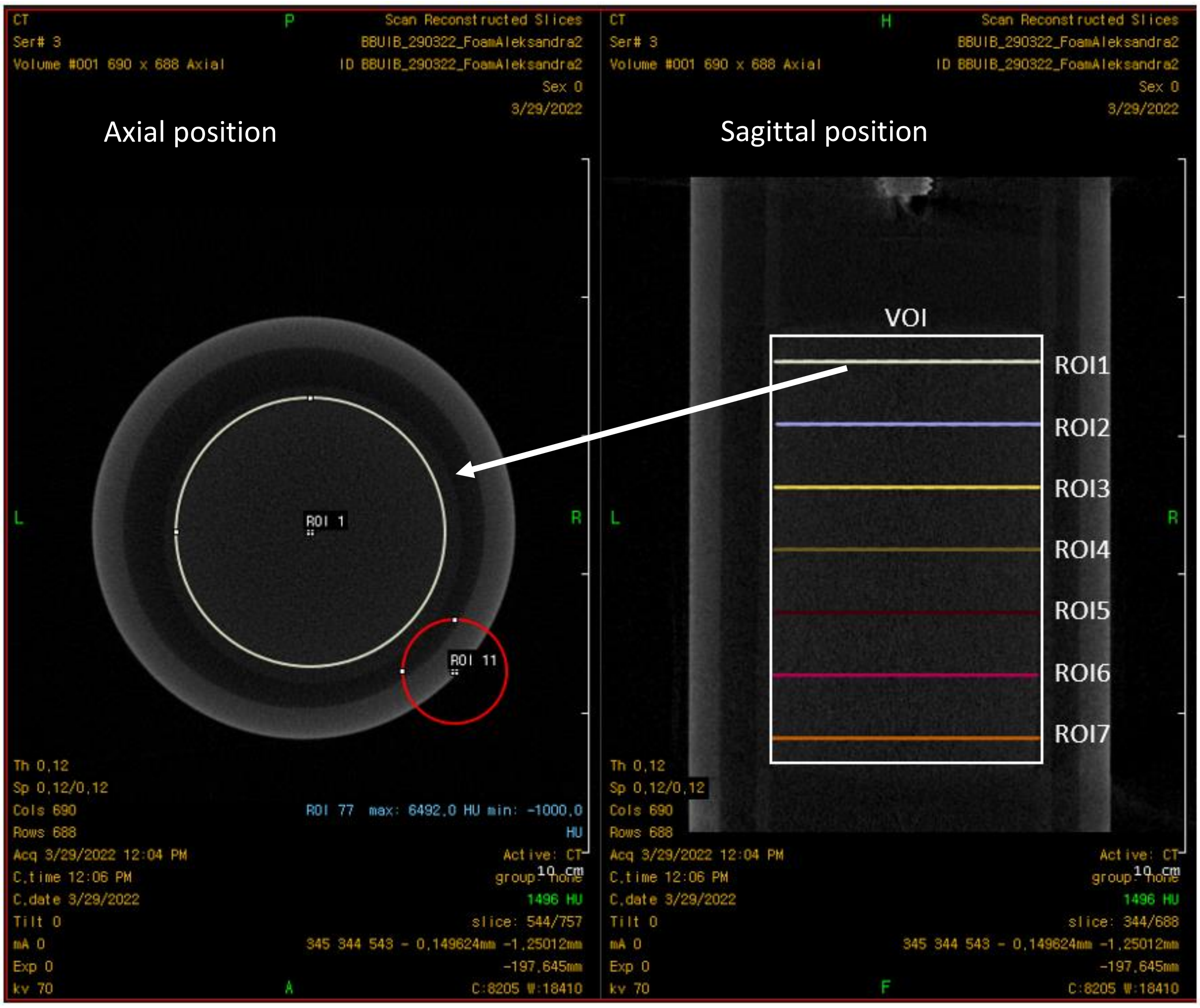
Axial position
Sagittal position
VOI
ROI1
ROI2
ROI3
ROI4
ROI5
ROI6
ROI7
ROI 1
ROI 11
CT
Ser# 3
Volume #001 690 x 688 Axial
Scan Reconstructed Slices
BBUIB_290322_FoamAleksandra2
ID BBUIB_290322_FoamAleksandra2
Sex 0
3/29/2022
P
H
L
R
A
F
Th 0,12
Sp 0,12/0,12
Cols 690
Rows 688
Acq 3/29/2022 12:04 PM
C.time 12:06 PM
C.date 3/29/2022
Tilt 0
mA 0
Exp 0
kv 70
ROI 77 max: 6492.0 HU min: -1000.0 HU
Active: CT
group: none
10 cm
1496 HU
slice: 544/757
slice: 344/688
345 344 543 - 0,149624mm -1,25012mm
-197,645mm
C:8205 W:18410

Figure 7.7 CT scan with a schematic of the VOI covering the entire volume of the core and 7 ROIs covering cross-sections from the core inlet to the outlet. On the left is the core in axial position where ROI1 covers the cross-section of the core, with ROI11 in proximity of the core, and the right image shows the VOI and ROI from sagittal position. The grey circular area surrounding the core plug (inside VOI) is the core holder, which is visible on the CT scan.

7.8 Experimental Overview

An experimental overview is given in Table 7.3, including all experiments performed for this thesis.

Table 7.3 Experimental Overview

Experiment	Type of experiment	Core material (Table 7.1)	Saturation fluids	Injection fluids	Number of experiments
Steady-state Co-injection	Foam Quality Scan	SS1 SS2	-	(Baseline) Brine + CO_2	1
				SF* + CO_2	4
				SF*+ NP*+ CO_2	2
	Rate Scan	SS1 SS2	-	(Baseline) Brine + CO_2	1
				SF* + CO_2	3
				SF*+ NP*+ CO_2	2
Unsteady-state WAG/SAG	Single Cycle	SS2	Brine	(baseline) CO_2	3
			SF*	CO_2	3
	Rapid	SS2	Brine	(Baseline) Brine + CO_2	4
				SF* + CO_2	8
In-situ imaging	Single Cycle	SS3 SS4	Brine	(Baseline) Brine	1
				(Baseline) CO_2	1
				SF*	1
			SF*	CO_2	1

7.9 *SF = Surfonic L24-22 at concentration 0.25wt.% or 0.50 wt.% and NP = Levacil at concentration 0.015 wt.% or 0.15 wt.%, detailed description in Table 7.2

8 Numerical Modelling Methods

This chapter describes the methods used for numerical simulations in this thesis. Simulations were conducted on a cross-sectional reservoir model to investigate field-scale foam generation and propagation. The reservoir model was built by Dr. Zachary Paul Alcorn and Dr. Mohan Sharma for a field pilot in the East Seminole field in west Texas (Alcorn et al., 2019; Alcorn, Føyen, Zhang, et al., 2020). The simulations were run with the ECLIPSE E300 simulator, and the objective was to investigate different injection strategies to determine which one provided the most oil recovery and CO_2 storage potential. The injection strategy, which was used for the field pilot, was a rapid SAG and was included as one of the injection strategies. Bottom hole pressure and tracer production were analyzed to investigate whether foam was generated and CO_2 mobility reduction. The cumulative oil, water production, and CO_2 retention were used to determine oil recovery and CO_2 retention for the different injection strategies. The injection strategies were based on the EOR experiments described in chapter 7.

8.1 Model Description

The numerical model consists of a high-resolution two-dimensional cross-section of the East Seminole Field in the Permian Basin in west Texas. The cross-section in the model is located between two wells, the injection well (I1) and the producing well (P1), with grid dimensions of 75x1x54 composed of 4050 grid cells corresponding to a cross-section with a depth of 170 ft and a length of 750 ft. The grid cells extend a depth of 10 ft in the x-direction and an average of 2.5 ft in the z-direction. The length corresponds to the length between the wells I1 and P1 (Alcorn, Føyen, Zhang, et al., 2020).

The East Seminole field produces from the San Andres reservoir and was first developed in the 1940 (Alcorn et al., 2016). Since the field began production, both water and CO_2 injection have been implemented as EOR measures with limited success due to the significant heterogeneity of the reservoir and poor sweep due to the high mobility of CO_2 (Alcorn et al., 2016). The reservoir comprises dolostone facies with a porosity ranging from 0.03 to 0.28 with an average of 0.12. The reservoir is layered with poor vertical communication due to shaley mudstone interbedding. The permeability ranges from 1 to 300 mD with an average value of 7 mD (Sharma, 2019). The permeability distribution in the cross-sectional model is shown in Figure 8.1 below.

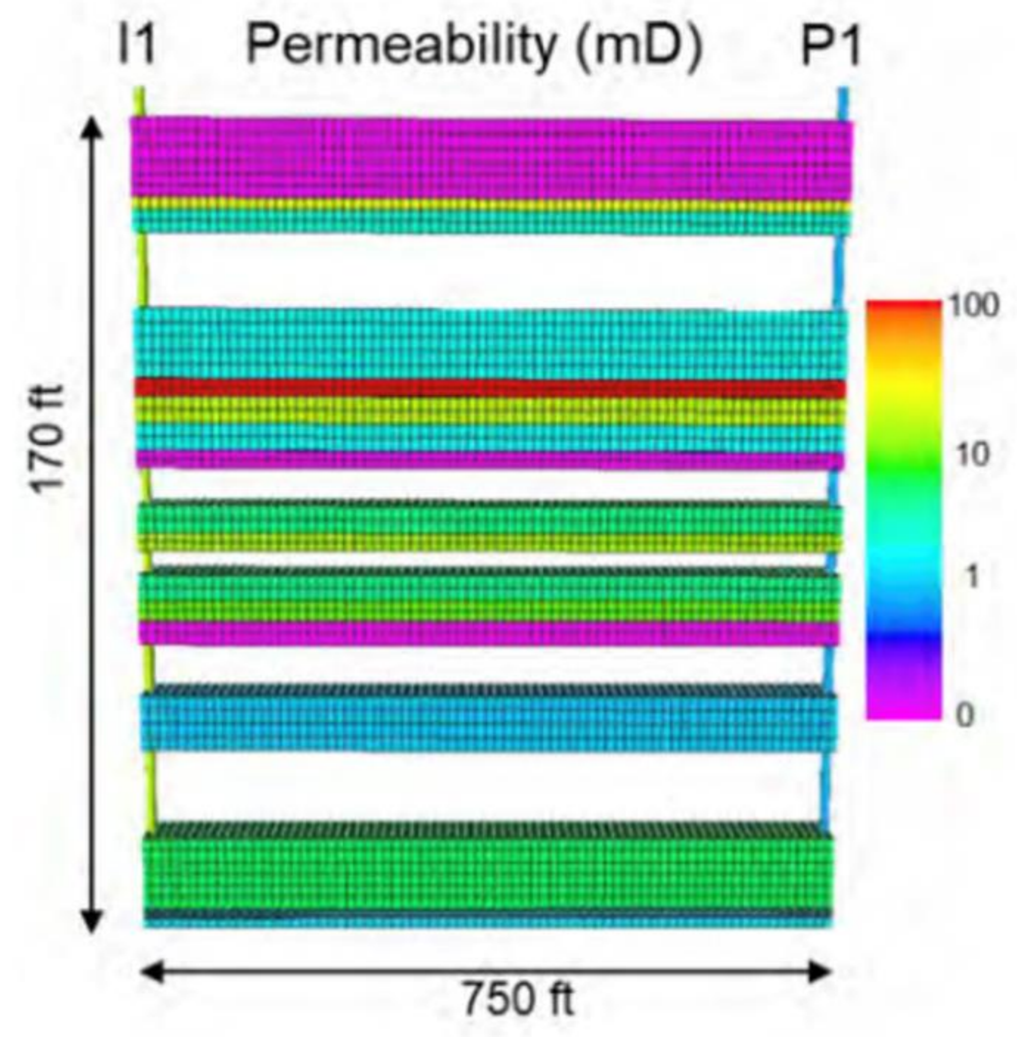

Figure 8.1 Schematic of the cross-sectional reservoir model with the distribution in permeability (Alcorn, Føyen, Zhang, et al., 2020).

8.2 Fluids in the Model

The Peng-Robinson equation of state models the fluids in the system with six components tuned to PVT data collected from available oil samples from the main producing or pay zone (MPZ). The oil comprises two heavy components, C7+, and four light components, CO_2, N_2+C1, H_2S+C2+C3, and C4+C5+C6 (Sharma, 2019). The model used two water phases: water and foaming solution. The distribution of fluids is listed in Table 8.1. The heavy component fraction was split with Gamma distribution and Gaussian quadrature-based lumping before the critical properties were calculated with the Lee-Kesler correlation (Sharma, 2019). The PVT data were matched by tuning the C7+ components with a swelling factor with a given saturation pressure for interaction with CO_2.

Table 8.1 Fluid composition measured in the main pay zone (MPZ) and the residual oil zone (ROZ) modified from(Sharma, 2019).

Component	**Fluid Composition (mol%)**	
	MPZ	**ROZ**
N_2	0.51	0.04
CO_2	2.47	0.02
H_2S	1.96	0
C1	24.65	20.1
C2	9.1	9.07
C3	7.57	6.95
iC4	1.41	0.04
iC5	1.76	0.04
nC5	2.03	2.49
C6	3.54	2.69
C7+	40.97	54.66

Laboratory measurements concluded that the wettability in the reservoir is mixed-wet with a tendency towards oil-wet. The relative permeability curve, presented in Figure 8.3, was derived by tuning available core flood data to a Corey-type model. The oil displacement of CO_2 was assumed to be miscible, and the relative permeability curves for CO_2 and oil are therefore straight and not presented in this thesis. The derived fluid model was fit to the available experimental data from differential liberation, swelling, and constant compositional expansion. The results from the experiments compared to field data are presented in Figure 8.2.

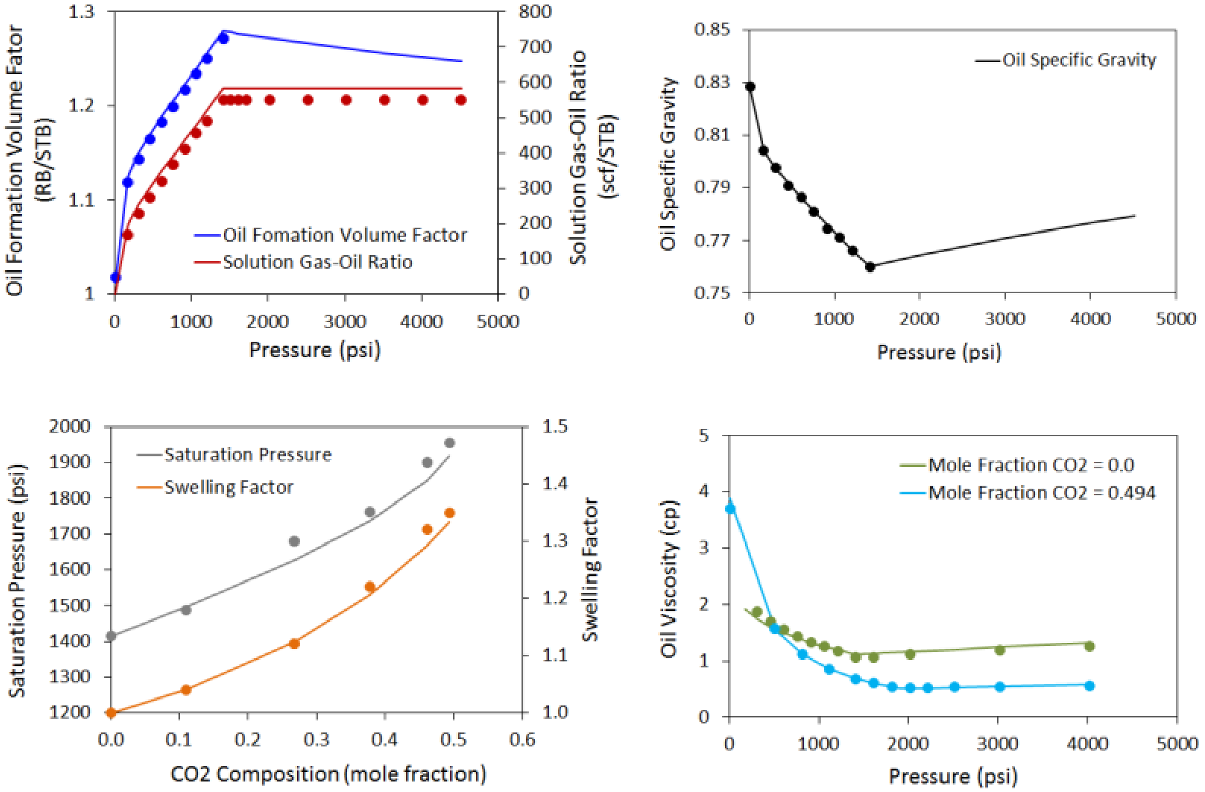

Figure 8.2 The fluid model compared to conducted experiments. The dots represent experimental data, and the lines correspond to the tuned equations of state in the model (Sharma et al., 2017).

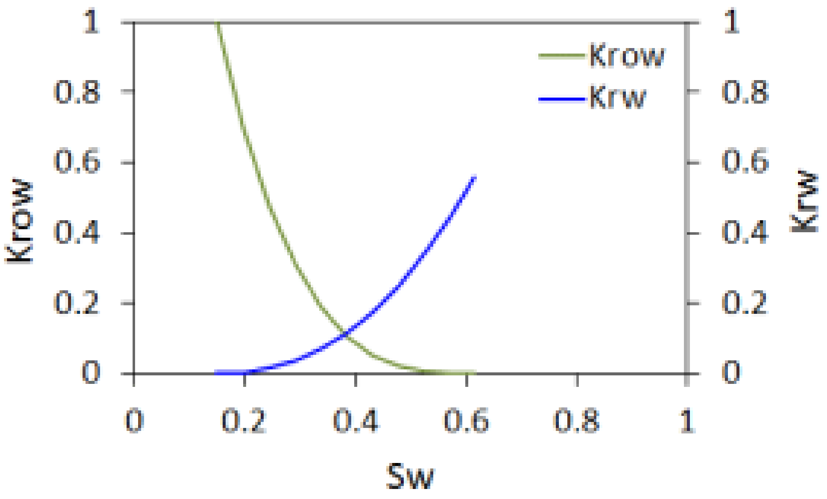

Figure 8.3 Relative permeability curve for water and oil used in the simulation models (Sharma et al., 2017).

8.3 Foam Modeling

The foam in the model was simulated with a local-equilibrium model described in chapter 6.3. The parameters were derived from fitting experimentally conducted foam quality and rate scan experiments by regression, shown in Figure 8.4 (Sharma, 2019; Sharma et al., 2017).

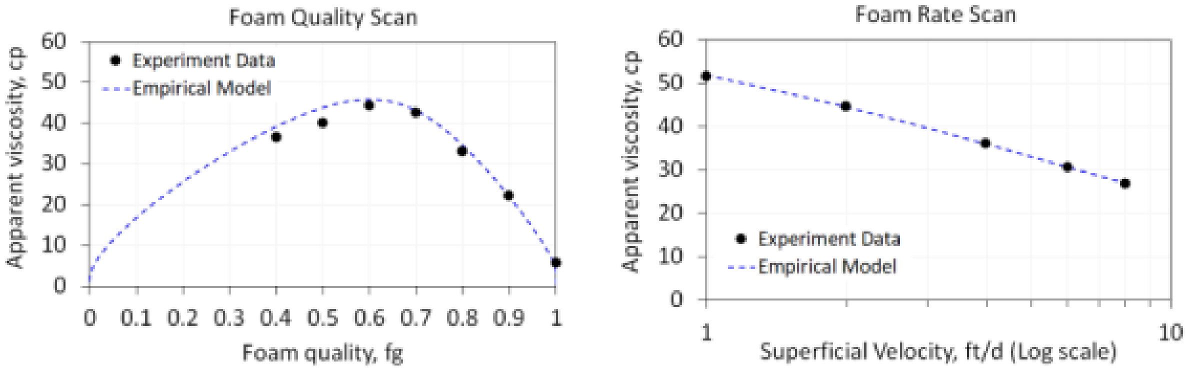

Figure 8.4 Results of conducted foam quality and rate scan experiments fit the empirical model in ECLIPSE (Alcorn, Fredriksen, et al., 2020; Rognmo et al., 2019; Sharma, 2019).

The model's foam parameters are based on the variables FMMOB, FMDRY, and EPDRY. The reservoir section was divided into three regions based on permeability, where region 1, 2, and 3 has an average permeability of <10mD, 10-50mD, and >50mD, respectively. The three regions are shown in Figure 8.5. The three permeability regions were assigned different foam parameters to capture the effect of permeability on foam generation and strength. For example, in region 1, with the lowest permeability, no foam is assumed to generate. Both regions 2 and 3 can have foam generation, but the FMMOB of the foam in region 3 is assumed to be two times larger than in region 2 (Sharma et al., 2017).

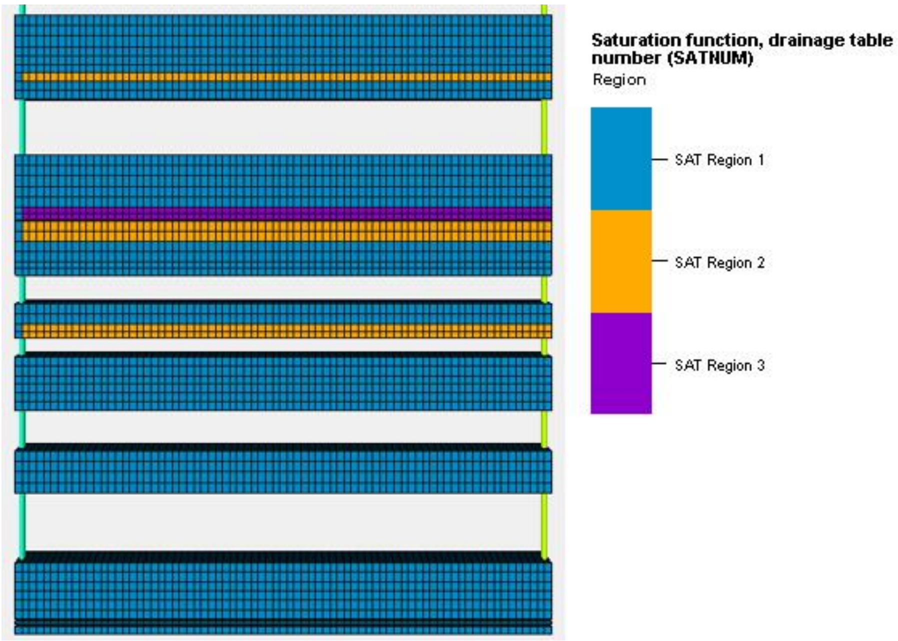

Figure 8.5 Saturation function for foam consisting of three regions with different foam parameters and properties.

The surfactant concentration used in the model is 0.50 wt.% of the Surfonic L24-22, used in all experimental work performed for this thesis. The CMC of the surfactant has previously been determined to be 0.01 wt.% and set to be the minimum concentration for foam generation in the model. The transition to strong foam was assumed to be five times CMC, forming the base value for FMSURF at 0.05 wt.%. All the values used in the different regions of the foam model are presented in Table 8.2 below (Alcorn, Fredriksen, et al., 2020).

Table 8.2 Derived foam parameters used in the foam model.

Parameter	Region	Base value	Remarks
FMMOB	1	0	Assumed no foam generation
	2	630	Based on Foam Quality Scan
	3	1200	
FMDRY	1	0.32	
	2	0.27	Based on Foam Quality Scan
	3	0.22	
EPDRY	1	500	
	2	100	Based on Foam Quality Scan
	3	25	
FMCAP	All	$7.8 \cdot e^{-7}$	Based on Foam Rate Scan exp.
EPCAP	All	0.65	Based on Foam Rate Scan exp.
FMSURF	All	0.175	Assumed to be 5 times CMC
EPSURF	All	1	
FMOIL	All	0.28	Based on EOR experiments
EPOIL	All	1	

8.4 Injection Strategies

Three different injection strategies were implemented in the model to compare the reservoir parameters and, most importantly, to compare oil recovery and CO_2 storage potential. Implementation of the different strategies was with and without surfactant present to compare the effects of the surfactant for determining foam generation and strength. The injection schemes were based on the pilot program's rapid SAG and the EOR and CO_2 storage experiments described in Section 7.6. In addition, two other injection schemes were performed to compare with the rapid WAG/SAG: a single cycle WAG/SAG and a co-injection. All changes made to the model were during the pilot's injection from May 2019-August 2020, and the pre-and post-pilot data was kept the same. The implementation of different injection schemes was called pilot in all three cases. The three injection strategies consisted of a baseline with only water and CO_2 injection and one with 0.50 wt.% surfactant in the water solution. For comparison, all three injection strategies injected approximately the same CO2 and aqueous solution volumes.

Rapid WAG/SAG

The rapid WAG and SAG consisted of 12 cycles of alternating water or foaming solution injection for 10 days, followed by 20 days of CO_2 injection (Figure 8.6). The foaming solution in the rapid SAG process had a concentration of 0.50 wt.% surfactant. The rapid SAG injection targeted a foam quality of 0.70 at an injection rate of 500 RB/day.

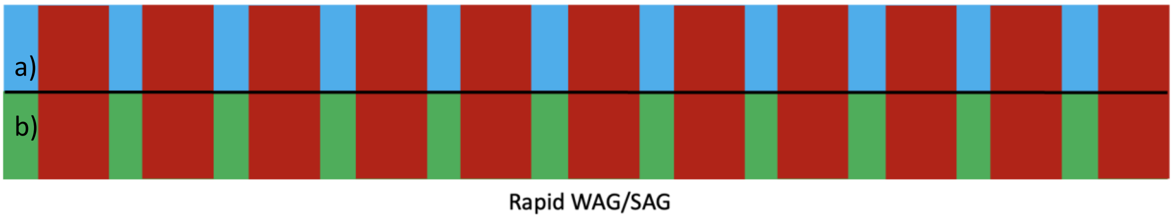

Figure 8.6 Schematic of the rapid WAG marked a) and the rapid SAG marked b) injection strategies consisting of 11 slugs of the aqueous phase and CO_2.

Single Cycle WAG/SAG

The single-cycle WAG and SAG consist of one continuous slug of water or foaming solution, injected for 110 days, followed by 220 days of CO_2 injection (Figure 8.7).

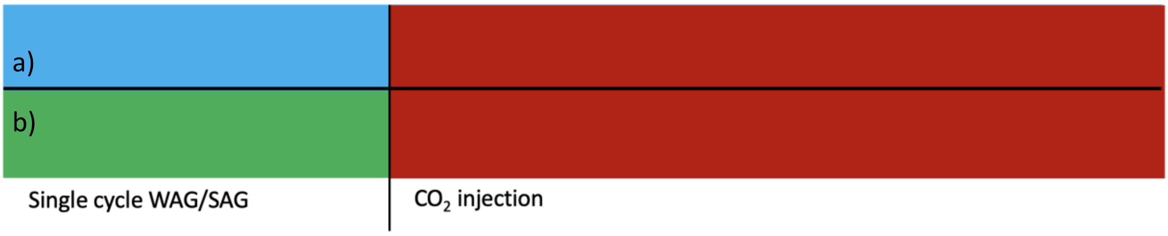

Figure 8.7 Schematic of the Single-cycle WAG marked a) and the single-cycle SAG marked b).

Co-Injection of aqueous solution and CO_2

In addition to the WAG/SAG strategies, a co-injection strategy was implemented to compare the foam behavior with alternating slug injection to simultaneous injection of both phases. The strategy targeted a gas fraction of 0.60. The co-injection lasted for 183 days, followed by 147 days of pure CO_2 injection to match the injected volumes in the WAG/SAG cases (Figure 8.8).

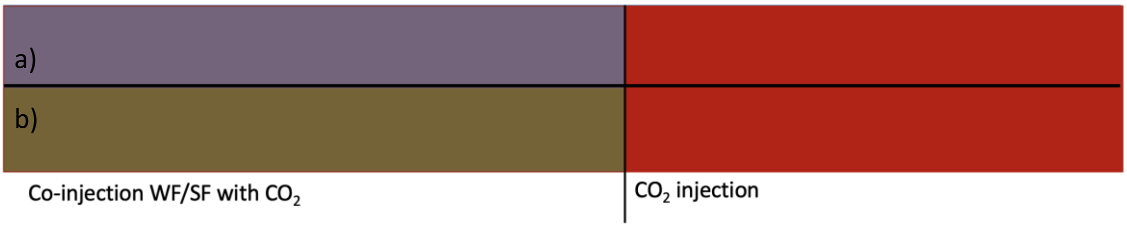

Figure 8.8 Schematic of the co-injection of water and CO_2 marked a) and foaming solution and CO_2 marked b).

Part III. Results and Discussion

9 Steady-State Co-Injections – Foam Quality and Rate Scans

This chapter presents the foam quality and rate scan experiments described in Section 7.5. First, baseline experiments were performed with brine to compare with experiments with foaming agents. Furthermore, different foaming solutions were used, as described in Section 7.3 in Table 7.2. The objective of the foam quality scans was to determine at which gas fraction the strongest foam was generated. Next, the selected gas fraction was used in a rate scan experiment to investigate the effect of injection rate on foam strength. Finally, the optimal gas fraction and injection rate was used in the EOR and CO_2 storage experiments in chapter 10. In addition, foam model parameters for numerical simulations can be extracted from the foam quality and rate scans.

9.1 Baseline - Without Foaming Agent

To establish a baseline, co-injection of brine and CO_2 was performed following the procedure for foam quality and rate scans described in Section 7.5. The baseline experiments, without foaming agents, were conducted for comparison to foam quality and rate scans with a foaming agent. The baseline foam quality scan was performed at an injection rate of 2 ft/day at a pressure of 180 bar and a temperature of 40°C and was performed with increasing gas fractions from 0.30 to 1.0 in a drainage-like process. The foam rate scans used the optimal gas fraction from the foam quality scans and started at a 2ft/day injection rate.

Figure 9.1a shows apparent viscosity as a function of gas fraction for the baseline quality scan. The apparent viscosity was 2.5 cP for the first two injected gas fractions of 0.30 and 0.50. At higher gas fractions, the apparent viscosity decreased gradually to 1.0 cP. The measured apparent viscosities confirmed that no foam was generated during the baseline foam quality and rate scan. However, the measured apparent viscosity is higher than expected for CO_2 and brine in a single-phase system due to reduced relative permeability for both fluids due to the presence of the other phase.

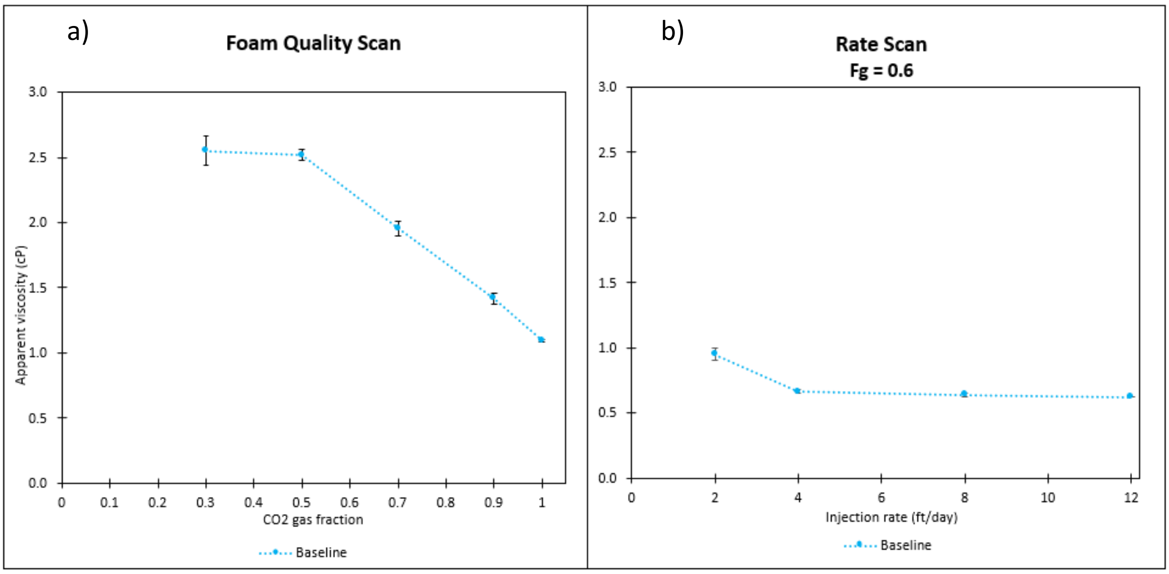

Figure 9.1 Apparent viscosity as a function of gas fraction during steady-state co-injection of CO_2 and brine in Bentheimer sandstone (SS1) at 180 bar and 40°C.

The rate scan experiment was performed with a gas fraction of 0.60. Figure 9.1b shows apparent viscosity as a function of injection rate for the baseline co-injection. The experiment was performed with injection rates increasing from 2 ft/day to 12 ft/day. The calculated apparent viscosity began at 1 cP at 2 ft/day and decreased to 0.50 at 4, 8, and 12 ft/day injection rates. In Figure 9.1b, the rate scan experiment showed that an increase in injection rate did not affect the apparent viscosity.

9.2 Surfactant Stabilized Foam

Surfactant was dissolved in the aqueous phase and compared to the baseline to confirm foam generation, determine the optimal gas fraction, and determine which injection rate generated the strongest foam (highest apparent viscosity). Injection rates of 2 ft/day and 4 ft/day in the foam quality scans were used as described in Section 7.5.

Figure 9.2a shows apparent viscosity as a function of gas fraction for the foam quality scans at 2 ft/day (green curve) and 4 ft/day (purple curve), both with foaming solutions containing a 0.25 wt.% surfactant concentration. At the injection rate of 2 ft/day (Figure 9.2a, green curve), the apparent viscosity was 60 cP at the first injected gas fraction, confirming foam generation compared to the baseline (blue curve). Apparent viscosity increased with increasing gas fraction until it reached the peak value of 80 cP, where the strongest foam was generated, at a gas fraction between 0.50 to 0.60. Therefore, at an injection rate of 2 ft/day, the optimal gas fraction was determined to be a gas fraction of approximately 0.60.

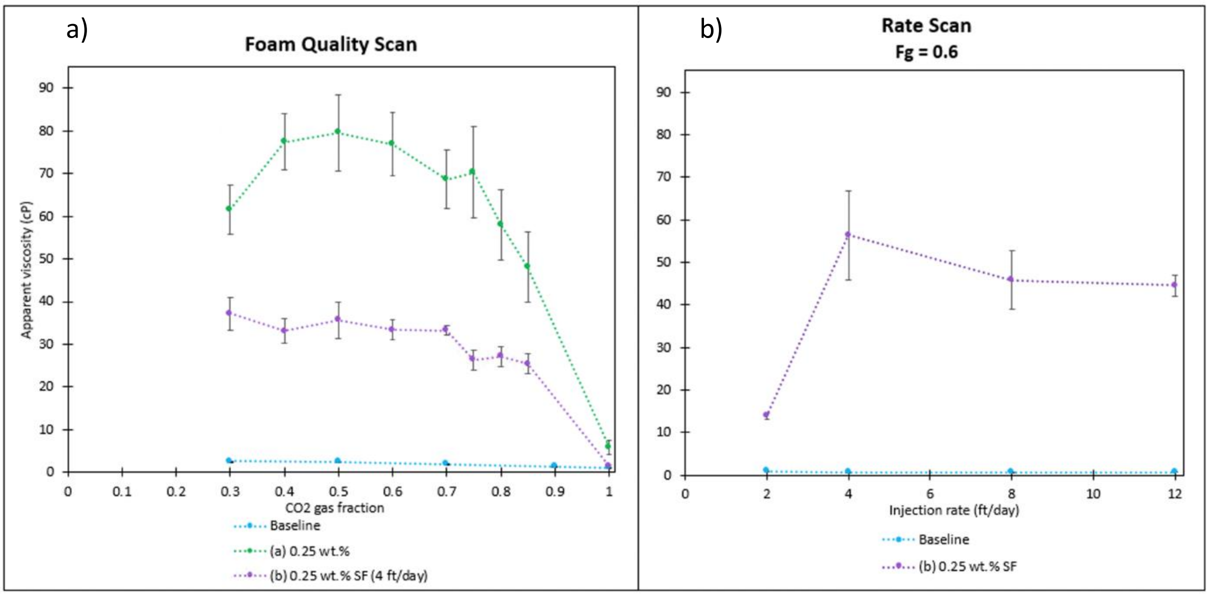

Figure 9.2 Apparent viscosity as a function of gas fraction (a) and injection rate (b) during steady-state co-injection of foaming solution and supercritical CO_2. Two Bentheimer sandstone cores were used, with similar properties and sizes. The baseline and (a) were performed on SS1 at a 2ft/day injection rate. The purple curve (b) was performed on SS2 at 4 ft/day. Both cores are described in detail in Table 7.1 in Section 7.1. The error bars on each point represent the uncertainty of the calculated apparent viscosity.

When the gas fraction increased to 0.70 and up to 1.0, the apparent viscosity decreased to 6 cP. The decrease in apparent viscosity indicated a transition into the high-quality foam regime where foam strength decreases with an increasing gas fraction (Boeije & Rossen, 2013; Osterloh & Jante, 1992; Sharma, 2019). At the final injection stage, where pure CO_2 is injected (gas fraction=1.0), the apparent viscosity remained at 6 cP. Compared to the baseline, the increased apparent viscosity indicated that immobile trapped gas was present in the core, despite 5 PV ofCO_2 injection. Similar behavior using the same surfactant supports previous findings (Boeije & Rossen, 2013; Sharma, 2019).

For the foam quality scan at an injection rate of 4 ft/day (Figure 9.2a, purple curve), the apparent viscosity for the first gas fraction of 0.30 was 37 cP, confirming foam generation compared to the baseline (blue curve). The apparent viscosity remained stable between 33 cP and 37 cP until the gas fraction reached 0.70. The optimal gas fraction which generated the strongest foam was between 0.30 and 0.70. The apparent viscosity in the interval was so similar that it was difficult to determine an optimal foam quality. The peak value in apparent viscosity was previously observed near the high-quality foam regime (Sharma, 2019). In this foam quality scan at 4 ft/day with a surfactant concentration of 0.25 wt.%, the foam strength was seemingly independent of gas fraction between 0.30 and 0.70. Next, when the injected gas fraction was increased gradually from 0.70 to 1.0, the system entered the high-quality foam regime, and the apparent viscosity gradually decreased to 1cP. The optimal gas fraction for a foaming solution with a concentration of 0.25 wt.% surfactant was 0.60 at 2 ft/day and between 0.30 and 0.70 at 4 ft/day. Compared to the foam quality scan conducted at 2 ft/day, the one at 4 ft/day had less trapped gas based on the calculated apparent viscosity at a gas fraction of 1.0, which is the same as observed in the baseline experiment.

Figure 9.2b shows apparent viscosity as a function of injection rate for the foam rate scans. As determined from the foam quality scans, a gas fraction of 0.60 was selected for the rate scan experiment. The first injection rate of 2 ft/day had an apparent viscosity of 13 cP before it increased to 56 cP at 4 ft/day, which indicated an increase in foam strength. The increase in apparent viscosity from the injection rate of 2 to 4 ft/day could also indicate a change in foam texture (Rossen, 1996). The foam strength and apparent viscosity would increase given a finer textured foam consisting of smaller bubbles. Such behavior could occur if the fluctuations in pressure or flow rate change, which was the case in the rate scan experiment. Similar behavior of apparent viscosity at low injection rates has previously been reported (Skjelsvik, 2018).

Furthermore, when the injection rate was increased to 8 and 12 ft/day, the apparent viscosity decreased to 45 cP at the highest injection rate. The decrease in apparent viscosity from 4 ft/day to 12 ft/day indicated shear-thinning behavior as observed using the same foaming solution at a similar surfactant concentration at 0.50 wt.% (Sharma, 2019). Therefore, shear-thinning in the foam was investigated to relate to near well behavior on the field scale. The flow rates and pressure gradients near the well are very high compared to the rest of the reservoir. Shear-thinning rheology is advantageous for field-scale injectivity because weaker foam is generated near the well, increasing strength as the flow rate decreases deeper into the reservoir (Hirasaki & Lawson, 1985).

The Effect of Injection Rate

The effect of injection rate on foam strength and the optimal foam quality was investigated by comparing the foam quality scans in Figure 9.2a performed at injection rates 2 and 4 ft/day. Firstly, the injection rate of 2 ft/day had a peak in apparent viscosity around 80 cP, while the 4 ft/day injection rate had a peak in apparent viscosity of 37 cP. The difference in apparent viscosity indicates that the foaming solution was shear-thinning because an increased injection rate resulted in lower apparent viscosity and foam strength.

Next, comparing Figure 9.2b at an injection rate of 4 ft/day and a gas fraction of 0.60 with an apparent viscosity of 58 cP to the equivalent point on the 4 ft/day curve in Figure 9.2a with apparent viscosity of 33 cP, there was a significant difference in calculated apparent viscosity of 25 cP. As shown by the error bars on the two points, the uncertainty in the rate scan is four times larger than for the foam quality scan with an uncertainty of 2.2 cP. The uncertainty was calculated based on pressure fluctuations during steady-state for each gas fraction or injection rate. Fluctuations in pressure affects the system and could increase foam generation by snap-off, as described in Section 4.2. Increased foam generation can result in finer textured foam with higher stability and thereby could be the reason for stronger foam at the same conditions in the rate scan compared to the foam quality scan. Similar behavior in pressure fluctuations has been observed using a similar set-up (Skjelsvik, 2018; Soyke, 2020).

9.3 Surfactant and Nanoparticle Stabilized Foam

Nanoparticles were added at two concentrations (0.015 wt.% and 0.15 wt.%) to the 0.25 wt.% foaming solution to determine whether nanoparticles impacted the optimal gas fraction and increased foam strength. Figure 9.3a shows apparent viscosity as a function of gas fraction for foaming solutions containing 0.25 wt.% surfactant and 0.015 wt.% nanoparticles (red curve) and 0.25 wt.% surfactant and 0.15 wt.% nanoparticles (yellow curve). The baseline without foaming agents is also shown for comparison (blue curve). In Figure 9.3a, both foaming solutions show an increase in apparent viscosity, with an increasing gas fraction from 0.30 to the optimal gas fraction. The maximum apparent viscosity was at 69 cP at a gas fraction of 0.50 for the 0.015 wt.% NP concentration (red curve) and 54 cP at gas fraction 0.60 for the 0.15 wt.% NP concentration (yellow curve). When the gas fraction was increased to 0.70, the apparent viscosity decreased gradually to 2 cP at a gas fraction of 1.0 for both foaming solutions.

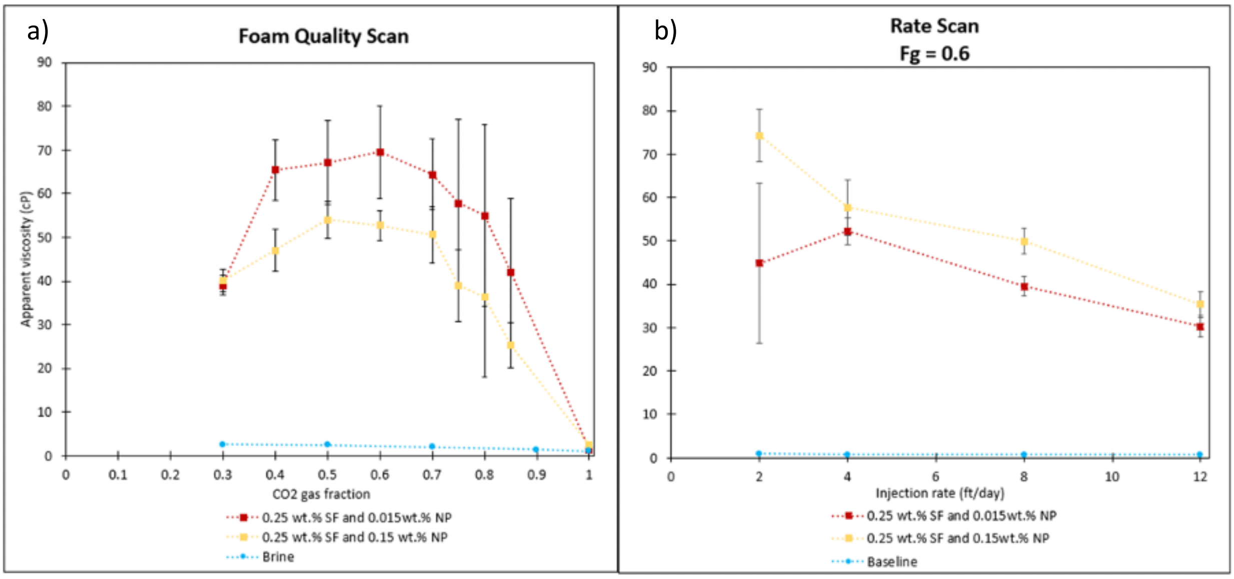

Figure 9.3 Apparent viscosity as a function of gas fraction (a) and injection rate (b) during steady-state co-injection of foaming solution with 0.15 wt.% (yellow curve) and 0.015 wt.% (red curve) nanoparticles and supercritical CO_2. All experiments were performed on Bentheimer sandstone core SS1. Properties are described in Section 7.1 in Table 7.1.

The calculated apparent viscosity at the two concentrations of nanoparticles is in the same range, but the peak value for the low concentration of 0.015 wt.% NP was 15 cP larger than for the increased NP concentration of 0.15 wt.%. The lower concentration of nanoparticles resulted in higher apparent viscosity, indicating that a higher concentration of nanoparticles did not increase foam stability. The optimal gas fraction was between 0.50 and 0.60 for both the low and high NP concentrations. Therefore, the nanoparticle concentration did not affect the optimal gas fraction.

In Figure 9.2b, the corresponding rate scans are shown. The NP concentration of 0.15 wt.% (yellow curve) shows a stable decrease in apparent viscosity from 74 cP to 35 cP for an increasing injection rate from 2 ft/day to 12 ft/day. On the other hand, the NP concentration of 0.015 wt.% (red curve) shows a slight increase in apparent viscosity from 45 cP to 52 cP at injection rates of 2 ft/day and 4 ft/day. Next, the apparent viscosity decreased steadily to 30 cP at a 12 ft/day injection rate. The apparent viscosity at 2 ft/day for the NP concentration of 0.15 wt.% was lower than at 4 ft/day but had significantly higher uncertainty. Due to the high uncertainty, it was impossible to determine whether the foam strength increased or decreased from an injection rate of 2 to 4 ft/day. However, both foaming solutions with added nanoparticles demonstrated shear-thinning rheology with an increasing injection rate.

9.4 The Effect of Injection Rate and Nanoparticles on Surfactant Stabilized Foam

Figure 9.4a shows all the foam quality scans performed in this work. Firstly, by comparing the scans performed at a 2 ft/day injection rate with a surfactant concentration of 0.25 wt.%, all had apparent viscosity peaks in the same range, varying between 54 cP and 80 cP. The highest apparent viscosity was for the foaming solution with surfactant only, and the lowest was for the surfactant and high nanoparticle solution with 0.15 wt.% nanoparticles. The difference in foam strength indicates that the nanoparticles did not increase the foam stability when added to a foaming solution with surfactant. The insignificant effect on foam strength for a similar foaming solution with the same surfactant (0.50 wt.%) and nanoparticles supports previous findings (Alcorn, Føyen, Gauteplass, et al., 2020a).

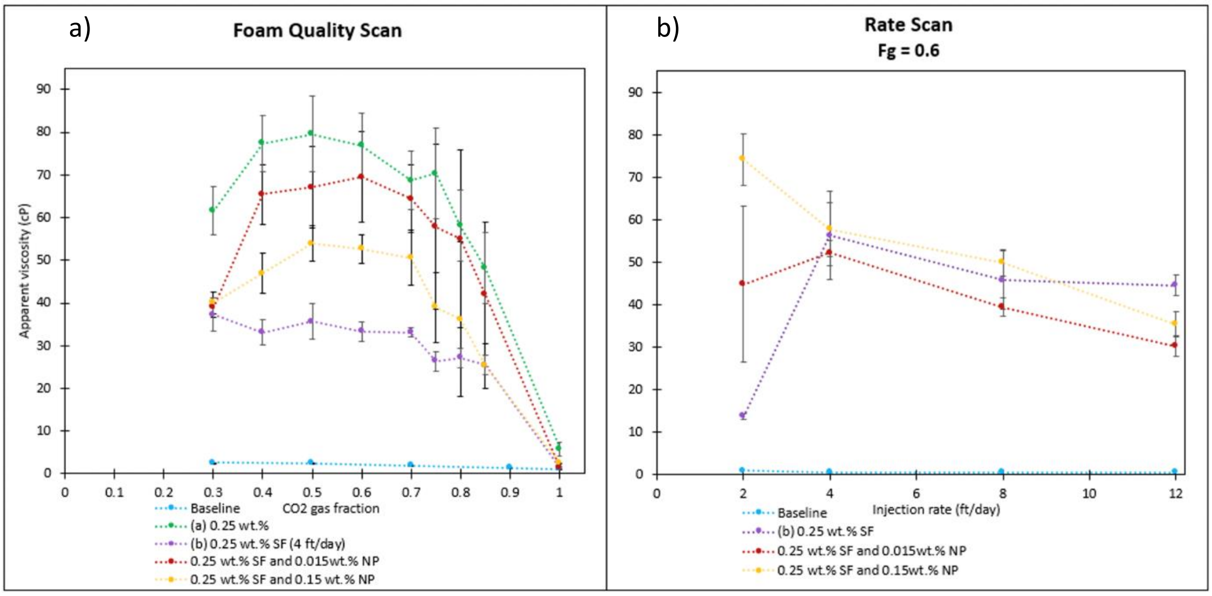

Figure 9.4 (a) Foam quality and (b) rate scans performed with different foaming solutions with surfactant and surfactant with added nanoparticles. All experiments were performed on Bentheimer sandstone cores with properties listed in Table 7.1 in Section 7.1.

Figure 9.4b shows the corresponding rate scans. The overall trend from the rate scans is that all the foaming solutions have shear-thinning behavior for increased injection rate. Also, the difference in peak apparent viscosity of 43 cP between the foam quality scans with 0.25 wt.% surfactant at 2 and 4 ft/day supports the statement of shear-thinning behavior.

Furthermore, increasing fluctuations in pressure had a positive effect on the foam strength. An increase in foam generation from snap-off described in Section 4.2 could result from pressure fluctuations (Appendix B). Capillary pressure depends on the system pressure and will be affected by the fluctuations. A rapid drop in capillary pressure is necessary for the foam to generate by snap-off, and increased pressure changes could lead to more snap-off.

10 Unsteady-State CO_2 EOR and CO_2 Storage

The objective of the unsteady-state CO_2 EOR and CO_2 storage experiments was to determine the impact of injection strategy on oil recovery and CO_2 retention. Single-cycle WAG and SAG, in addition to rapid WAG and SAG injection strategies, are presented and evaluated based on the oil recovery factor, CO_2 retention, and apparent viscosity. Further, in chapter 12, the injection strategies have been implemented in field-scale numerical simulations using a cross-sectional reservoir model.

10.1 Single-Cycle WAG and SAG

The single-cycle WAG and SAG injections consisted of approximately 1 PV brine injection or foaming solution, followed by 9 PV of supercritical CO_2 injection. Figure 10.1 shows oil recovery factor and gas saturation (primary y-axis) and apparent viscosity (secondary y-axis) as a function of PV injected for the single-cycle WAG (blue curve) and the single-cycle SAG (green curve). When the brine and surfactant injections were initiated for the Single-Cycle WAG and SAG, oil production began after 0.50 PV was injected and rapidly increased to 0.45 OOIP. Despite different injection fluids, the produced volumes were approximately the same for the Single-Cycle WAG and SAG, with a recovery factor of 0.45 OOIP. The presence of surfactant has proven to reduce the interfacial tension between oil and water to increase oil recovery. The foaming solution was only injected for 1 PV, so it is possible that the effect of the surfactant injection would be noticeable if the injection was prolonged.

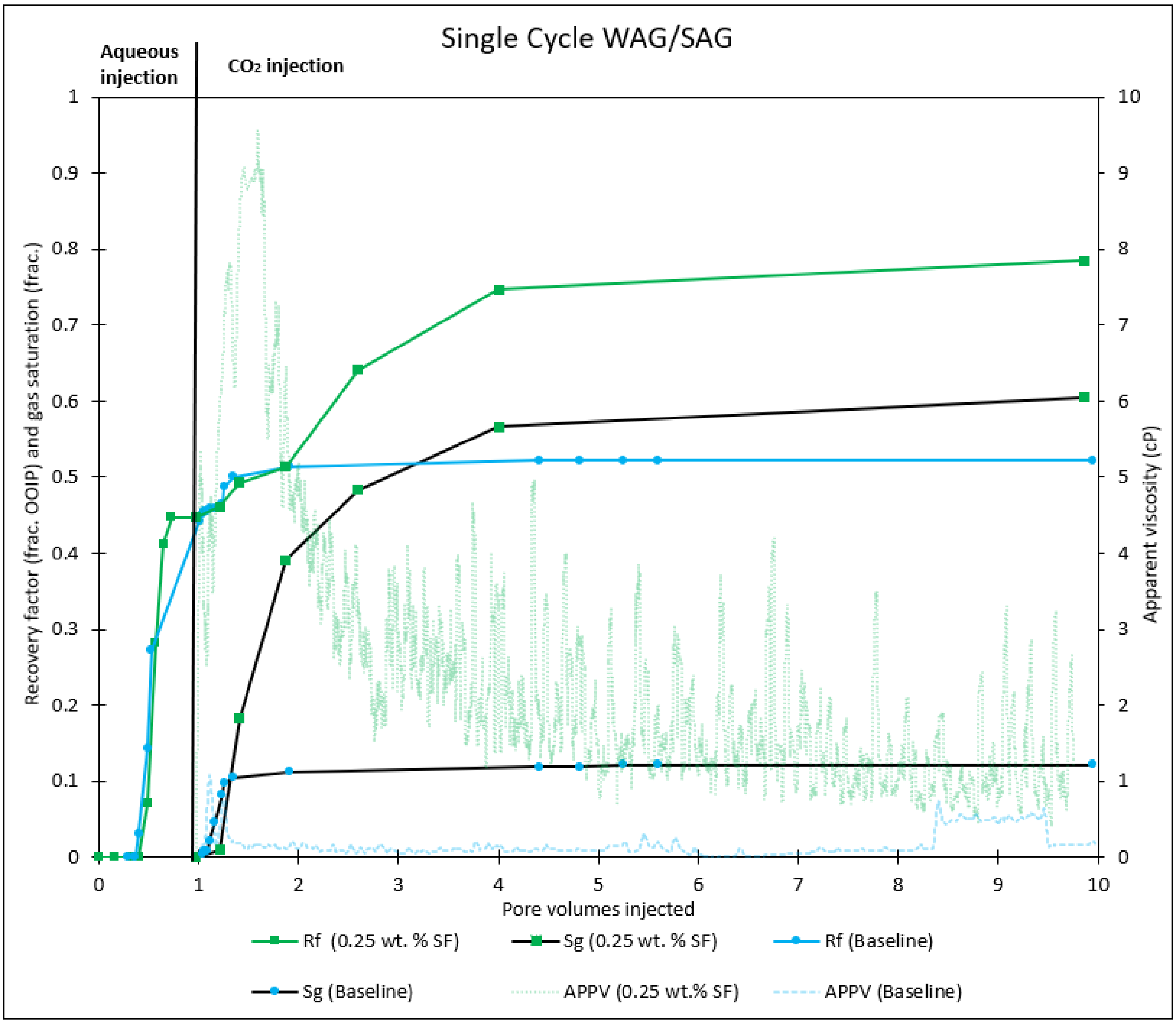

Figure 10.1 Recovery factor (colored curves) and CO_2 gas saturation (black curves) on the primary vertical axis and Apparent viscosity (dotted curves) on the secondary vertical axis as a function of Pore volumes injected. A Single-Cycle WAG (blue curves) and Single-Cycle SAG (green curves) were performed by injection of brine or foaming solution (0.25 wt.%) followed by CO_2 injection. Both experiments were performed on Bentheimer sandstone, SS2 described in Figure 7.1.

Next, when CO_2 injection was initiated, the oil recovery gradually increased to about 0.50 OOIP for both the single-cycle WAG and SAG after 2 PV injected. During the second injected pore volume, the apparent viscosity for the single-cycle SAG (dotted green curve, Figure 10.1) rapidly increased to 9 CP, confirming foam generation. The generated foam in the single-cycle SAG increased oil recovery to a final recovery factor of 0.71 OOIP after 10 PV injected. The increase in apparent viscosity by foam provided increased viscous displacement forces. However, the WAG's apparent viscosity remained around 1 cP due to no foam generation. As a result, the oil production subsided after 1 PV of CO_2 injection and ended at a total recovery factor of 0.52 OOIP. Theoretically, the miscible CO_2 injection should be able to displace 100% of the OOIP. Because the core was strongly water-wet, water shielding in the core is likely to have reduced the oil recovery in both the single-cycle WAG and SAG (Rao et al., 1992). However, based on the difference in oil recovery between the single-cycle WAG and SAG, the increased viscous forces due to foam significantly increased oil recovery in the single-cycle SAG by a recovery factor of 0.19 OOIP larger than the single-cycle WAG.

Total liquid production was also measured to determine the volume of CO_2 stored in the core. The CO_2 saturation in the single-cycle WAG rapidly increased before it stabilized at $S_g = 0.12$ after approximately 0.2 pore volumes of CO_2 had been injected. For the duration of the single-cycle WAG, the apparent viscosity remained stable below 1 cP. On the other hand, the CO_2 saturation in the single-cycle SAG increased rapidly before it gradually stabilized with an endpoint gas saturation of 0.61. The significant difference in gas saturation between the single-cycle WAG and the SAG indicated that a larger volume of water was produced during the SAG experiment, contributing to increased CO_2 saturation of 0.49 compared to the single-cycle WAG.

The difference in fluid production between the single-cycle WAG and SAG indicated that the single-cycle SAG improved volumetric sweep and contacted a larger part of the core, increasing displacement due to viscous forces. The increase in the oil recovery factor by 0.29 OOIP indicated a better sweep where more oil was contacted and displaced in the single-cycle SAG compared to the WAG. The displacement front development in the single-cycle SAG was likely piston shaped, whereas the single-cycle WAG likely had more instabilities due to viscous fingering. The effect of foam was significant for both increasing oil recovery and CO_2 storage by increasing oil recovery by 19 percentage points (pp) and CO_2 retention by 49 pp.

10.2 Rapid WAG and SAG

The rapid alternating injection experiments consisted of a baseline rapid WAG injection and two rapid SAG injections at two different surfactant concentrations (0.25 wt.% and 0.50 wt.%) to determine the effect of surfactant concentration on oil recovery factor and CO_2 retention. Figure 10.2 shows recovery factor and gas saturation (primary y-axis), and apparent viscosity (secondary y-axis) as a function of PV injected for the rapid WAG (blue curve), the rapid SAG with 0.25 wt.% surfactant concentration (green curve) and the rapid SAG with 0.50 wt.% surfactant concentration (red curve). All rapid injection strategies were conducted after the core was waterflooded for one pore volume. The waterflood recovery was the same for all three cases, with a recovery factor of about 0.50 OOIP.

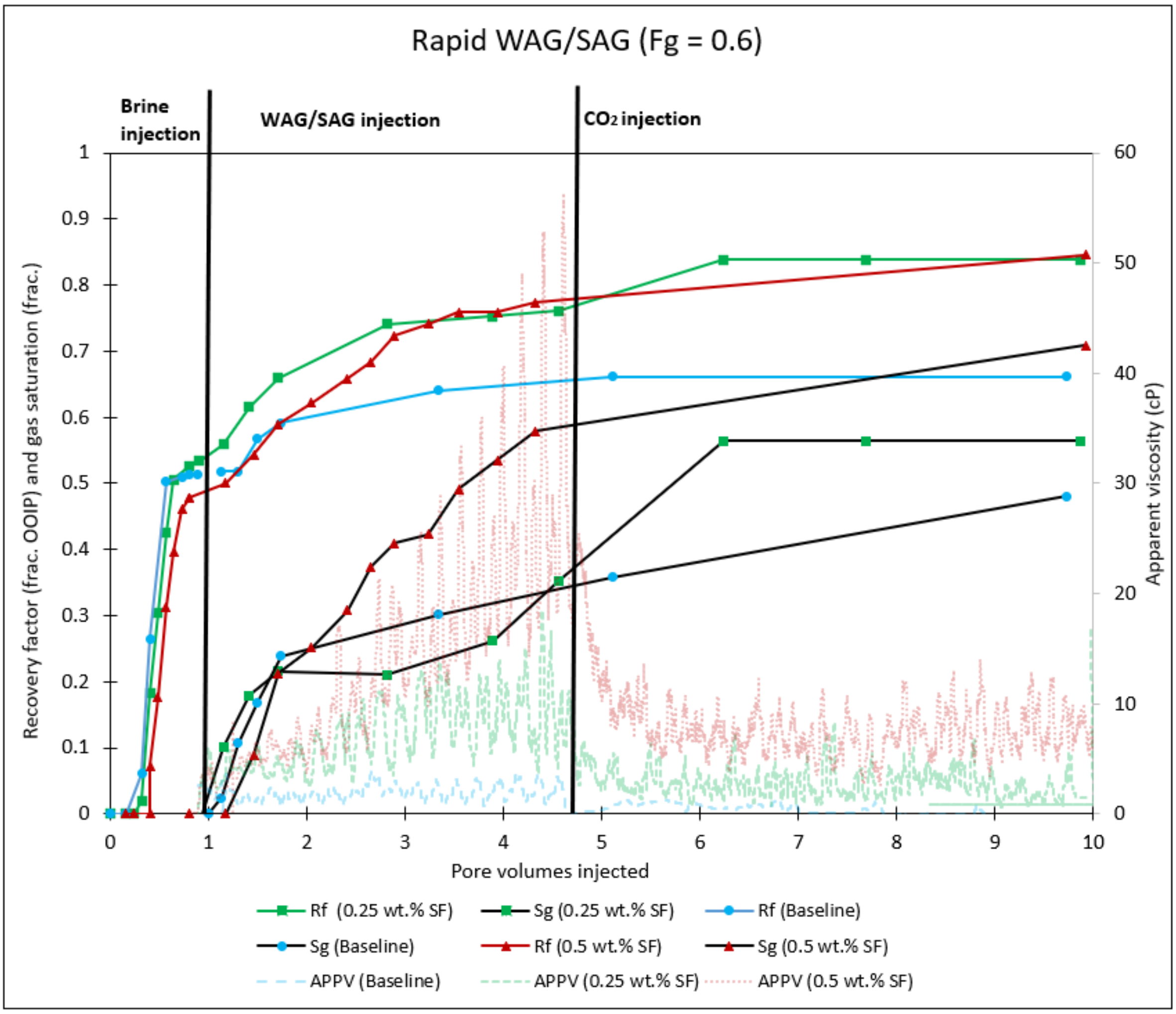

Figure 10.2 Recovery factor (colored curves) and CO_2 gas saturation (black curves) on the primary vertical axis and Apparent viscosity (dotted curves) on the secondary vertical axis as a function of pore volumes injected. A Rapid WAG (blue curves) and Rapid SAGs with 0.25 wt.% (green curves) and 0.50 wt.% (red curve) surfactant were performed, followed by CO_2 injection. All experiments were performed on Bentheimer sandstone, SS2 described in Figure 7.1.

During the baseline rapid WAG (blue curve), the oil recovery factor remained at 0.50 OOIP until the first WAG cycle was injected, and the recovery factor had a sharp increase before stabilizing at 0.66 OOIP. The apparent viscosity fluctuated depending on the injection fluid but stayed below 4 cP during the WAG injection. No foam was generated, and the increase and variations in apparent viscosity were likely due to the reduction of CO_2 relative permeability from the presence of brine. During the WAG injection period, the CO_2 saturation increased rapidly for the first injected pore volume and gradually increased during pure CO_2 injection. The CO_2 saturation in the core after ten injected pore volumes was 0.48.

The rapid SAG injections with surfactant concentrations of 0.25 wt.% (green curve) and 0.50 wt.% (red curve) showed a sharp increase in oil recovery when SAG was initiated, where both continued to increase throughout the SAG injection before stabilizing at 0.84 OOIP and 0.85 OOIP, respectively. The apparent viscosity increased for each injected SAG slug in both SAGs and reached a peak value of 20 cP and 55 cP for the Rapid SAG with 0.25 wt.% and 0.50 wt.% surfactant concentration, respectively. Similar results for oil recovery with foam have been reported in limestone (Skjelsvik, 2018).

The significant increase in apparent viscosity confirmed that foam was generated in both the rapid SAGs (green and red dotted lines, Figure10.2). Despite the similar oil recovery factors, the apparent viscosity was 35 cP higher for the surfactant concentration of 0.50 wt.% compared to 0.25 wt.%. Based upon no difference in oil recovery factor between the surfactant concentrations of 0.25 wt.% and 0.50 wt.%, the increase in foam strength did not increase oil recovery.

On the other hand, there was a significant increase of 15 pp in CO_2 saturation between the rapid SAG with 0.25 wt.% to 0.50 wt.% surfactant concentration (black curves). They rapidly increased CO_2 saturation at the beginning of the SAG injection before the curves separated after 0.80 pore volumes after 4 SAG cycles were injected. While the 0.50 wt.% surfactant concentration (red curve) continued to increase in gas saturation, the 0.25 wt.% surfactant concentration (Green curve) remained constant for almost two pore volumes before increasing further. A possible reason for the delayed increase could be that the foam did not have sufficient strength to displace fluid. Also, the high mobility of supercritical CO_2 could prevent liquid production if viscous fingers and gas channels propagated through the core until sufficient foam strength was obtained. After ten injected pore volumes, the final gas saturation in the core was 0.56 and 0.71 for the 0.25 wt.% and 0.50 wt.%, respectively.

The oil recovery factors were the same for both concentrations, and a difference in water production can explain the difference in gas saturation. The water production was measured during the experiments but was not included in Figure 10.2. Based on the difference in CO_2 gas saturation, stronger foam increased CO_2 retention by a fraction of 0.15 from a surfactant concentration of 0.25 wt.% to 0.50 wt.%. Compared to the baseline rapid WAG, with no foam present, the maximum gas fraction was 0.48, and the presence of foam increased CO_2 retention. However, the rapid WAG did provide significant CO_2 mobility control to displace significant volumes of oil and water.

10.3 The Effect of Injection Strategy and Surfactant Concentration on Oil Recovery and CO_2 Storage

Figure 10.3a shows a bar chart summarizing the oil recovery factors for the Single-Cycle and Rapid WAGs (blue bars) and SAGs with 0.25 wt.% surfactant (green bars) and 0.50 wt.% surfactant (red bar). WAG/SAG. The Single-Cycle WAG/SAG was compared to the Rapid WAG/SAG to determine the most efficient injection strategy regarding oil recovery and CO_2 retention. The Single-Cycle WAG had an oil recovery factor of 0.52 OOIP, whereas the rapid WAG had a recovery factor of 0.66 OOIP, which means that the rapid WAG produced 14 percentage points (pp) more than the Single-Cycle WAG. Furthermore, because the Rapid WAG consisted of several 0.20 pore volume slugs, the CO_2 could have contacted and displaced a larger amount of the oil.

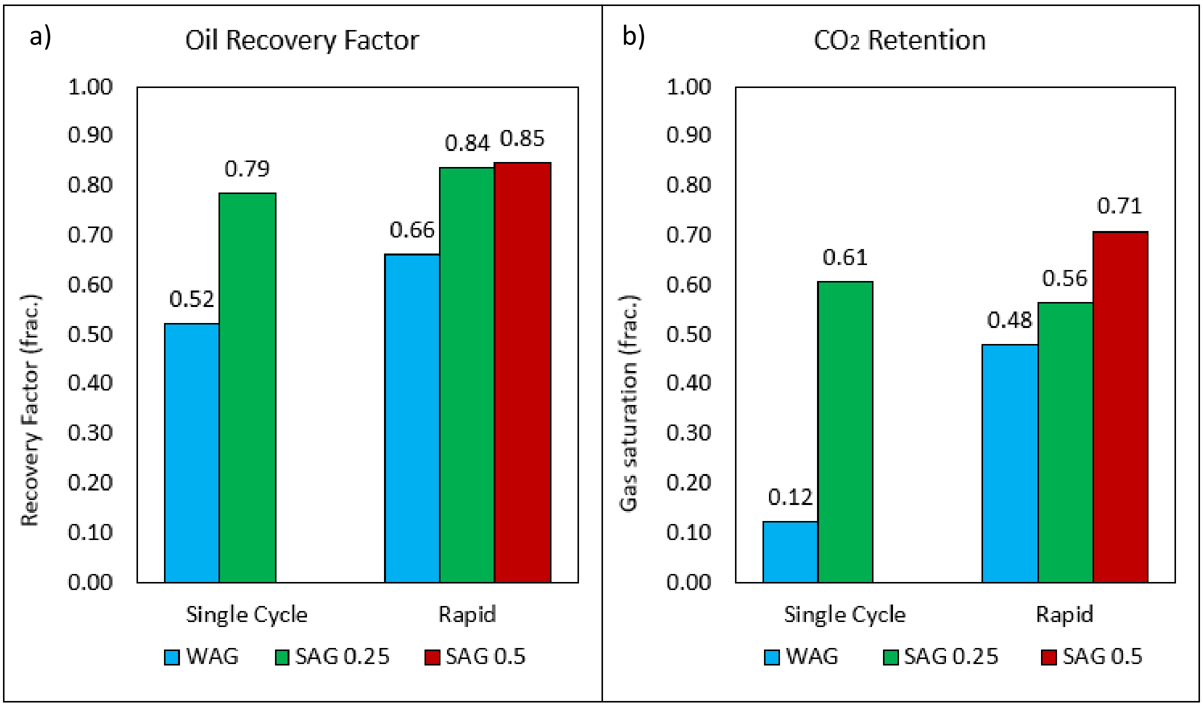

Figure 10.3 Summarizing bar charts of Oil recovery factor and CO_2 retention for Single-Cycle WAG/SAG and Rapid WAG/SAG. Blue bars represent WAG, green represents 0.25 wt.% surfactant concentration, and red represents 0.50 wt.% surfactant concentration.

The Single-Cycle SAG with a 0.25 wt.% surfactant concentration produced 0.79 OOIP, compared to the Rapid SAGs with a 0.25 wt.% and 0.50 wt.% surfactant concentration, which produced 0.84 OOIP and 0.85 OOIP, respectively. Despite different surfactant concentrations, the Rapid SAGs essentially had the same oil recovery factor, which indicated that an increase in surfactant concentration did not increase oil recovery. The increase in oil recovery was 5 pp from the Single-Cycle SAG to the Rapid SAG, both at a surfactant concentration of 0.25 wt.%. The difference was minor, indicating that oil recovery was not sensitive to injection strategy in these experiments.

Based on the oil recovery factors from the two injection strategies, both the Rapid WAG and SAG had a higher oil recovery factor than the corresponding Single-Cycle WAG and SAG. However, the Single-Cycle SAG produced 13% more oil than the Rapid WAG, indicating that foam increased oil recovery. The Rapid SAG with a 0.25 wt.% surfactant concentration had the same oil recovery factor as the Rapid SAG with a 0.50 wt.% surfactant concentration, which indicated that the change in surfactant concentration did not change the impact the oil recovery. The oil recovery increased for SAG compared to WAG, both for the Single-Cycle and the Rapid injection strategies. However, by comparing the two WAGs and the SAGs with 0.25 wt.% surfactant, the oil recovery was 14% and 5% higher for the Rapid injections than the Single-Cycle, confirming that the Rapid injection strategy was most effective for WAG and SAG.

Figure 10.3b shows a bar chart summarizing CO_2 retention for the Single-Cycle and Rapid WAGs (blue bars) and SAGs with 0.25 wt.% surfactant (Green bars) and 0.50 wt.% surfactant (Red bar). The Single-Cycle WAG had a 12% CO_2 retention, while the Rapid WAG had 48% CO_2 retention. The significant difference of 36 pp in CO_2 retention confirms that the Rapid WAG displaced significantly more liquid than the Single-Cycle WAG. Furthermore, the increase in CO_2 retention indicated that the relative permeability reduction of CO_2 was more prominent for the Rapid WAG than the Single-Cycle WAG.

Next, the Single-Cycle and Rapid SAGs, both with a 0.25 wt.% surfactant concentration, had 61% and 56% CO_2 retention. The difference in CO_2 retention was only 5 pp, indicating that the injection strategy did not significantly affect the CO2 retention. The maximum apparent viscosity of 10 cP indicated that the foam generated in both the Single-Cycle and Rapid SAG had the same strength. However, the apparent viscosity in the Single-Cycle SAG had a sharp increase for half a pore volume, followed by a rapid dry-out after one injected pore volume of CO_2. On the contrary, the Rapid SAG gradually increased apparent viscosity to 10 cP for the first 10 SAG slugs before the apparent viscosity stabilized and fluctuated around 10 cP for the remaining SAG cycles. The injected slugs had a gas fraction of 0.60, where the remaining 40% were foaming solution. Therefore, it is possible that the prolonged injection of liquid resulted in lower CO_2 retention.

The Rapid SAG with a surfactant concentration of 0.50 wt.% surfactant had a 71% CO_2 retention, which was 10 pp and 15 pp more than the SAGs with 0.25 wt.% surfactant concentration. The increased surfactant concentration resulted in larger CO_2 retention due to increased liquid displacement. The foam generated in the Rapid SAG with the 0.50 wt.% surfactant concentration had a maximum apparent viscosity of 50 cP. The apparent viscosity increased for each SAG slug before reaching the peak value, which was five times larger than for both SAGs with 0.25 wt.% surfactant concentration. The difference in CO_2 retention and apparent viscosity confirmed that stronger foam with higher apparent viscosity resulted in larger CO_2 retention for the performed experiments, which is favorable for CO_2 storage.

The injection strategies and surfactant concentrations were compared to determine the most efficient injection strategy regarding oil recovery and CO_2 retention. Firstly, the Rapid WAG recovered 15 pp more oil and retained 36 pp more CO_2 than the Single Cycle WAG. However, all of the SAGs recovered more oil and had higher CO_2 retention than the WAGs, confirming that the presence of foam is favorable for both oil recovery and CO2 storage. The Single-Cycle and Rapid SAGs with a 0.25 wt.% surfactant concentration generated foam with a maximum strength of 10 cP. They had similar results with oil recovery factors 0.79 and 0.84 and CO_2 retention of 61% and 56%, indicating that the results were independent of injection strategy. The Rapid SAG with a 0.50% surfactant concentration generated the strongest foam and had a maximum apparent viscosity of 50 cP. The oil recovery factor of 0.85 was the same as the SAGs with 0.25 wt.% surfactant concentration, indicating that increased foam strength did not improve oil recovery. However, the CO_2 retention of 0.71% was significantly increased from a surfactant concentration of 0.25 wt.% to 0.50 wt.% by a 10-15 pp increase.

11 In-Situ Imaging – Foam Generation and Propagation

The objective of the in-situ imaging experiments was to visualize and study the propagation of CO_2 with and without foam and to visualize foam generation in porous media.

11.1 Quantification of Core Properties with PET/CT

In the imaging experiments, two different core samples were used, and Volumes of interest (VOI) were used to investigate the core properties of the whole cores relative to each other. Two Bentheimer sandstone cores were used for the Single-Cycle WAG (SS3) and the Single-Cycle WAG and SAG (SS4) injection strategies. The core properties are described in Table 7.1 in Section 7.1. Firstly, because two different core samples were used, the homogeneity was evaluated to determine whether they were similar enough for comparison.

Figure 11.11 shows the normalized signal intensity as a function of pore volumes injected for VOIs covering the core volumes. The radioactively traced brine and foaming solution (0.50 wt.%) were injected beginning at zero pore volumes for the Single Cycle WAG (Figure 11.1, blue curve) and SAG (Figure 11.1, green curve). The signal intensity increased as the traced liquids displaced brine until a normalized signal intensity of 1.0, where the cores were saturated with traced brine and foaming solution. The signal intensity increased following a linear trend for both the Single-Cycle WAG and SAG. However, the increase for the brine injection was slightly sharper than for the foaming solution and began to stabilize after 1.4 pore volumes were injected. The signal intensity for the Single-Cycle SAG began to stabilize at 1.5 pore volumes injected, which confirmed that the difference in core properties was minor compared to the WAG. The variation could indicate that the Single-Cycle WAG had slightly poorer sweep efficiency than the SAG, but the difference is insignificant. Based on the data from the VOIs, the cores show similar enough behavior to compare the Single-Cycle WAG to the Single-Cycle SAG.

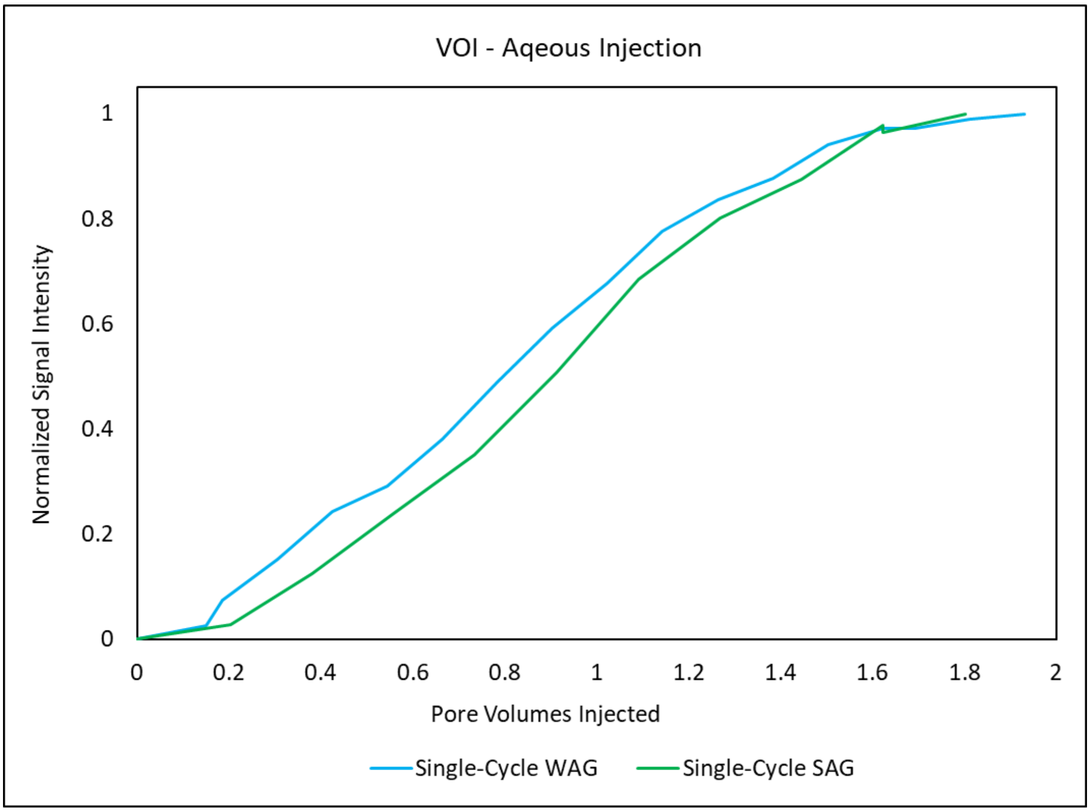

Figure 11.1 Normalized signal intensity as a function of pore volumes injected for VOIs covering the whole core during miscible brine (Single-Cycle WAG, blue curve) and surfactant injection (Single-Cycle SAG, green curve).

Figure 11.2 shows the change in normalized signal intensity as a function of pore volumes injected during CO_2 injection for the Single-Cycle WAG (blue curve) and SAG (green curve). The cores were initially saturated with brine and foaming solution at the normalized signal intensity equal to 1.0. When CO_2 entered the core, the signal intensity decreased because the traced liquid was displaced by $CO_{2,}$ which was not detected by the PET scanner. The normalized signal intensity corresponded to a change in water saturation, and the decrease in signal correlates to decreasing water saturation (Brattekås et al., 2021). After one injected pore volume, the brine saturation remained high with a normalized signal intensity was 0.70. CO_2 breakthrough was rapid during the CO_2 injection, which indicated poor sweep efficiency.

On the contrary, the Single-Cycle SAG had a much lower foaming solution saturation after CO_2 injection with a normalized signal intensity of 0.33. CO_2 breakthrough was significantly delayed compared to the WAG, indicating improved sweep efficiency with the SAG injection strategy. The measured differential pressure was also higher for the SAG, confirming foam generation (Appendix A).

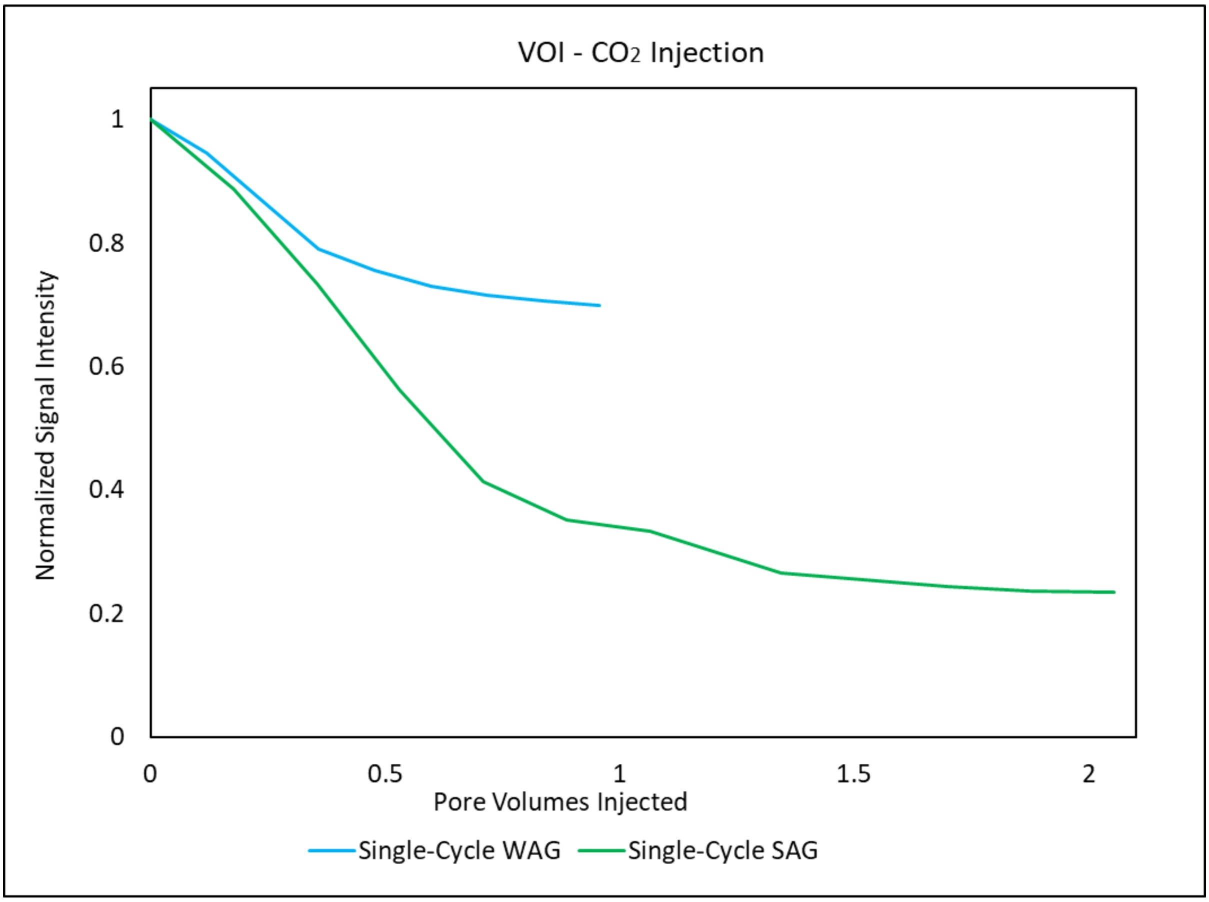

Figure 11.2 Normalized signal intensity as a function of pore volumes injected for Single-Cycle WAG (blue curve) and Single-Cycle SAG (green curve) during CO_2 injection.

The normalized signal reduction for the Single-Cycle WAG of 0.30 indicated poor sweep efficiency, likely due to viscous fingering and gravity override (Enick et al., 2012). The Single-Cycle SAG showed a significant decrease in normalized signal intensity of 0.67, which indicated a more piston-shaped displacement of foaming solution by CO_2. Observed CO_2 breakthrough and measured differential pressure confirmed foam generation in the Single-Cycle SAG. The reduction in relative permeability of CO_2 by foam resulted in a significant difference in liquid displacement between the WAG and SAG.

11.2 Baseline – Single-Cycle WAG

Figure 11.3 shows the normalized signal intensity as a function of pore volumes injected, with each curve representing a position along the core length (each of the seven ROIs presented in Figure 7.7 also described in Section 7.7). When the traced brine entered the core, the signal intensity increased first for ROI1 and ROI2 (close to the inlet). As the traced brine propagated further into the core, the signal intensity in each core cross-section (i.e., the remaining ROIs) increased. At 1.5 PV injected, the normalized signal intensity for all ROIs was near 1.0, confirming that the core was fully saturated with the traced brine. The PET signal increase observed for the different core segments aligns with observations made from the VOI (Section 11.1) and corresponded to a miscible displacement (Section 3.2).

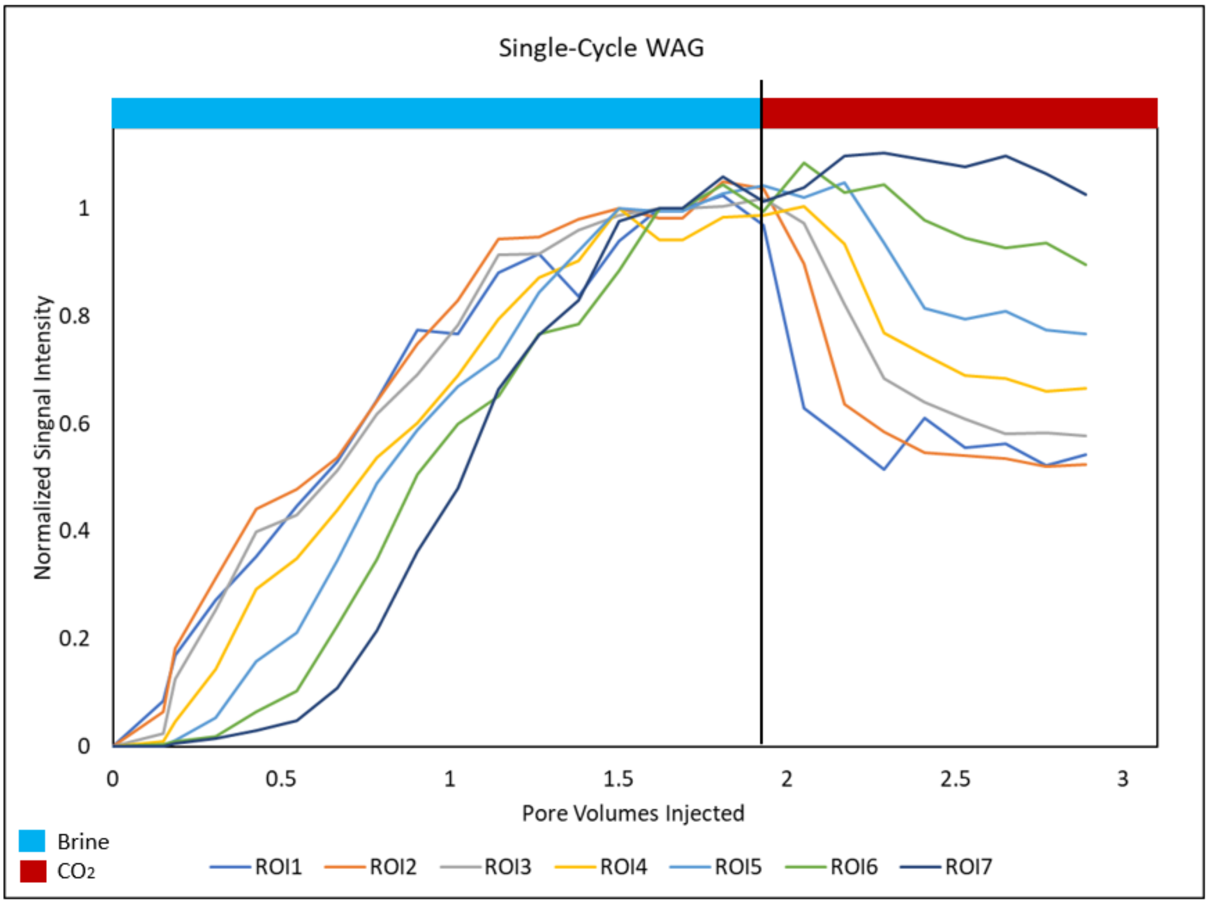

Figure 11.3 Normalized signal intensity as a function of pore volumes injected for ROIs corresponding to axial cross-sections through the core. The Single-Cycle WAG was performed on Bentheimer sandstone core SS3; a detailed core description is in Table 7.1 in Section 7.1.

After almost two pore volumes of traced brine were injected, CO_2 injection was initiated, as indicated by the black line in Figure 11.3. When CO_2 entered the core, traced brine was displaced, and the PET signal intensity decreased. First, the signal intensity near the inlet (ROI1 and ROI2) began to decrease rapidly before stabilizing at a normalized signal intensity of 0.55. The rapid decrease in PET signal corresponded to a rapid decrease in brine saturation.

At 2.2 PV injected, the brine saturation decreased further into the core (ROI3, ROI4, ROI5) and towards the outlet (ROI6) but stabilized at a normalized intensity of 0.58, 0.67, 0.77, and 0.89. At the outlet (ROI7), the traced brine saturation increased with a signal intensity of 1.1 before decreasing to 1.0. The difference in normalized signal intensity between the inlet (ROI1) and outlet (ROI7) was 0.42, and the signal intensity proved an increase in brine saturation at the outlet relative to the inlet. The difference in signal intensity confirmed a difference in water saturation through the core, where more brine was displaced close to the inlet than towards the outlet, where the signal intensity and water saturation did not change. The variation in signal intensity throughout the core also confirmed that brine's displacement by CO_2 was uneven because the signal, representing the brine saturation, remained between 70% and 90% after the CO_2 injection.

Figure 11.4 shows PET/CT images from the end of brine injection (t = 1) before CO_2 injection was initiated until the end of CO_2 injection (t = 5). When CO_2 entered the core (t = 2), the signal decreased close to the inlet. As CO_2 propagated further into the core (t = 3, t = 4), the signal decreased, forming an unstable front, where large green areas indicated poor brine displacement. Finally, at the end of the injection (t = 5), the outlet side had a strong signal response, although the CO_2 injection could indicate an accumulation of brine close to the outlet, which could be due to capillary end effects (Cheng et al., 2015) or high CO_2 mobility. The PET/CT images visualize the same trends as observed in the signal intensity plot (Figure 11.3), confirming assumptions of poor sweep efficiency.

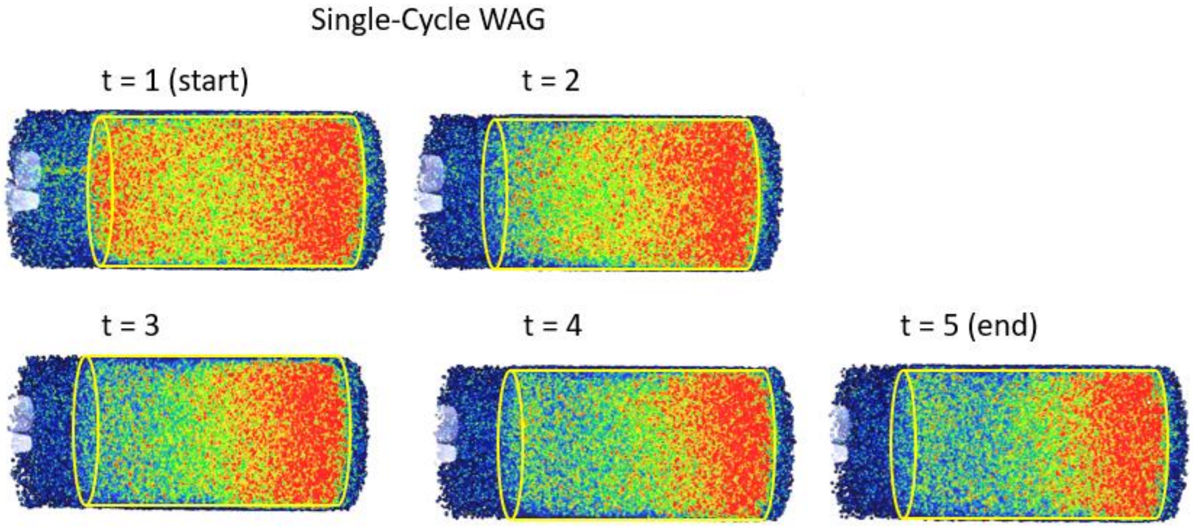

Figure 11.4 PET/CT images in 3D from the CO_2 injection into brine saturated cores at five relative points in time (t), from start to end. Red indicated a strong signal response, and blue indicated a low signal.

11.3 Single-Cycle SAG

In Figure 11.5, the Single-Cycle SAG is presented by the normalized signal intensity as a function of pore volumes injected, with each curve representing a position (ROI1-ROI7) along the core length and ROI8 representing the inlet tubing (grey dotted curve) before the core. Firstly, traced foaming solution with a 0.50 wt.% surfactant concentration was injected for almost 2 PV. The foaming solution mainly consisted of brine (Section 7.3, Table 7.2), making the displacement of brine by foaming solution a miscible displacement process. Inside the core, the signal intensity increased gradually from 0.0 to 1.0 from the inlet to the outlet side (ROI1 to ROI7). The increase in signal corresponded to the increase in the saturation of surfactant concentration in the core. However, the normalized signal intensity was not 1.0 for all ROIs simultaneously, which indicated that the core was not uniformly saturated with the foaming solution prior to CO_2 injection.

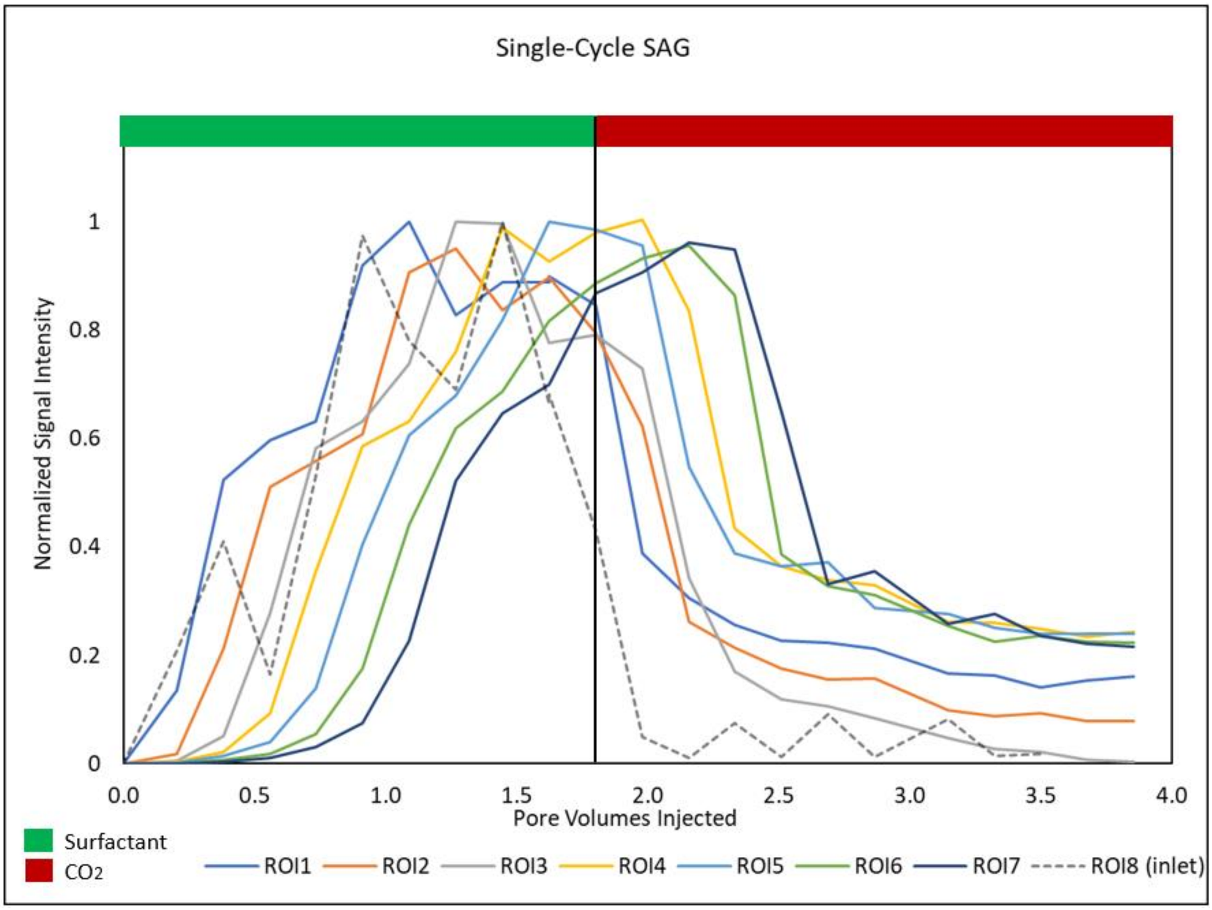

Figure 11.5 Normalized signal intensity as a function of pore volumes injected for 7 ROIs (Section 7.7). Signal increases with increasing concentration of FDG traced foaming solution. The Single-Cycle SAG was performed on Bentheimer sandstone core SS4; a detailed core description is in Table 7.1 in Section 7.1.

At 0.5 PV injected, the signal intensity decreased from 0.40 to 0.20 in the inlet tubing, which propagated into the core and caused a shift in intensity for the ROIs inside the core. The signal intensity change occurred in the tubing before entering the core and was unrelated to core properties. Again, at 1 PV injected, the signal intensity in ROI8 dropped from 1.0 to 0.65, which caused another decrease in signal intensity for the ROIs inside the core. The effect was most pronounced near the inlet (ROI1) and decreased as the traced foaming solution propagated further into the core towards the outlet (ROI7), where there was no decrease in signal intensity. The large and abrupt signal intensity changes in the inlet tubing (ROI8) indicated instability of the injected fluid with tracer. If the foaming solution with tracer was not uniformly mixed, it would explain why the signal intensity changed so abruptly during the injection period. Also, if the injected tracer concentration was not uniform, the signal intensity cannot relate directly to surfactant saturation.

Next, when the CO_2 injection was initiated, indicated by the black line in Figure 11.5, the surfactant saturation rapidly decreased from a normalized signal intensity of 1.0 near the inlet (ROI1, ROI2). The signal intensity increased near the outlet (ROI6, ROI7), indicating that the core was not fully saturated with traced foaming solution prior to CO_2 injection. However, the signal intensity decreased in ascending order from ROI1 to ROI7, indicating a piston-shaped displacement by the foaming solution. The decrease continued for 1 PV of CO_2 injection before stabilizing between 0.15 and 0.23 after 2 PV injected. The generation of foam during the CO_2 injection would explain the displacement behavior. CO_2 has higher mobility than the foaming solution, and the displacement process would likely be dominated by viscous fingering and gravity override without the presence of foam. Based on the observed development in normalized signal intensity for the Single-Cycle SAG, foam was generated during the CO_2 injection. The presence of foam resulted in a normalized signal reduction from 1.0 to 0.15-0.23, indicating that CO_2 displaced around 80% of the traced solution.

Figure 11.6 shows the 3D PET/CT images at different injection stages of the Single-Cycle WAG. At the start (t = 1), the core was saturated with the traced foaming solution prior to CO_2 injection. As CO_2 entered the core, the signal decreased close to the inlet (t = 2). As CO_2 propagated further, a sharp front began to develop (t = 3, t = 4), displacing most of the signal (blue color) from the swept areas. Towards the end of the CO_2 injection (t = 5), only the cross-sectional area close to the outlet had a strong signal (red color), whereas the rest of the core was dominated by a lack of signal (blue color). However, even after 2 PV of CO_2 injection, some signal is still present at the outlet, possibly due to capillary end effects. Overall, the signal intensity of surfactant was significantly decreased during CO_2 injection due to foam.

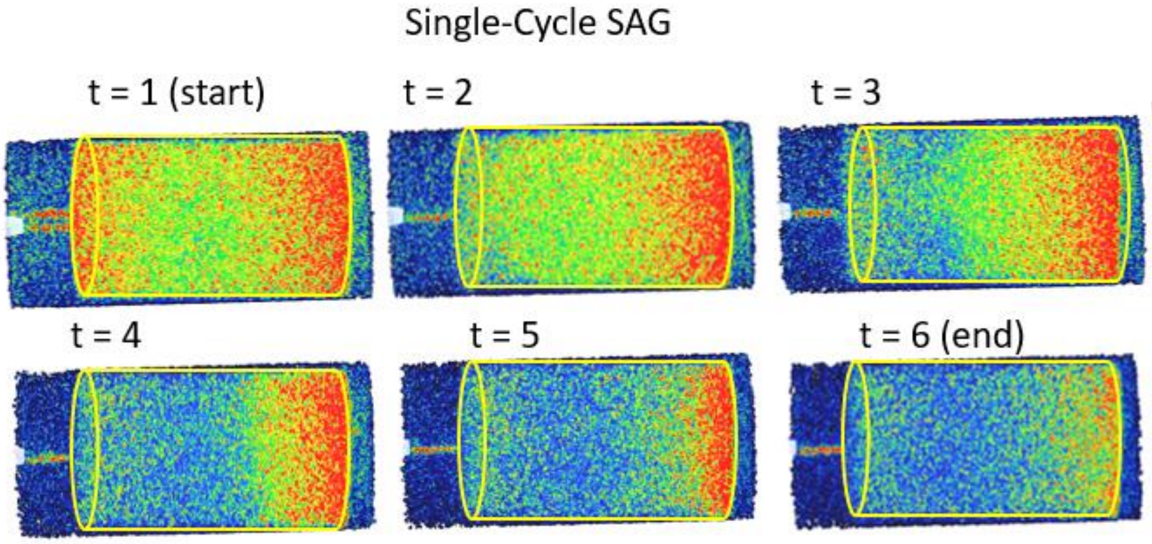

Figure 11.6 PET/CT images in 3Dfrom the CO_2 injection into foaming solution at six different times, from start to end. Red indicated a strong signal response, and blue indicated a low signal.

11.4 The Effect of Surfactant on CO_2 Propagation

The signal intensity curves and PET/CT images determined the effect of surfactant on CO2 propagation. First, the VOIs were presented in Section 11.1, where the two Bentheimer Sandstone cores were determined to have similar properties for comparison. During the CO_2 injection in Figure 11.1, foam generated in the Single-Cycle SAG resulted in a much lower normalized signal intensity of 0.33 compared to 0.70 in the Single-Cycle WAG. The foam increased the water displacement and likely affected the CO_2 propagation in the core.

Next, the signal intensity was further investigated for both cases, with 7 ROIs placed throughout the two cores. The signal intensity and PET/CT images both indicated poor sweep efficiency during CO_2 injection in the Single-Cycle WAG. In addition, the Single-Cycle SAGs signal intensity indicated a piston-shaped displacement, where most of the traced foaming solution was displaced by foam.

12 Numerical Simulation – Injection Strategy Sensitivity

In numerical simulations, three injection strategies were investigated to determine which strategy reduced CO_2 mobility for increased CO_2 retention and oil recovery. The field-scale simulation cases implemented injection strategies also used at the core scale. The injection strategies were described in Section 8.4 and included a baseline Rapid WAG and SAG, Single-Cycle WAG and SAG, and co-injections of brine and CO_2, and foaming solution and CO_2. The Base Case Rapid WAG and SAG follow the injection scheme from the field pilot (Section 8.1). The base model was history matched to field data from the historical waterflood and CO_2 injection (Sharma et al., 2020). Field-level performance metrics, including bottom hole pressure (BHP), gas-oil-ratio (GOR), and cumulative oil and water production, were used to determine whether foam was generated, and which injection strategies had higher oil recovery and CO_2 retention. CO_2 tracers were also used to identify variations in CO_2 breakthrough time to determine CO_2 mobility reduction from foam. CO_2 retention was calculated to determine CO_2 storage potential as described in Section 3.5.

12.1 Base Case – Rapid WAG and SAG

The Rapid WAG and SAG injection scheme consisted of 11 cycles of brine or foaming solution (0.50 wt.% surfactant) injection, followed by CO_2. Each cycle targeted a gas fraction of 0.70 and was described in detail in Section 8.4.

Bottom Hole Pressure

The bottom hole pressure for the baseline WAG and SAG were compared to confirm whether foam was generated. Figure 12.1 shows BHP as a function of pore volumes injected (PV) injected for the baseline WAG (blue curve) and the base case SAG (green curve). Also shown is the injection rate (gray curve, secondary y-axis). The different injection schemes are indicated by the colored bars on the top of Figure 12.1. During the first SAG slug, there was an increase in BHP of 30 psi, whereas the WAG's BHP remained stable. The BHP of the SAG continued to increase with each injected slug for the entire injection scheme until a pressure of approximately 3100 psi, whereas the WAG's BHP remained at 2400 psi. A higher BHP indicated foam generation and a larger resistance to flow. Because the BHP depends on fluid mobility and velocity in the system, a change in injection rate would affect the BHP value. The injection rate varied silightly during the injections but remained relatively stable, at around 10 RB/day. The effect of injection rate can be observed in the blue curve for WAG during the last three injected slugs. The difference in injection rate from 8 to 10 RB/day between water and CO_2 for the three last cycles corresponded to three noticeable decreases in BHP. However, the change in injection rate resulted in insignificant changes in BHP compared to the effect of foam observed for the Rapid SAG.

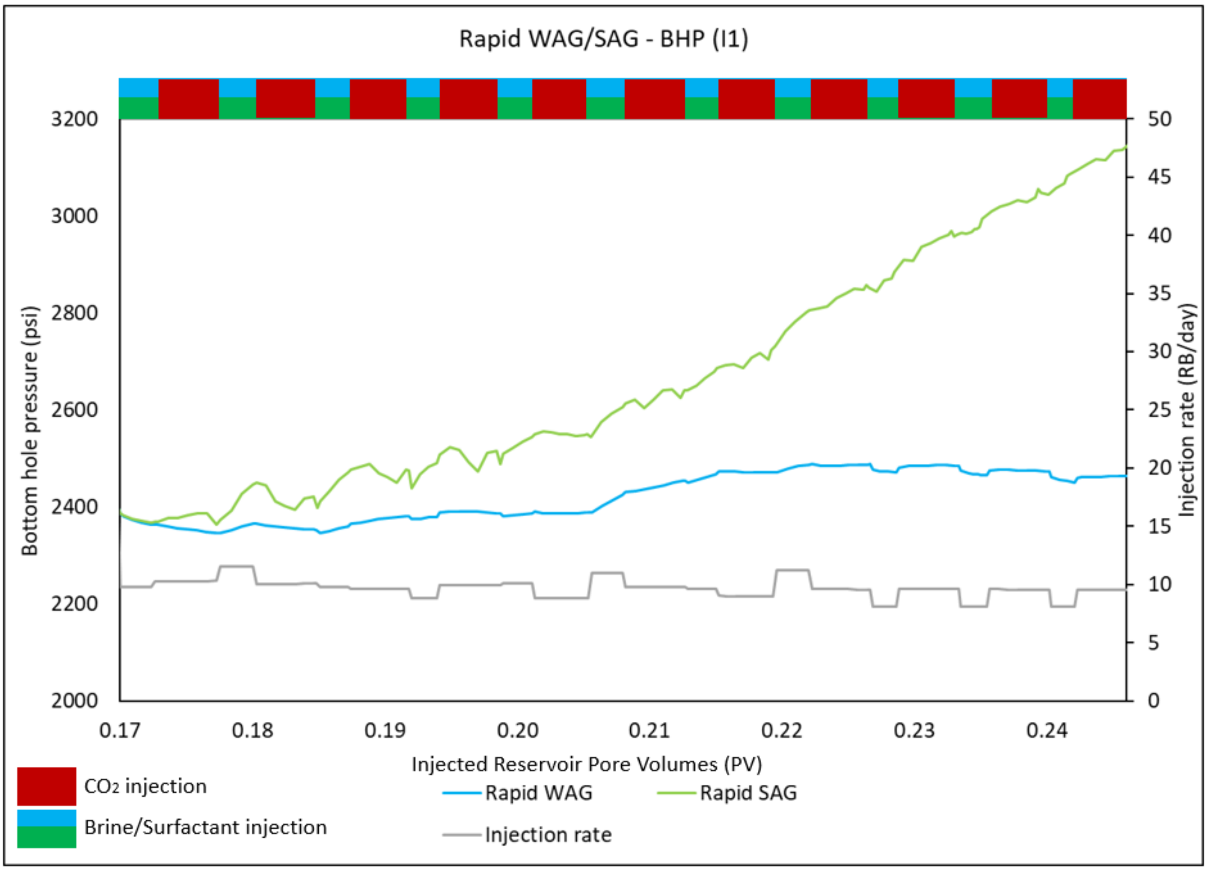

Figure 12.1 Bottom hole pressure (BHP) (blue and green curves, Primary, y-axis) and injection rate (grey, curve secondary, y-axis) for the Rapid WAG (blue curve) and SAG (green curve) injection strategies during the pilot. The injection scheme is indicated by the colored bar above the graph and is described in Section 8.4, Figure 8.7.

CO_2 Tracers

Figure 12.2 shows CO_2 tracer injection rate (orange curves. Primary y-axis) and production rate (secondary y-axis) as a function of days since injection for Rapid WAG (blue curve) and SAG (green curve). CO_2 tracers, GS1 (a), GS2 (b), and GS3 (c), were used to determine the mobility reduction of CO_2 by foam by comparing the Rapid WAG and SAG.

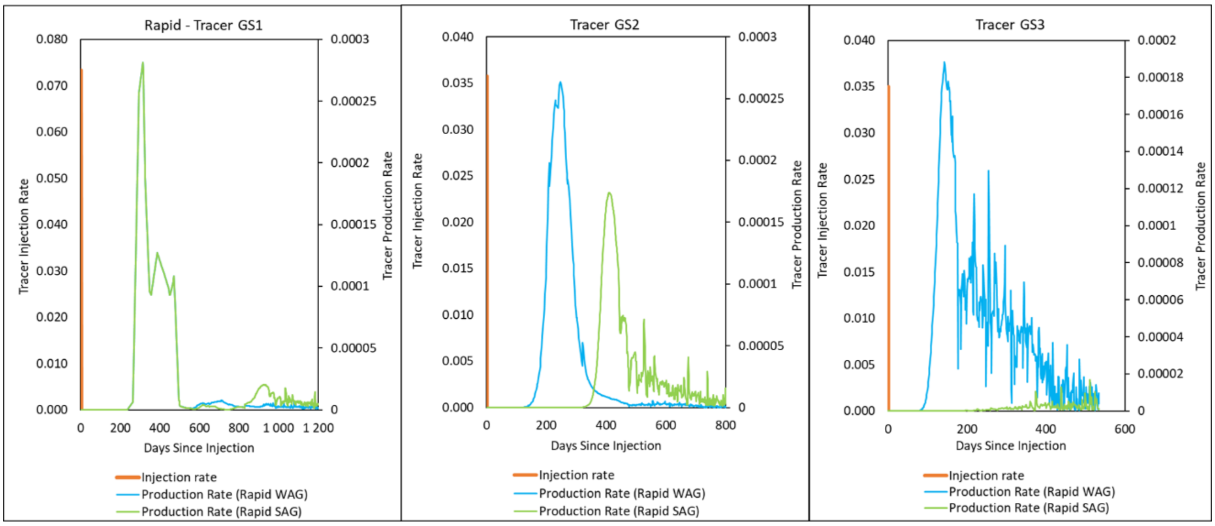

Figure 12.2 Injected CO_2 tracers; GS1 (a) before the pilot, GS2 (b) at the beginning of the pilot, and GS3 (c) after the pilot for Rapid WAG (blue curves) and SAG (green curves). Tracer injection rate (orange curves, primary y-axis) and tracer production rate (secondary y-axis) is plotted as a function of days since injection for each tracer.

In Figure 12.2a, GS1 was injected prior to the pilot, and only one tracer production line is visible because the injected fluid and injection schemes were identical for the WAG and SAG. The tracer broke through at a high rate after 235 days before decreasing close to zero after 50 days. The CO_2 tracer broke through at a high concentration and quickly dropped, indicating that the gas came from the same area. The gas likely swept a high permeable streak, resulting in a high production rate at breakthrough followed by a rapid decrease.

Figure 12.2b shows a new CO_2 tracer (GS2) was injected at the beginning of the pilot period, where WAG and SAG injections were initiated. Like GS1, the GS2 tracer for the Rapid WAG (blue curve) broke through at a high rate after 160 days before decreasing rapidly. In contrast, the GS2 tracer for the Rapid SAG broke through after 337 days at a lower rate and decreased gradually until 800 days after injection. The delay in tracer production of 180 days and the reduction in the breakthrough production rate of ca. 30% both indicated that foam significantly reduced gas mobility.

Furthermore, in Figure 12.2c, GS3 was injected after the pilot WAG, and SAG injections were completed. While the Rapid WAGs breakthrough was after 95 days at a high rate and gradually decreased to zero after 500 days, it did not increase until after 200 days for the Rapid SAG. The tracer production rate for the SAG was low for the entire injection period. The difference confirmed that the gas mobility reduction was significantly larger for the Rapid SAG than for the WAG. Furthermore, the effect of foam persisted until the end of injection, more than 300 days after the pilot program and surfactant injection was stopped.

Cumulative Oil and Water Production

Figure 12.3 shows cumulative oil (a) and water (b) production as a function of pore volume injected for the Rapid WAG (blue curves) and Rapid SAG (green curves). The pilot ranged from 0.17 to 0.25 PV, where the Rapid WAG and SAG injection schemes were performed. The WAG and SAG had the same injection scheme and cumulative production until the pilot was initiated. In Figure 12.3a, the cumulative oil production increased with a linear trend for the Rapid WAG, from 2000 STB at the beginning of the pilot (0.17 PV) to 2582 STB at the end of the simulation (0.35 PV). For the Rapid SAG, the cumulative oil production remained at 2000 STB during the pilot injection before increasing to 2830 by the end of the simulation. In Figure 12.3b, the water production was the same for both the Rapid WAG and SAG until the end of the pilot. After the pilot, the water production was slightly higher for the SAG than the WAG but subsided after 0.05 PV and was at the same cumulative water production of 11590 STB at the end of the simulation at 0.35 PV.

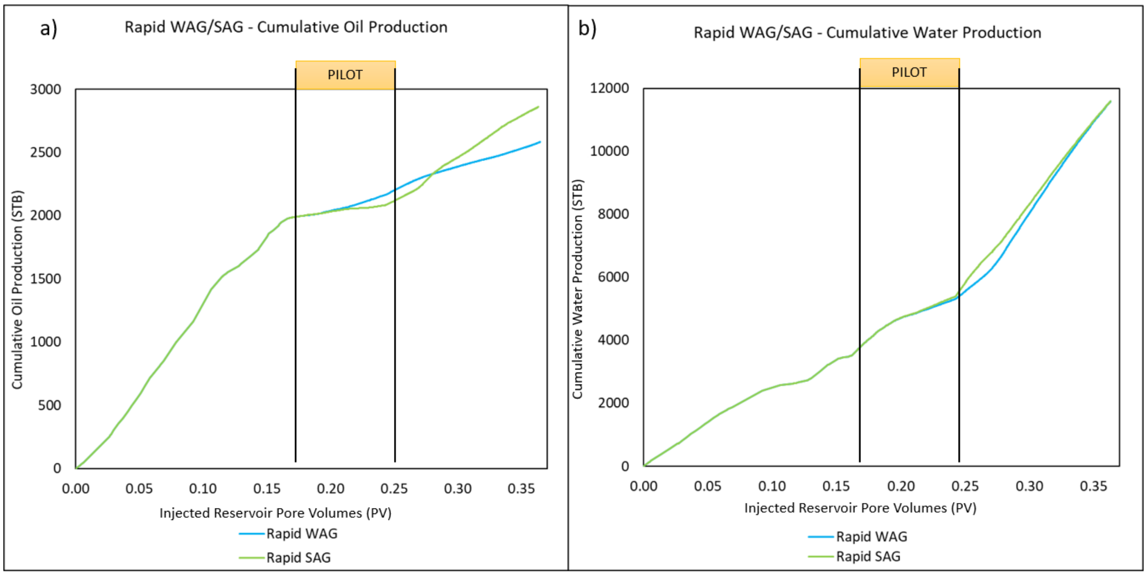

Figure 12.3 Cumulative oil (a) and water (b) production as a function of reservoir pore volumes injected for the Rapid WAG (blue curves) and SAG (green curves) injections. The Figure highlights the WAG and SAG period by "PILOT".

The presence of foam in the Rapid SAG delayed the oil production but increased the oil recovery. The 248 STB increase in oil recovery for the SAG compared to the WAG was after the pilot. Therefore, the foam had a prolonged effect in the reservoir, as seen for the CO_2 tracers in Figure 12.2. Because the water production was approximately the same for both the Rapid WAG and SAG, the foam in the Rapid SAG did not affect the total water production. The SAG's increase in oil recovery could be due to flow diversion into other parts of the reservoir, improving the volumetric sweep. If foam diverted CO_2 to other parts of the reservoir, CO_2 would be able to displace larger volumes of oil. The flow diversion and CO_2 mobility reduction from foam could have resulted in the buildup of an oil bank, mobilizing previously unwept or immobile oil. The oil production increased in the SAG while the water production was the same in the WAG. Therefore, the water cut must have been reduced, supporting increased production from other reservoir parts and mobilization of previously immobile oil.

CO_2 Retention

Figure 12.4 shows the fraction of CO_2 retained as a function of reservoir pore volumes injected for the Rapid WAG (blue curve) and Rapid SAG (green curve). The curves began with the pilot and continued to the simulation ended, and the injection scheme (Section 8.4) is highlighted by the top bar. The CO2 retention increased from 42% to 48% for the three first slugs for both the Rapid WAG and SAG. Next, the SAGs' CO_2 retention continued to increase to 56% at the pilot's end, while the CO2 retention for WAG began to decrease to 43% at the end of the pilot. Furthermore, the brine injection after the pilot program caused a decrease in CO_2 retention to 19% for the Rapid WAG and 34% for the Rapid SAG after the brine injection. The decrease in CO_2 retention after the pilot program was approximately the same for each case, but the Rapid SAG had 15 pp more CO_2 retention than the WAG. In summation, the presence of foam was favorable for increased CO_2 retention.

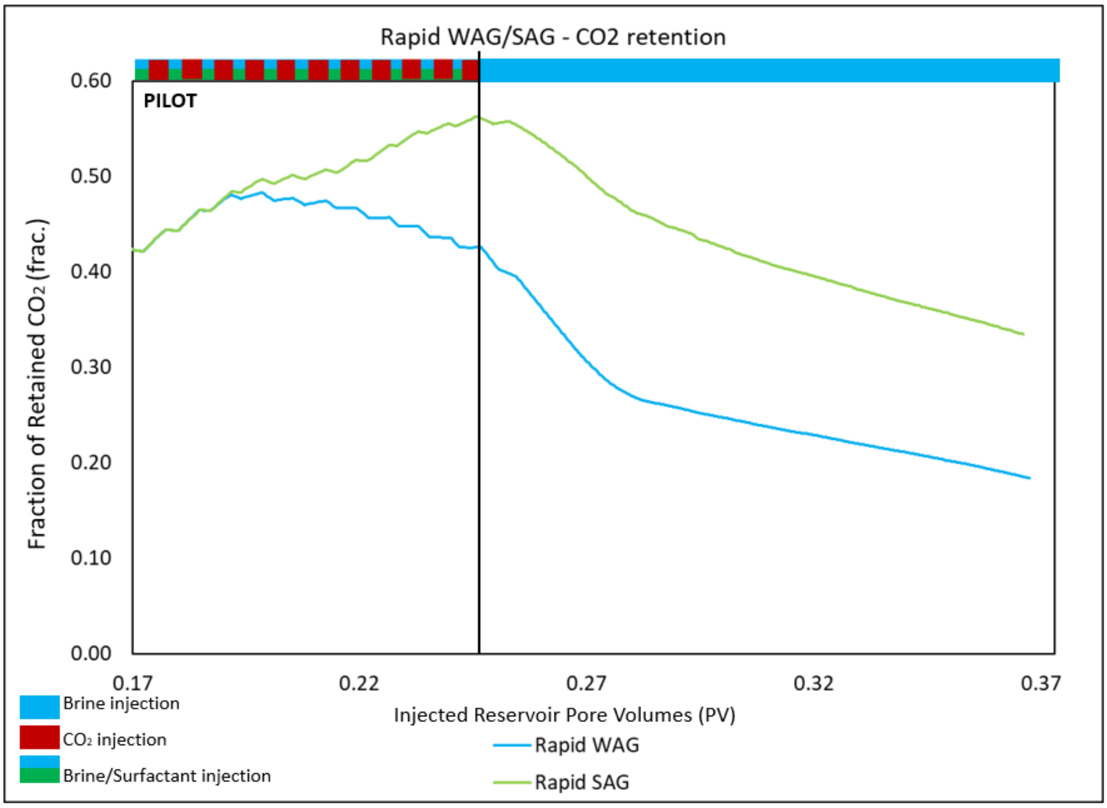

12.4 Fraction of CO_2 retention as a function of injected reservoir pore volumes for Rapid WAG (blue curve) and SAG (green curve). The colored bars at the top represent the injected fluid from the beginning of the pilot, where the lines separate different injection stages.

12.2 Single-Cycle WAG and SAG

The Single-Cycle WAG and SAG consisted of a large slug of brine or foaming solution (0.50 wt.% surfactant), followed by CO_2. The injection scheme was described in detail in Section 8.4.

Bottom Hole Pressure

Figure 12.5 shows the BHP (Primary y-axis) and injection rate (grey curve. Secondary y-axis) as a function of injected reservoir pore volumes for the Single-Cycle WAG (blue curve) and SAG (green curve). The injection scheme is represented by the colored bar at the top and is described in detail in Section 8.4. The curves' starting point was at the beginning of the pilot, with brine and foaming solution injection for WAG and SAG, respectively. Both increased from 2375 psi to 2720 psi during the liquid injection. The injection rate varied between 8 and 11 RB/day during the liquid slug and did not significantly impact the BHP. When the CO_2 injection was initiated, the BHP slightly decreased from 0.195 PV to 0.21 PV by 134 psi and 108 psi for the WAG and SAG, respectively. Furthermore, the BHP increased for both cases throughout the pilot to 3005 psi for the Single-Cycle WAG and 3185 psi for the Single-Cycle SAG. The increase of 180 psi in BHP for the SAG compared to the WAG confirmed that foam was generated.

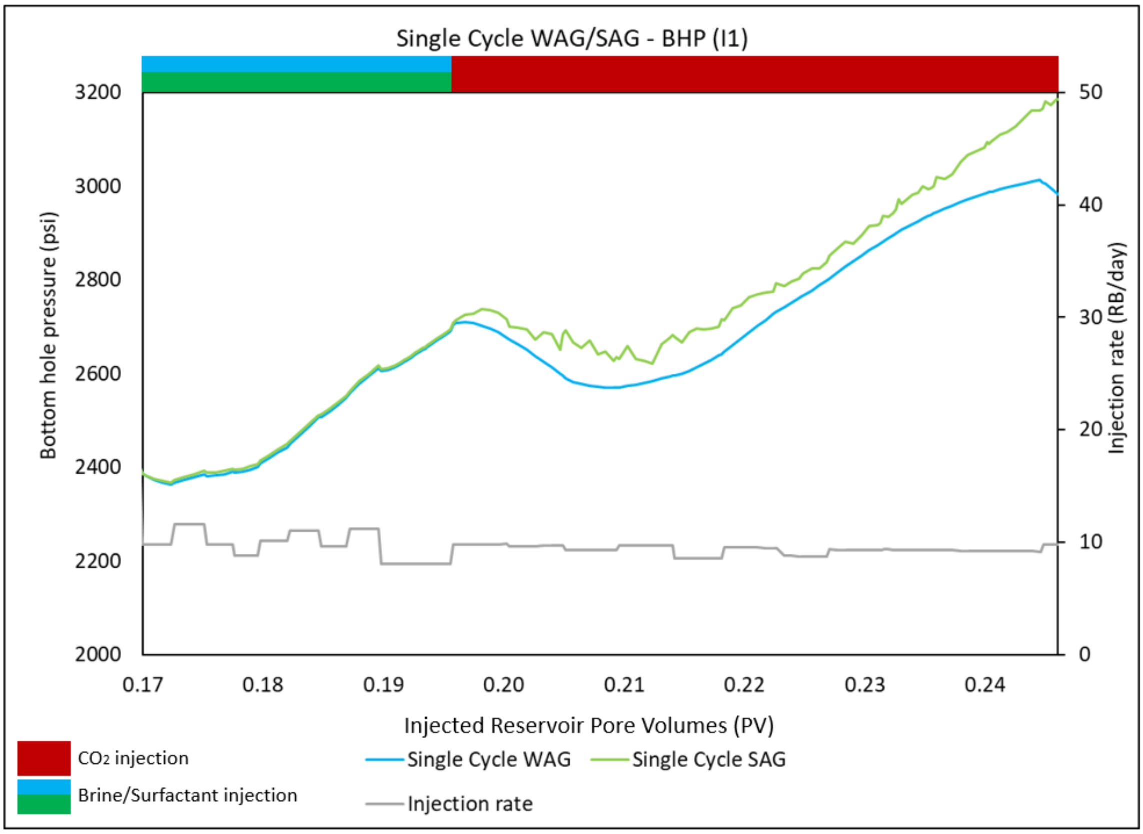

Figure 12.5 Bottom hole pressure (BHP) (blue and green curves, primary, y-axis) and injection rate (grey, curve secondary, y-axis) for the Single-Cycle WAG (blue curve) and SAG (green curve) during the pilot. The injection scheme is indicated by the colored bar above the graph and is described in Section 8.4, Figure 8.8

CO_2 Tracers

Figure 12.6 shows CO_2 tracer injection rate (orange curves, primary y-axis) and production rate (secondary y-axis) as a function of days since injection for Single-Cycle WAG (blue curve) and SAG (green curve). CO_2 tracers, GS1 (a), GS2 (b), and GS3 (c), were used to determine the mobility reduction of CO_2 by foam by comparing the Rapid WAG and SAG.

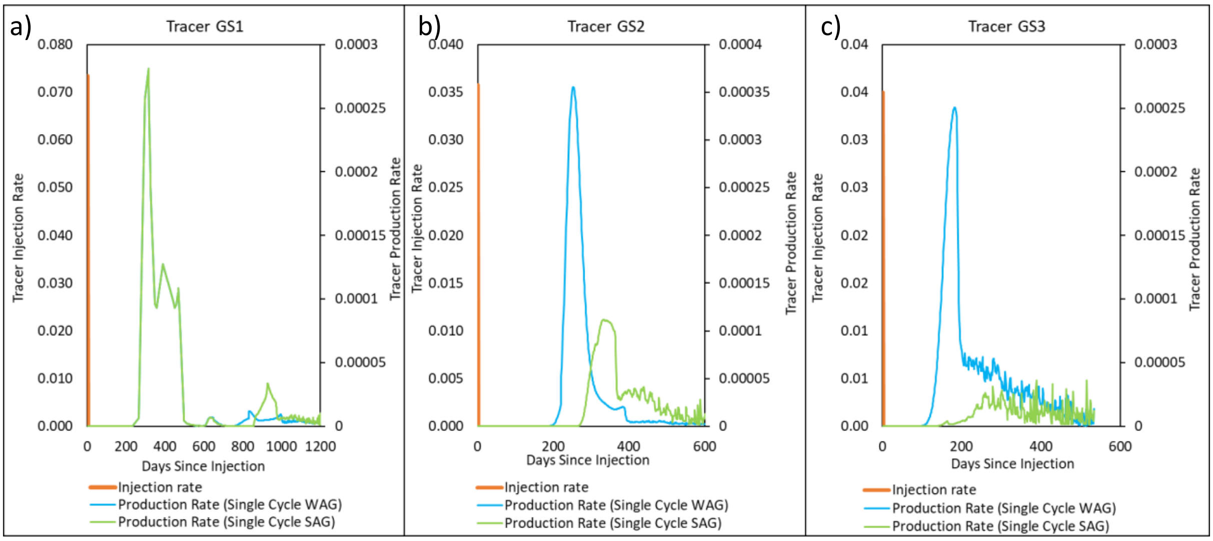

Figure 12.6 Injected CO_2 tracers; GS1 (a) before the pilot, GS2 (b) at the beginning of the pilot, and GS3 (c) after the pilot for Single-Cycle WAG (blue curves) and SAG (green curves). Tracer injection rate (orange curves, primary y-axis) and tracer production rate (secondary y-axis) is plotted as a function of days since injection for each tracer.

Figure 12.6a shows the pre-pilot tracer GS1 and proved that the Single-Cycle WAG and SAG had the same tracer production rate before the SAG implemented surfactant. The tracer broke through at a high production rate after 200 days and rapidly subsided, returning to a low concentration after 400 days since injection.

Next, Figure 12.6b showed GS2, which was injected at the beginning of the pilot. The Single-Cycle WAG had a similar tracer response as GS1, where the tracer injection rate increased rapidly after 193 days and quickly decreased and remained close to zero from 400 days since injection. Furthermore, the SAG had a tracer breakthrough of GS2 after 265 days at a much lower rate. The delay in breakthrough and reduction of the production rate in the Single-Cycle SAG, compared to the WAG, confirmed significant mobility reduction of CO_2 by foam.

Finally, GS3 was injected at the end of the pilot, as presented in Figure 12.6c. The Single-Cycle WAG had a tracer breakthrough after 119 days with a rapid increase and production rate. 207 days since injection, the tracer production rate subsided and remained below that until the end of the simulation. The tracer production rate in the Single-Cycle SAG increased after 168 days but remained low throughout. The difference in GS3s tracer production rate confirms that the foam generated in the Single-Cycle SAG resulted in a significant mobility reduction of CO_2.

Cumulative Oil and Water Production

Figure 12.7 shows cumulative oil (a) and water (b) production as a function of pore volumes injected for the Single-Cycle WAG (blue curves) and Single-Cycle SAG (green curves). The Single-Cycle injection scheme is highlighted by "PILOT." The injection schemes were identical before the pilot, and only one curve is visible for both 12.7a and 12.7b. During the pilot at 0.23 PV in Figure 12.7a, the oil production for WAG and SAG began to increase at different rates to an endpoint cumulative oil production of 2543 STB for the WAG and 2682 STB for the SAG. The foam generation in the Single-Cycle SAG increased oil recovery compared to the Single-Cycle WAG. Next, in Figure 12.7b, the water production remained the same for the Single-Cycle WAG and SAG until 0.24 PV, increasing more rapidly for the SAG. As a result, the cumulative endpoint production was 11243 for the WAG and 11576 for the SAG. The increased water production in the SAG indicated that the foam generation mobilized larger liquid volumes, likely due to increased viscosity as observed in the laboratory (Chapters 9 and 10).

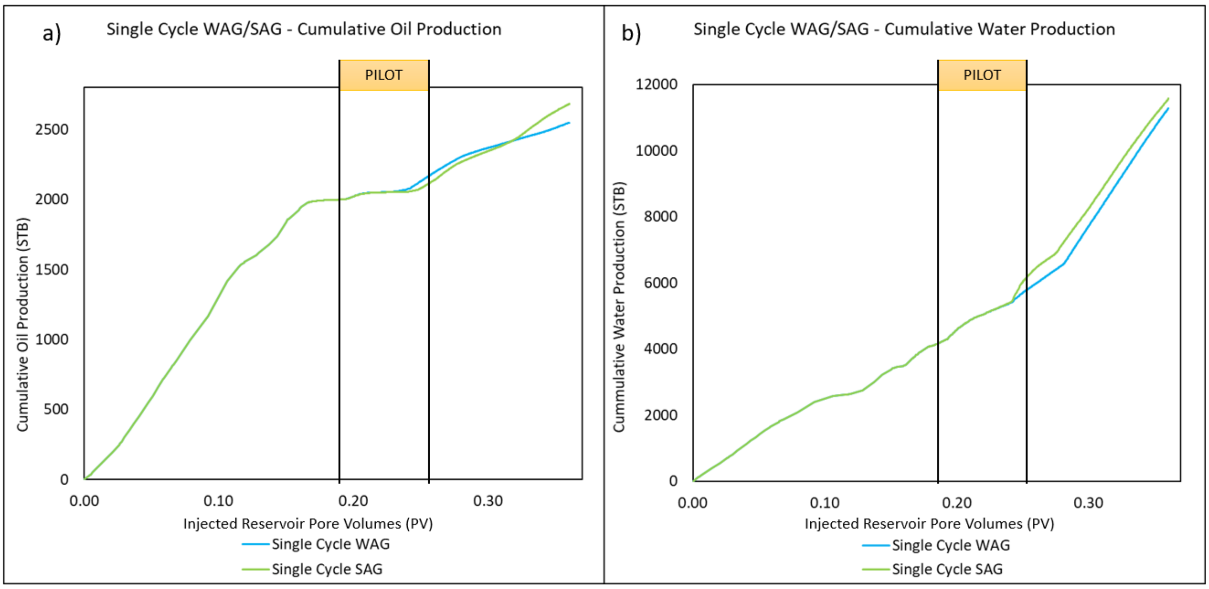

Figure 12.7 Cumulative oil (a) and water (b) production as a function of reservoir pore volumes injected for the Single-Cycle WAG (blue curves) and SAG (green curves) injections. The Figure highlights the WAG and SAG period by "PILOT".

CO_2 Retention

Figure 12.8 shows CO_2 retention as a function of injected reservoir pore volumes for the Single-Cycle WAG (blue curve) and Single-Cycle SAG (green curve). The injection scheme is indicated by the colored bars (Section 8.4) from the pilot to the end of the simulation. Firstly, during brine or surfactant injection, the CO_2 retention was stable at around 42% for both WAG and SAG. When CO_2 injection was initiated at 0.19 PV, the retention increased to 54% for the WAG and 58% for the SAG. The increased CO_2 retention during the CO_2 injection followed the same curve for both cases, indicating that the CO_2 did not reach the production well during the CO_2 injection. However, a slight difference of 4 pp in the CO_2 retention, indicating that the surfactant injected in the SAG affected the CO_2 retention. Next, the CO2 retention decreased for both the Single-Cycle WAG and SAG during the brine injection. While the WAG decreased to 21%, the SAG decreased to 32%. The difference in CO_2 retention at the end of the brine injection confirmed that the foam in the Single-Cycle SAG improved CO_2 retention even long after the surfactant was injected. The improvement in CO_2 retention was 11 pp compared to the Single-Cycle WAG.

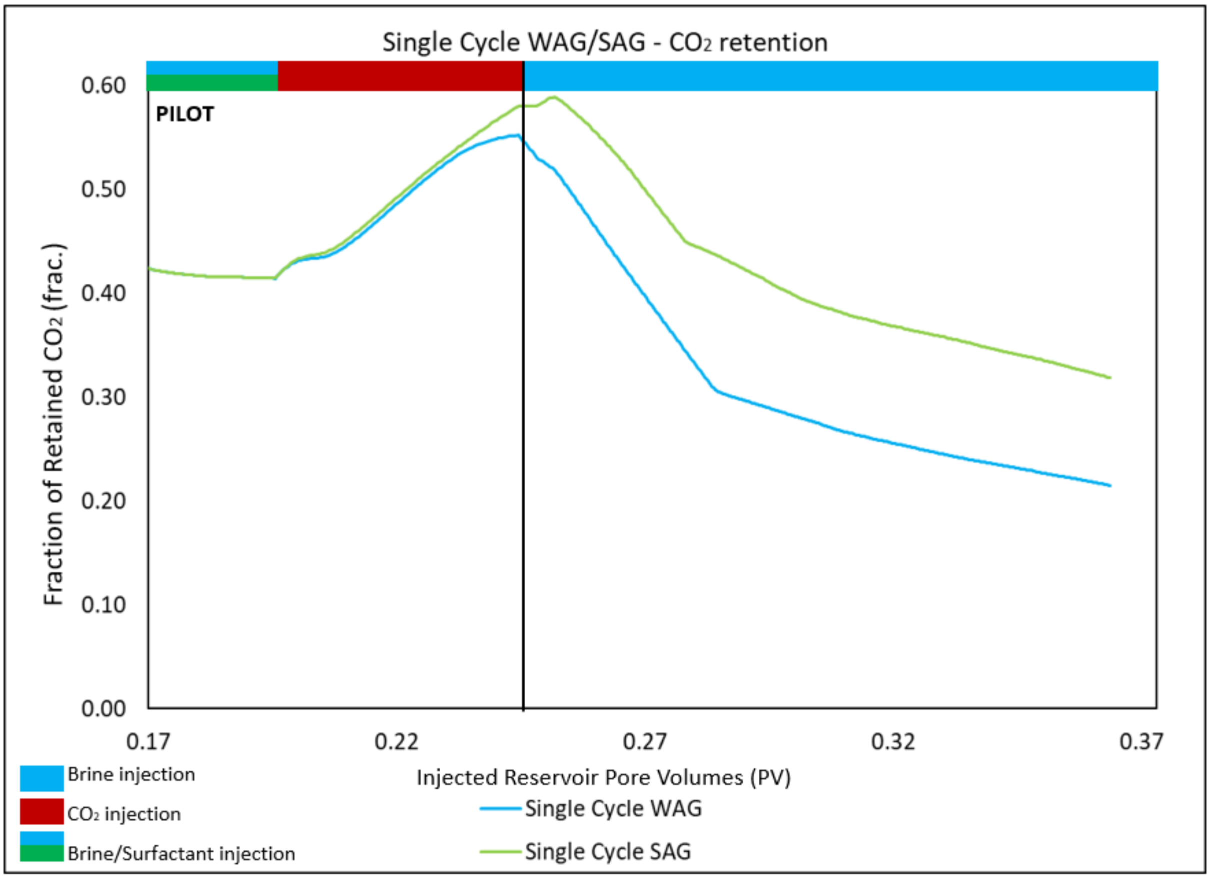

12.8 Fraction of CO_2 retention as a function of injected reservoir pore volumes for Single-Cycle WAG (blue curve) and SAG (green curve). The colored bars at the top begin at the pilot start and represent the injected fluid, where the lines separate different injection stages.

12.3 Co-Injection of Aqueous Phase and CO_2

The co-injections consisted of simultaneous injection of brine or foaming solution (0.50 wt.% surfactant) and CO_2 at a gas fraction of 0.60, followed by pure CO_2 injection. The injection scheme was described in detail in Section 8.4.

Bottom Hole Pressure

Figure 12.9 shows the BHP (primary y-axis) and injection rate (grey curve, secondary y-axis) as a function of injected reservoir pore volumes for the co-injection with brine (blue curve) and the co-injection with surfactant (green curve). The injection scheme is represented by the colored bar at the top and is described in detail in Section 8.4. When the pilot was initiated, the BHP increased for the co-injection with surfactant compared to the one with brine, confirming foam generation in the surfactant co-injection. Next, from 0.22 PV injected, CO_2 injection was initiated. The BHP for the surfactant co-injection continued to increase relative to the co-injection with brine, indicating that the foam still affected the reservoir even after pure CO_2 injection for 0.02 PV injected. The difference in BHP The injection rate varied between 10.28 RB/day and 11.84 RB/day and did not significantly affect the changes in BHP.

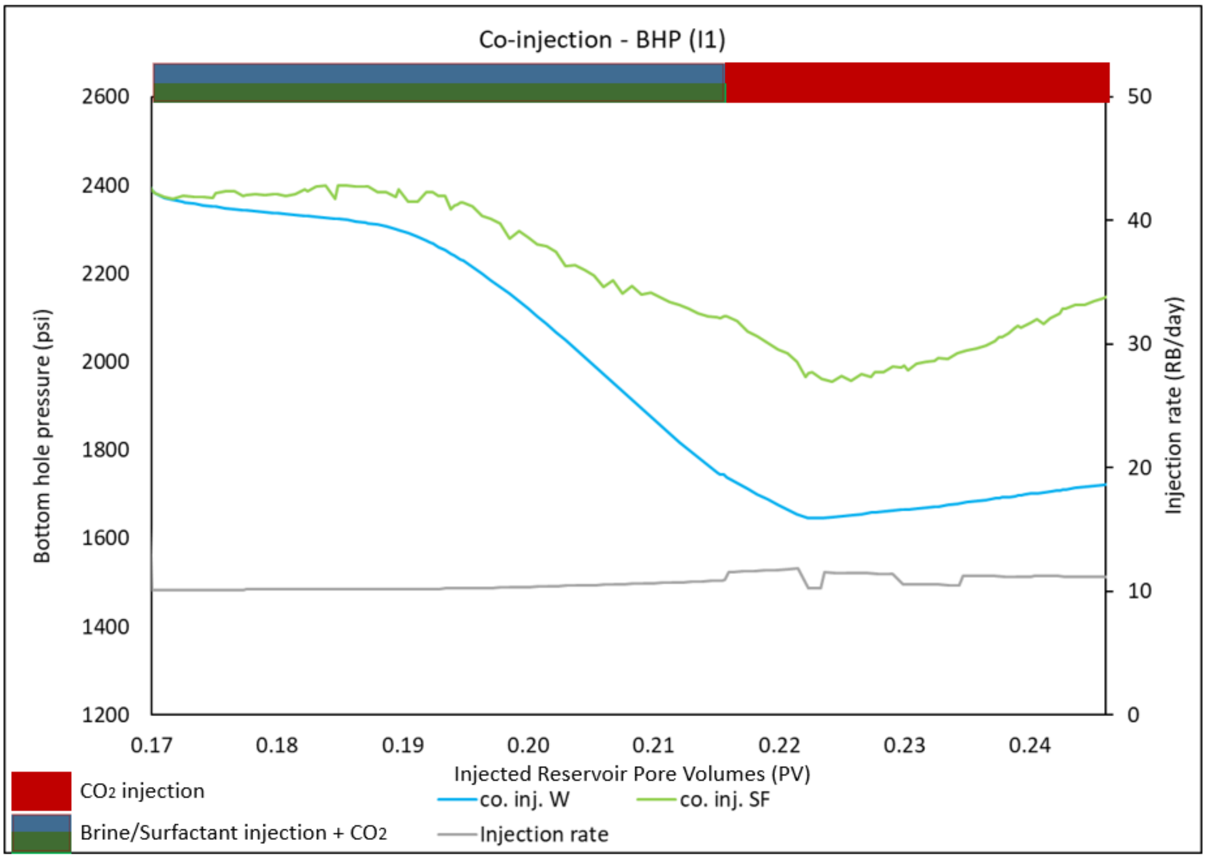

Figure 12.9 Bottom hole pressure (BHP) (blue and green curves, Primary, y-axis) and injection rate (grey, curve secondary, y-axis) for the co-injection of brine and CO_2 (blue curve) and foaming solution with 0.50 wt.% surfactant and CO_2 (green curve) during the pilot. The injection scheme is indicated by the colored bar above the graph and is described in Section 8.4, Figure 8.9.

CO$_2$ Tracers

Figure 12.10 shows CO$_2$ tracer injection rate (orange curves, primary y-axis) and production rate (secondary y-axis) as a function of days since tracer injection for co-injections with brine (blue curve) and surfactant (green curve). CO$_2$ tracers, GS1 (a), GS2 (b), and GS3 (c), were used to determine the mobility reduction of CO$_2$ by foam by comparing the co-injection with surfactant to the one without it.

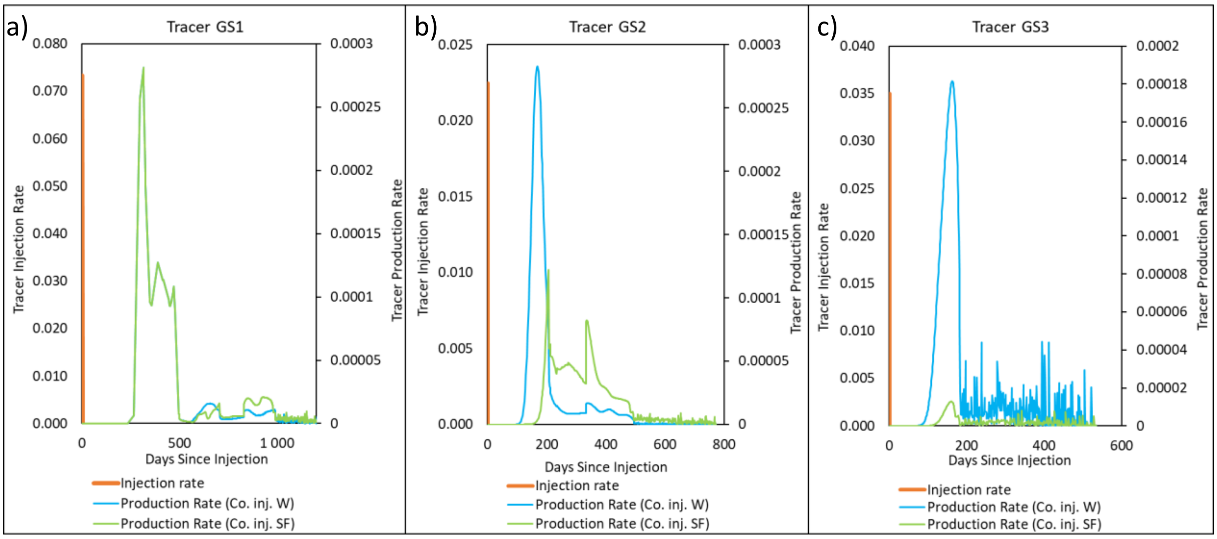

Figure 12.10 Injected CO$_2$ tracers; GS1 (a) before the pilot, GS2 (b) at the beginning of the pilot, and GS3 (c) after the pilot for co-injection of brine and CO$_2$ (blue curve) and foaming solution with 0.50 wt.% surfactant and CO$_2$ (green curve). Tracer injection rate (orange curves, primary y-axis) and tracer production rate (secondary y-axis) is plotted as a function of days since injection for each tracer.

The pre-pilot tracer, GS1, is presented in Figure 12.10a and indicated that the injected and produced tracer was the same prior to both co-injections. The first CO$_2$ tracer after surfactant injection, GS2, had breakthrough after 106 days for the co-injection with brine (Figure 12.10b, blue curve) and after 160 days for the co-injection surfactant (Figure 12.10b, green curve). In addition, the tracer broke through at a much higher concentration during the co-injection with brine compared to the co-injection with foaming solution. In the co-injection with foaming solution, the presence of foam delayed tracer breakthrough for 54 days and reduced the tracer production rate at breakthrough to 25% compared to co-injection with brine. Thus, foam reduced CO2 mobility more than co-injection with only brine. In addition, the production rate at breakthrough for the co-injection with surfactant indicated that CO$_2$ flow was diverted from the high-permeability streak to other parts of the reservoir. Figure 12.10c showed the CO$_2$ tracer GS3, injected at the end of the pilot. The tracer production rate for the co-injection with surfactant remained low after breakthrough 123 days after injection. However, the co-injection with brine had a high production rate after 81 days, similar to GS1 and GS2. The difference in CO$_2$ tracer production indicated that the foam had a long-term effect on the reservoir, reducing CO$_2$ mobility. The tracer production rate for the surfactant co-injection remained low and broke through after 123 days, whereas the brine co-injection had breakthrough after 81 days at a high rate.

Cumulative Oil and Water Production

Figure 12.11 shows cumulative oil (a) and water (b) production as a function of pore volume injected for the co-injections with brine (blue curves) and foaming solution (green curves). The pilot ranged from 0.17 to 0.25 PV, where the co-injection schemes were performed. In Figure 12.11a, the cumulative oil production was approximately the same for the two co-injections until 0.29 PV, where the oil production accelerated for the co-injection with surfactant. The oil production increased the final values of 2547 STB for the brine co-injection and 2810 STB for the surfactant co-Injection. The increased oil recovery with surfactant was likely a result of increased sweep efficiency due to foam. The delayed oil production could also indicate that an oil bank was generated by non-swept or immobile oil, contributing to increased oil recovery.

Next, in Figure 12.11b, the cumulative water production for the co-injections with brine and foaming solutions showed little difference in behavior. Directly after the pilot at 0.25 PV injected, the water production slightly increased for the co-injection with surfactant compared to the one with brine. However, at 0.31 PV, the two co-injections were identical and continued to increase to 11195 STB at the end of the simulation. The similarities in the cumulative water production indicated that the presence of foam did not increase the water production but did increase oil recovery.

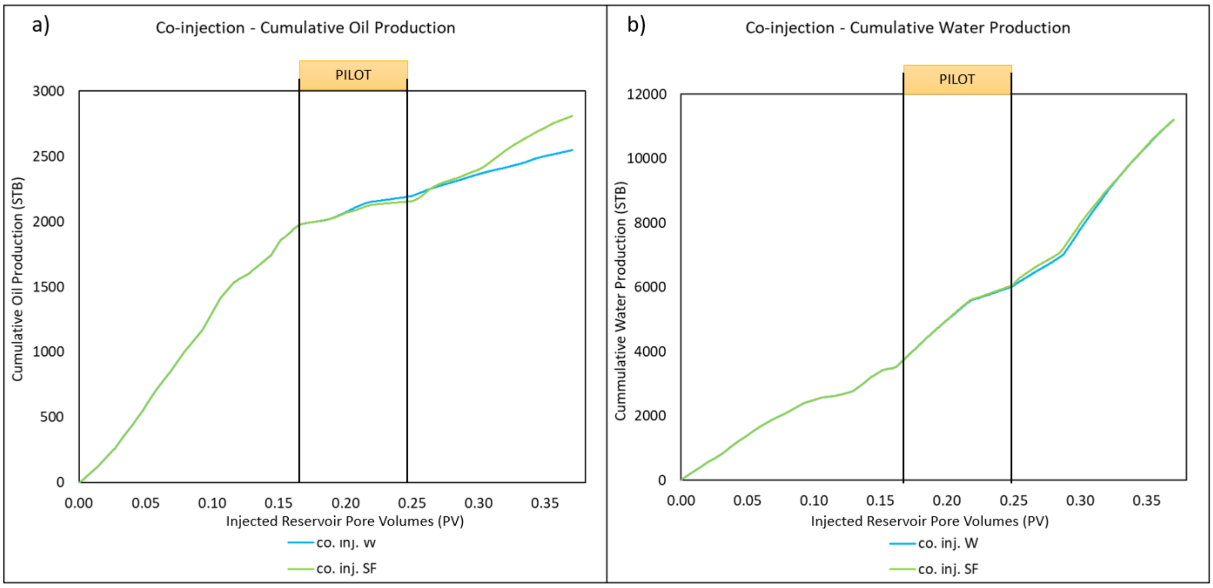

Figure 12.11 Cumulative oil (a) and water (b) production as a function of reservoir pore volumes injected for the co-injection of brine and CO_2 (blue curves) and foaming solution with 0.50 wt.% surfactant and CO_2 (green curves) injections. The Figure highlights the WAG and SAG period by “PILOT”.

CO_2 Retention

Figure 12.12 shows CO_2 retention as a function of injected reservoir pore volumes for the co-injection of brine and CO_2 (blue curve) and surfactant and CO_2 (green curve). The injection scheme is indicated by the colored bars at the top of Figure 12.12 and described in Section 8.4. First, during both co-injections, the CO_2 retention increased by 4% and 5% before decreasing to 35% and 45% for brine and surfactant, respectively. The foam generated during the co-injection with surfactant increased CO_2 retention compared to the one with brine. Next, during CO_2 injection (0.22 PV to 0.25PV injected), the CO_2 retention increased in both cases to 39% for brine and 51% for surfactant. Furthermore, when brine was injected (0.25 PV to 0.36 PV injected), the CO_2 retention decreased to 14% and 25% for the brine and surfactant co-injection, respectively. The difference between the cases confirmed that CO_2 retention was improved by 11 pp when foam was generated.

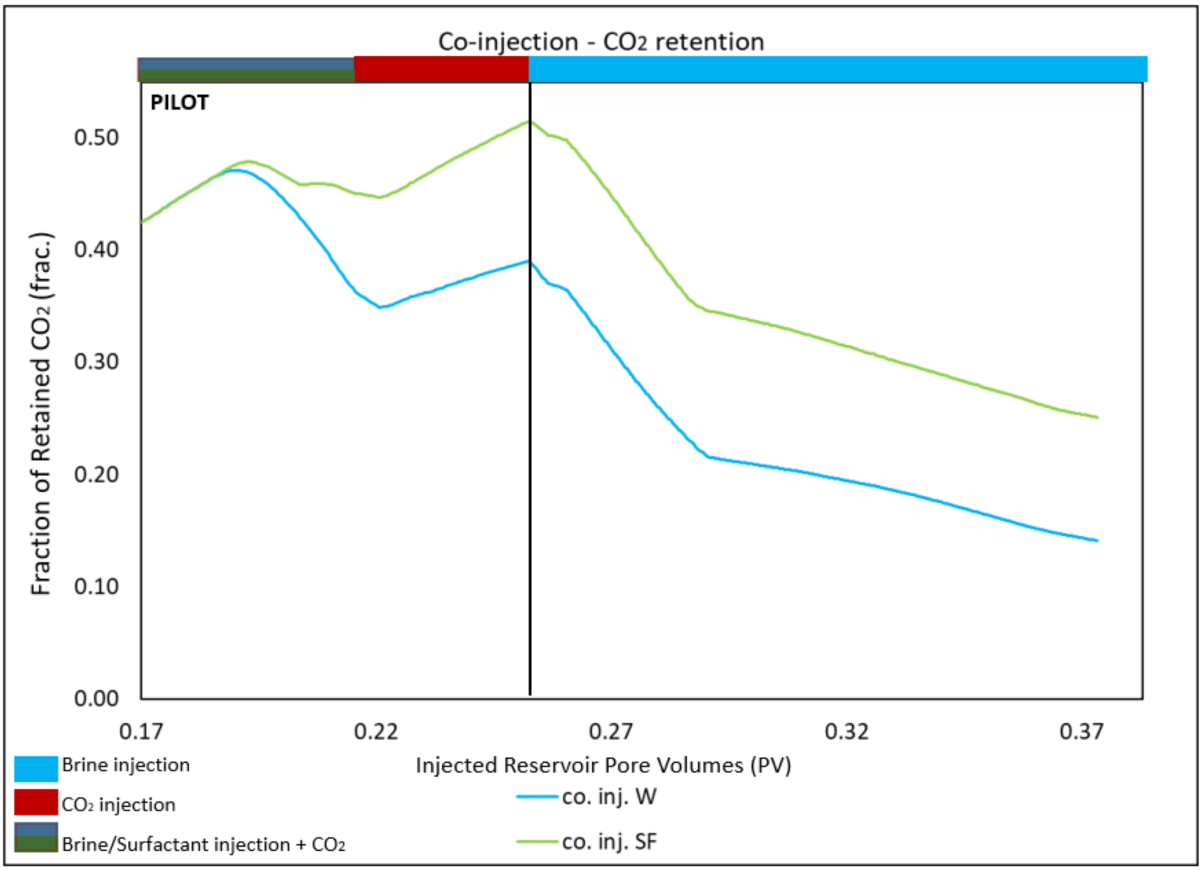

12.12 Fraction of CO_2 retention as a function of injected reservoir pore volumes for co-injection of brine and CO_2 (blue curve) and foaming solution with a 0.50 wt.% surfactant concentration and CO_2 (green curve). The colored bars at the top represent the injected fluid starting with the pilot, and the line separates different injection stages.

12.4 The Effect of Injection Strategy

Figure 12.13 shows two summarizing bar charts with (a) cumulative oil production and (b) CO_2 retention for the three injection strategies. The different injection strategies are presented both without and with surfactant as WAG and co-injection of brine and CO_2 (blue and purple bars), and SAG and co-injection of surfactant and CO_2 (green and brown bars). The corresponding WAGs and SAGs and the co-injections are identical, except for the surfactant implemented in the SAGs and surfactant co-injection.

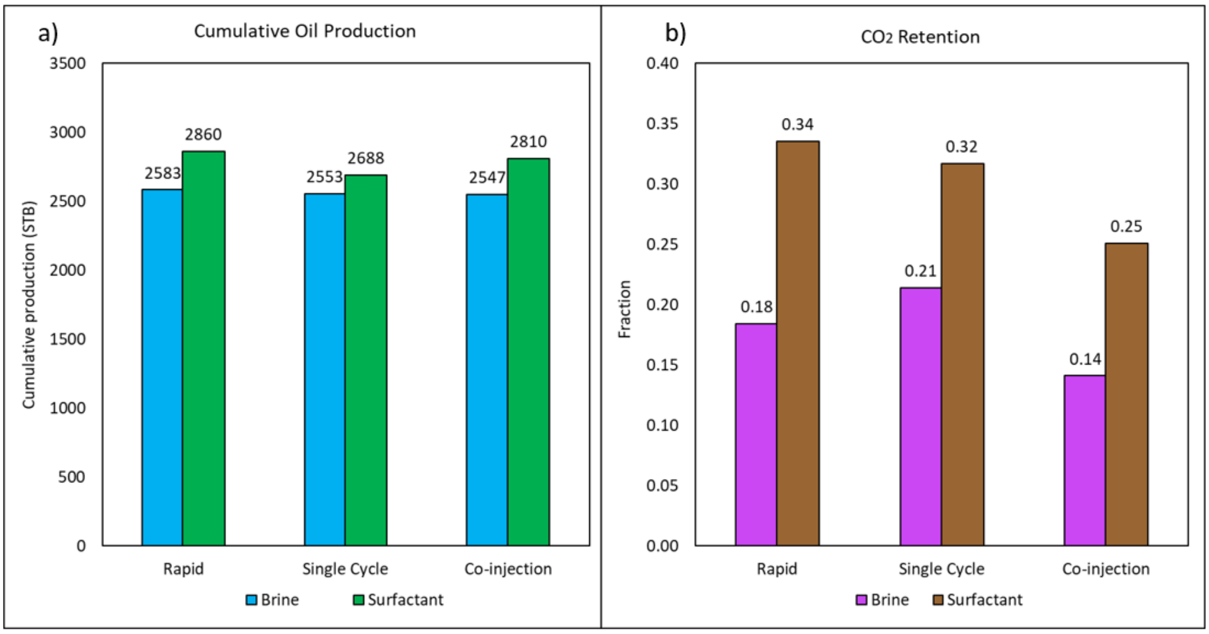

Figure 12.13 Bar chart summarizing the cumulative oil production (a) and CO_2 retention (b) divided into injection strategies. Cumulative oil production for WAG and co-injection with brine (blue bars) and SAG and co-injection with surfactant (green bars). CO_2 retention for WAG and co-injection with brine (purple bars) and SAG and co-injection with surfactant (brown bars).

First, in Figure 12.13a, the cumulative oil production is presented. All three injection strategies with surfactant increased cumulative oil production compared to brine. The BHP and delay in CO2 tracer breakthrough indicated that foam was generated in all three simulations with surfactant. The presence of foam likely diverted CO_2 flow to other reservoir regions, improving the sweep efficiency and increasing the oil recovery. The Rapid SAG had the highest cumulative oil production of 1860 STB, which was 50 STB and 172 STB more than the surfactant co-injection and Single-Cycle SAG.

In Figure 12.13b, the CO_2 retention is presented for each injection strategy. All three cases with surfactant had significantly larger CO_2 retention than the corresponding WAG/brine injections. The Rapid SAG had the highest CO_2 retention at 34%, the Single-Cycle SAG had 32%, and the co-injection with surfactant was the lowest at 25% CO_2 retention. The difference in CO_2 retention between the injection strategies proved that an alternating injection scheme was more efficient than co-injection in increasing CO_2 retention. Based on the BHP from the different cases, the co-injection had around 700 psi lower BHP than the SAGs, which could indicate that the foam was weaker and resulted in less CO_2 retention. A weaker foam would also result in weaker CO_2 mobility control, where less CO_2 is diverted from the high permeability streak. Based on cumulative oil production and CO_2 retention, the Rapid SAG was the most efficient injection strategy. The cumulative oil production was 2860 STB, and the CO_2 retention was 34%.

13 From Core to Field Scale – Observations and Reflections

Experimental work is often performed to investigate processes for implementation on a larger scale. In reservoir engineering, understanding the interaction between reservoir fluids and the system's dynamics is crucial. Accurate prediction of reservoir behavior is essential in developing models to optimize hydrocarbon production and CO_2 injection for storage.

Implementing EOR methods such as SAG injections are very expensive, and extensive testing on a smaller scale is therefore performed to minimize the risk of failure. In addition, before implementing a new EOR technique on the field scale, pilot tests can contribute to determining if a method is feasible on the field scale. Reservoir properties such as wettability are difficult to recreate accurately in the laboratory, and different mechanisms dominate the displacement processes. In core scale experiments, the dominating displacement mechanism is from viscous forces, but also diffusion and miscibility have a significant impact due to the small volumes. The core volume is small, which results in little effect from gravitational forces.

On the field scale, the volumes are enormous, and reservoir heterogeneity largely determines the direction of fluid flow. Injected fluids propagate over a large distance due to the large volumes. As observed in this thesis, a pore volume was injected at the core scale in minutes, whereas it took more than 100 days for CO_2 to break through, corresponding to less than 0.1 PV injected in the numerical simulations. Therefore, gravitational forces causing gravity segregations will significantly affect fluid displacement processes from density differences between reservoir fluids. The heterogeneity will also significantly impact the sweep efficiency, where the fluid flow will choose the flow path of least resistance, typically where permeability is high.

This thesis demonstrated several core-scale experiments, in addition to field-scale simulations, with CO_2 foam. Despite the differences in scale, rock properties, and displacement mechanisms, similar results were observed in both cases. Foam increased oil recovery and CO_2 retention compared to injections without foam. A rapid alternating injection scheme with surfactant proved to be the most efficient on both scales. Thus, confirming that core scale experiments can be a good indicator for field-scale behavior. However, understanding the differences in fluid interaction and flow behavior at different scales is crucial to upscaling laboratory experiments.

Part IV. Conclusions and Future Work

14 Conclusions

This thesis reported a combination of core-scale experimental work and field-scale numerical simulations investigating the use of CO_2 foam mobility control in CO_2 EOR and CO_2 storage. Optimal foam strengths and injection rates were identified in foam quality, and foam rate scans for different foaming solutions. In addition, oil recovery and CO_2 retention were studied at the core and field-scale for different CO_2 injection strategies, including rapidly alternating, single cycle, and co-injections with and without surfactant. Finally, in-situ imaging techniques were applied to understand the displacement process, with and without foam. Below are the key observations and conclusions from this experimental and numerical study:

- Foam Generation and Strength:
  The optimal gas fraction where the strongest foam was generated was between 0.50 and 0.70 for foaming solutions with 0.25 wt.% foaming solution with or without nanoparticles. The highest foam strength during steady-state co-injection was obtained at a 2 ft/day injection rate with a surfactant concentration of 0.25 wt.% Surfonic L24-22. Foaming solutions with surfactant and nanoparticles did not increase foam stability compared to foaming solutions with only surfactant. Increased injection rate caused a decrease in foam stability, indicating shear-thinning behavior.

- Core Scale: Oil Recovery and CO_2 Retention:
  The Rapid SAG with a 0.50 wt.% surfactant concentration increased oil recovery and CO_2 retention compared to the Single-Cycle SAGs and Rapid SAG with 0.25 wt.% surfactant concentration. All experiments performed with surfactant had larger oil recovery and CO_2 retention than those without surfactant. Stronger foam increased CO_2 retention, whereas oil recovery was not as dependent on foam strength. The Single-Cycle and Rapid SAGs with identical foaming solutions and similar foam strength demonstrated similar performance in oil recovery and CO_2 retention, independent of injection strategy.

- In-situ Imaging of Foam flow with PET/CT:
  The in-situ mobility reduction of CO_2 by foam was imaged with PET/CT. The Single-Cycle SAG improved fluid displacement significantly compared to the Single-Cycle WAG. Front development was unstable for pure CO_2 injection. The presence of foam provided a piston-shaped displacement front and improved liquid displacement on the core scale.

- Field Scale: Oil Recovery and CO_2 Retention:
  The Rapid SAG produced the most oil and retained the most CO_2 compared to the Single-Cycle SAG and co-injection with surfactant. All injection schemes with surfactant improved oil recovery and CO_2 retention compared to injection schemes without surfactant. Alternating injection with surfactant (SAG) generated a stronger foam which increased CO_2 retention compared to co-injection with surfactant.

The key observations and conclusions from this thesis demonstrated improved oil recovery and CO_2 retention using CO_2 foam mobility control. A rapid alternating injection scheme proved to be most effective both in core-scale laboratory experiments and in field-scale numerical simulations.

15 Future Work

The experimental and numerical work presented in this thesis was part of an ongoing project by NFR, “Optimizing CO_2 Foam Mobility Control for Field Pilots” led by the Reservoir Physics group at the Department of Physics and Technology, University of Bergen. The work conducted for this thesis has contributed to improve the understanding of CO_2 foam in regards to foam strength and propagation, in addition to oil recovery and CO_2 retention. Suggestions for future work to build upon these results are provided in the following list:

- Perform foam quality and rate scans with different concentrations of surfactant and with different rock types.

- Perform CO_2 EOR and CO_2 retention experiments with crude oil to investigate oil recovery and CO_2 storage under more field-like conditions.

- Repeat the in-situ imaging experiments on different rock types to further investigate the possibilities of visualizing foam propagation in whole cores.

- In-depth analysis of the PET/CT images should be performed to quantify the front development of CO_2 with and without foam.

- Conduct numerical simulations with different gas fractions for both the Rapid and Single-Cycle SAG injection schemes to investigate the effect on oil recovery and CO_2 retention.

- Change the foam parameters to investigate changes on foam generation and propagation under different conditions.

- Conduct numerical simulations with sandstone properties to better correlate to the experimental work.

Part V. Nomenclature, Abbreviations, References and Appendix

Nomenclature

K_a	Absolute permeability
k_{eff}	Effective permeability
k_r	Relative permeability
P_C	Capillary pressure
σ	Interfacial tension
V_{CO_2}	Volume of CO_2
f_{gas}	Gas fraction
Q	Total flow rate
q	Component flow rate
μ_{APPV}	Apparent viscosity
ΔP	Pressure gradient
L	Length
μ	Viscosity
I	Intensity
ϕ	Porosity
ρ	Density
M	Mass-flux
β	Volume factor
T	Temperature
P	Pressure
pp	Percentage points
S_w	Water saturation
S_g	Gas saturation
S_{wi}	Irreducible water saturation
Wt.%	Weight percent
EPCAP	Shear thinning flow behavior
EPDRY	Foam collapse
EPOIL	Effect of oil saturation
EPSURF	Effect of surfactant concentration
FMCAP	Minimum capillary pressure
FMMOB	Reduction in gas mobility by foam
FMSURF	Surfactant concentration
FMOIL	Oil saturation where foam collapse
cP	Centipoise
psi	Pound-force per square inch
STB	Stock tank barrel

Abbreviations

EOR	Enhanced oil recovery
CCS	Carbon capture and storage
CCUS	Carbon capture, utilization, and storage
GHG	Greenhouse gas
Surfactant	Surface active agent
CO_2	Carbon dioxide
OOIP	Original oil in place
WAG	Water alternating gas
SAG	Surfactant alternation gas
CT	Computed Tomography
PET	Positron Emission Tomography
FDG	Fluorodeoxyglucose
LOR	Line of response
E100	ECLIPSE 100
E300	ECLIPSE 300
SF	Surfactant
NP	Nanoparticles
IPA	Isopropanol
PV	Pore volume
PVT	Pressure-Volume-Temperature
CMC	Critical micellar concentration
RB	Reservoir barrels
VOI	Volume of interest
ROI	Region of interest
BHP	Bottom hole pressure

References

Akin, S., & Kovscek, A. (2003). Computed tomography in petroleum engineering research. *Geological Society, London, Special Publications*, *215*(1), 23-38.

Al Adasani, A., & Bai, B. (2011). Analysis of EOR projects and updated screening criteria. *Journal of Petroleum Science and Engineering*, *79*(1-2), 10-24.

Alcorn, Z. P., Fernø, M., & Graue, A. (2016). Workflow for Optimal Injection of CO2 to Enhance Oil Recovery in Mature Oil Fields: A Preliminary Study for a Field Pilot Program. SPE Bergen One Day Seminar,

Alcorn, Z. P., Fredriksen, S., Sharma, M., Føyen, T. L., Wergeland, C., Fernø, M., Graue, A., & Ersland, G. (2020). Core-scale sensitivity study of CO2 foam injection strategies for mobility control, enhanced oil recovery, and CO2 storage.

Alcorn, Z. P., Fredriksen, S. B., Sharma, M., Rognmo, A. U., Føyen, T. L., Fernø, M. A., & Graue, A. (2019). An Integrated Carbon-Dioxide-Foam Enhanced-Oil-Recovery Pilot Program With Combined Carbon Capture, Utilization, and Storage in an Onshore Texas Heterogeneous Carbonate Field. *SPE Reservoir Evaluation & Engineering*, *22*(04), 1449-1466. https://doi.org/10.2118/190204-pa

Alcorn, Z. P., Føyen, T., Gauteplass, J., Benali, B., Soyke, A., & Fernø, M. (2020a). Pore- and Core-Scale Insights of Nanoparticle-Stabilized Foam for CO2-Enhanced Oil Recovery. *Nanomaterials*, *10*(10), 1917. https://www.mdpi.com/2079-4991/10/10/1917

Alcorn, Z. P., Føyen, T., Gauteplass, J., Benali, B., Soyke, A., & Fernø, M. (2020b). Pore-and core-scale insights of nanoparticle-stabilized foam for CO2-enhanced oil recovery. *Nanomaterials*, *10*(10), 1917.

Alcorn, Z. P., Føyen, T., Zhang, L., Karakas, M., Biswal, S. L., Hirasaki, G., & Graue, A. (2020). CO2 Foam Field Pilot Design and Initial Results. SPE Improved Oil Recovery Conference,

Alvarado, V., & Manrique, E. (2010). Enhanced oil recovery: an update review. *Energies*, *3*(9), 1529-1575.

Anderson, W. G. (1986). Wettability literature survey-part 1: rock/oil/brine interactions and the effects of core handling on wettability. *Journal of Petroleum Technology*, *38*(10), 1125-1144.

Anderson, W. G. (1987). Wettability literature survey-part 4: Effects of wettability on capillary pressure. *Journal of Petroleum Technology*, *39*(10), 1283-1300.

Anderson, W. G. (1987). Wettability Literature Survey Part 5: The Effects of Wettability on Relative Permeability. *Journal of Petroleum Technology*, *39*(11), 1453-1468. https://doi.org/10.2118/16323-pa

Asghari, K., & Torabi, F. (2008). Effect of miscible and immiscible CO2 injection on gravity drainage: experimental and simulation results. SPE Symposium on Improved Oil Recovery,

Ayirala, S. C., Xu, W., & Rao, D. N. (2006). Interfacial behaviour of complex hydrocarbon fluids at elevated pressures and temperatures. *The Canadian Journal of Chemical Engineering*, *84*(1), 22-32.

Azzolina, N. A., Nakles, D. V., Gorecki, C. D., Peck, W. D., Ayash, S. C., Melzer, L. S., & Chatterjee, S. (2015). CO2 storage associated with CO2 enhanced oil recovery: A statistical analysis of historical operations. *International Journal of Greenhouse Gas Control*, *37*, 384-397.

Bikerman, J. J. (2013). *Foams* (Vol. 10). Springer Science & Business Media.

Boeije, C., & Rossen, W. (2013). Fitting foam simulation model parameters to data. IOR 2013-17th European Symposium on Improved Oil Recovery,

Bouckaert, S., Pales, A. F., McGlade, C., Remme, U., Wanner, B., Varro, L., D'Ambrosio, D., & Spencer, T. (2021). Net Zero by 2050: A Roadmap for the Global Energy Sector.

Brattekås, B., Fernø, M. A., Haugen, M., Føyen, T., Steinsbø, M., Graue, A., Brekke, N., Adamsen, T. C. H., Rygh, C. B., & Espedal, H. (2021). Of rats and rocks: using pre-clinical PET imaging facilities in core analysis.

Brattekås, B., Steinsbø, M., Graue, A., Fernø, M., Espedal, H., & Seright, R. S. (2016). New insight to wormhole formation in polymer gel during water chasefloods using positron emission tomography PET. SPE Bergen One Day Seminar,

Brock, W. R., & Bryan, L. A. (1989). Summary Results of CO2 EOR Field Tests, 1972-1987. Low Permeability Reservoirs Symposium,

Chambers, D. J. (1994). Foams for well stimulation. In. ACS Publications.

Cheng, Y.-c., Di, Q.-f., Gu, C.-y., Ye, F., Hua, S., & Yang, P.-q. (2015). Visualization study on fluid distribution and end effects in core flow experiments with low-field mri method. *Journal of hydrodynamics*, *27*(2), 187-194.

ECLIPSE. (2016). Simulation Software Reference Manual. In Schlumberger (Ed.). Houstion, TX, USA: Schlumberger.

Eiken, O., Ringrose, P., Hermanrud, C., Nazarian, B., Torp, T. A., & Høier, L. (2011). Lessons learned from 14 years of CCS operations: Sleipner, In Salah and Snøhvit. *Energy procedia*, *4*, 5541-5548.

El-Dessouky, H. T., & Ettouney, H. M. (2002). *Fundamentals of salt water desalination*. Elsevier.

Energy.gov. (2022). *Enhanced Oil Recovery*. https://www.energy.gov/fecm/science-innovation/oil-gas-research/enhanced-oil-recovery

Enick, R. M., Olsen, D., Ammer, J., & Schuller, W. (2012). Mobility and Conformance Control for CO2 EOR via Thickeners, Foams, and Gels - A Literature Review of 40 Years of Research and Pilot Tests. SPE Improved Oil Recovery Symposium,

Equinor. (2022). *Northern Lights CCS*. Equinor ASA. https://www.equinor.com/en/what-we-do/northern-lights.html

Espinosa, D., Caldelas, F., Johnston, K., Bryant, S. L., & Huh, C. (2010). Nanoparticle-Stabilized Supercritical CO2 Foams for Potential Mobility Control Applications. SPE Improved Oil Recovery Symposium,

Falls, A. H., Musters, J. J., & Ratulowski, J. (1989). The Apparent Viscosity of Foams in Homogeneous Bead Packs. *SPE reservoir engineering*, *4*(02), 155-164. https://doi.org/10.2118/16048-pa

Farajzadeh, R., Andrianov, A., Krastev, R., Hirasaki, G. J., & Rossen, W. R. (2012). Foam-Oil Interaction in Porous Media: Implications for Foam Assisted Enhanced Oil Recovery. SPE EOR Conference at Oil and Gas West Asia,

Freund, P., Bachu, S., Simbeck, D., Thambimuthu, K., & Gupta, M. (2005). Properties of CO2 and carbon-based fuels. *IPCC Special Report on*.

Friedmann, F., & Jensen, J. (1986). Some parameters influencing the formation and propagation of foams in porous media. SPE California Regional Meeting,

Green, D. W., & Willhite, G. P. (1998). *Enhanced oil recovery* (Vol. 6). Henry L. Doherty Memorial Fund of AIME, Society of Petroleum Engineers ….

Grogan, A. T., & Pinczewski, W. V. (1987). The Role of Molecular Diffusion Processes in Tertiary CO2 Flooding. *Journal of Petroleum Technology*, *39*(05), 591-602. https://doi.org/10.2118/12706-pa

Heleen van Soest, D. M., Christoph Bertram, Mathijs Harmsen. (2018). *Opportunities for Enhanced Action to*

Keep Paris Goals in Reach. https://unfccc.int/sites/default/files/resource/437_Enhanced%20Action%20to%20Keep%20Paris%20Goals%20in%20Reach.pdf

Hirasaki, G. J., & Lawson, J. B. (1985). Mechanisms of Foam Flow in Porous Media: Apparent Viscosity in Smooth Capillaries. *Society of Petroleum Engineers Journal*, *25*(02), 176-190. https://doi.org/10.2118/12129-pa

Holm, L. (1986). Miscibility and miscible displacement. *Journal of Petroleum Technology*, *38*(08), 817-818.

Hove, A., Ringen, J., & Read, P. (1987). Visualization of laboratory corefloods with the aid of computerized tomography of X-rays. *SPE reservoir engineering*, *2*(02), 148-154.

Huber, M. L., & Perkins, R. A. (2005). Thermal conductivity correlations for minor constituent fluids in natural gas: n-octane, n-nonane and n-decane. *Fluid Phase Equilibria*, *227*(1), 47-55.

Jian, G., Puerto, M. C., Wehowsky, A., Dong, P., Johnston, K. P., Hirasaki, G. J., & Biswal, S. L. (2016). Static adsorption of an ethoxylated nonionic surfactant on carbonate minerals. *Langmuir*, *32*(40), 10244-10252.

Khatib, Z. I., Hirasaki, G. J., & Falls, A. H. (1988). Effects of Capillary Pressure on Coalescence and Phase Mobilities in Foams Flowing Through Porous Media. *SPE reservoir engineering*, *3*(03), 919-926. https://doi.org/10.2118/15442-pa

Kovscek, A. R., & Radke, C. J. (1993). *Fundamentals of foam transport in porous media*.

Kular, G. S., Lowe, K., & Coombe, D. (1989). Foam Application in an Oil Sands Steamflood Process. SPE Annual Technical Conference and Exhibition,

Lake, L. W., Johns, R., Rossen, B., & Pope, G. A. (2014). *Fundamentals of enhanced oil recovery* (Vol. 1). Society of Petroleum Engineers Richardson, TX.

Lee, S., & Kam, S. (2013). Enhanced oil recovery by using CO2 foams: fundamentals and field applications. In *Enhanced Oil Recovery Field Case Studies* (pp. 23-61). Elsevier.

Lemmon, E. W. (2022). Thermophysical properties of fluid systems. *NIST chemistry WebBook*.

Mangalsingh, D., & Jagai, T. (1996). A laboratory investigation of the carbon dioxide immiscible process. SPE Latin America/Caribbean Petroleum Engineering Conference,

McAuliffe, C. D. (1973). Oil-in-Water Emulsions and Their Flow Properties in Porous Media. *Journal of Petroleum Technology*, *25*(06), 727-733. https://doi.org/10.2118/4369-pa

Melzer, L. S. (2012). Carbon dioxide enhanced oil recovery (CO2 EOR): Factors involved in adding carbon capture, utilization and storage (CCUS) to enhanced oil recovery. *Center for Climate and Energy Solutions*, 1-17.

Metz, B., Davidson, O., De Coninck, H., Loos, M., & Meyer, L. (2005). *IPCC special report on carbon dioxide capture and storage*. Cambridge: Cambridge University Press.

Muller, T., & Lake, L. W. (1991). Theoretical study of water blocking in miscible flooding. *SPE reservoir engineering*, *6*(04), 445-451.

Mungan, N. (1981). Carbon Dioxide Flooding-fundamentals. *Journal of Canadian Petroleum Technology*, *20*(01). https://doi.org/10.2118/81-01-03

Nagarajan, N., & Robinson Jr, R. L. (1986). Equilibrium phase compositions, phase densities, and interfacial tensions for carbon dioxide+ hydrocarbon systems. 2. Carbon dioxide+ n-decane. *Journal of Chemical and Engineering Data*, *31*(2), 168-171.

Osterloh, W. T., & Jante, M. J., Jr. (1992). Effects of Gas and Liquid Velocity on Steady-State Foam Flow at High Temperature. SPE/DOE Enhanced Oil Recovery Symposium,

Peksa, A. E., Wolf, K.-H. A., & Zitha, P. L. (2015). Bentheimer sandstone revisited for experimental purposes. *Marine and Petroleum Geology*, *67*, 701-719.

Perkins, T. K., & Johnston, O. C. (1963). A Review of Diffusion and Dispersion in Porous Media. *Society of Petroleum Engineers Journal*, *3*(01), 70-84. https://doi.org/10.2118/480-pa

Ransohoff, T., & Radke, C. (1988). Laminar flow of a wetting liquid along the corners of a predominantly gas-occupied noncircular pore. *Journal of colloid and interface science*, *121*(2), 392-401.

Rao, D. N., Girard, M., & Sayegh, S. G. (1992). The Influence Of Reservoir Wettability On Waterflood And Miscible Flood Performance. *Journal of Canadian Petroleum Technology*, *31*(06). https://doi.org/10.2118/92-06-05

Rognmo, A. U., Fredriksen, S. B., Alcorn, Z. P., Sharma, M., Føyen, T., Eide, Ø., Graue, A., & Fernø, M. (2019). Pore-to-Core EOR Upscaling for CO2 Foam for CCUS. *SPE Journal*, *24*(06), 2793-2803.

Romero-Zerón, L. (2012). *Introduction to enhanced oil recovery (EOR) processes and bioremediation of oil-contaminated sites*. BoD–Books on Demand.

Rossen, W. (2013). Numerical challenges in foam simulation: a review. SPE annual technical conference and exhibition,

Rossen, W. R. (1996). Foams in enhanced oil recovery. *Foams: theory, measurements and applications*, *57*, 413-464.

Schlumberger. (2014). Blackoil Reservoir Simulation

Training and Exercise Guide

In: Schlumberger.
Schlumberger, A. (2016). Eclipse technical description. *Schlumberger Information Solutions*.
Schmitz, R. E., Alessio, A. M., & Kinahan, P. (2013). The Physics of PET / CT scanners.
Schramm, L. L. (1994). *Foams: fundamentals and applications in the petroleum industry*. ACS Publications.
Schramm, L. L., & Marangoni, D. G. (2000). Surfactants and their solutions: Basic principles. *Surfactants: Fundamentals and applications in the petroleum industry*, 3-50.
Sharma, M. (2019). *CO2 Mobility Control with Foam for*

Enhanced Oil Recovery and Associated Storage

Multi-scale Approach for Field Application University of Stavanger]. University of Stavanger. https://www.uis.no/sites/default/files/inline-images/uaGYu4WynJ81f3RT3vGx6TMOOPPxoRhAk68MFqeDpQhdJnx3Ns.pdf
Sharma, M., Alcorn, Z., Fredriksen, S., Fernø, M., & Graue, A. (2017). Numerical modelling study for designing CO2-foam field pilot. IOR 2017-19th European Symposium on Improved Oil Recovery,
Sharma, M., Alcorn, Z., Fredriksen, S., Rognmo, A., Fernø, M., Skjæveland, S., & Graue, A. (2020). Model calibration for forecasting CO2-foam enhanced oil recovery field pilot performance in a carbonate reservoir. *Petroleum Geoscience*, *26*(1), 141-149.
Sheng, J. J. (2013). *Enhanced oil recovery field case studies*. Gulf Professional Publishing.
Sihvonen, M., Järvenpää, E., Hietaniemi, V., & Huopalahti, R. (1999). Advances in supercritical carbon dioxide technologies. *Trends in Food Science & Technology*, *10*(6-7), 217-222.
Skea, J., Shukla, P., & Kılkış, Ş. (2022). Climate Change 2022: Mitigation of Climate Change. In: Cambridge University Press, Cambridge (MA), USA.
Skjelsvik, E. B. (2018). *Synergy of Nanoparticles and Surfactants for CO2 Foam Enhanced Oil Recovery and CO2 Storage in Carbonates* The University of Bergen].
Skjæveland, S. M., & Kleppe, J. (1992). SPOR Monograph, Recent advances in improved oil recovery methods for north sea sandstone reservoirs. *Norwegian Petroleum Directorate, Norway*.
Soleimani Zohr Shiri, M., Henderson, W., & Mucalo, M. R. (2019). A review of the lesser-studied microemulsion-based synthesis methodologies used for preparing nanoparticle systems of the noble metals, Os, Re, Ir and Rh. *Materials*, *12*(12), 1896.
Song, Y.-C., Zhu, N.-J., Liu, Y., Zhao, J.-F., Liu, W.-G., Zhang, Y., Zhao, Y.-C., & Jiang, L.-L. (2011). Magnetic resonance imaging study on the miscibility of a CO2/n-decane system. *Chinese Physics Letters*, *28*(9), 096401.
Soyke, A. M. (2020). *Combining Nanoparticles and Surfactants to Stabilize CO2 Foam for CCUS* The University of Bergen].
Verma, M. K. (2015). *Fundamentals of carbon dioxide-enhanced oil recovery (CO2-EOR): A supporting document of the assessment methodology for hydrocarbon recovery using CO2-EOR associated with carbon sequestration*. US Department of the Interior, US Geological Survey Washington, DC.
Wasan, D., Koczo, K., & Nikolov, A. (1994). Mechanisms of aqueous foam stability and antifoaming action with and without oil: a thin-film approach. In. ACS Publications.
Zahasky, C., Kurotori, T., Pini, R., & Benson, S. M. (2019). Positron emission tomography in water resources and subsurface energy resources engineering research. *Advances in water resources*, *127*, 39-52.
Zolotukhin, A. B., & Ursin, J.-R. (2000). *Introduction to petroleum reservoir engineering*. Norwegian Academic Press.

Appendix

A. Differential Pressure Development During WAG and SAG Injection

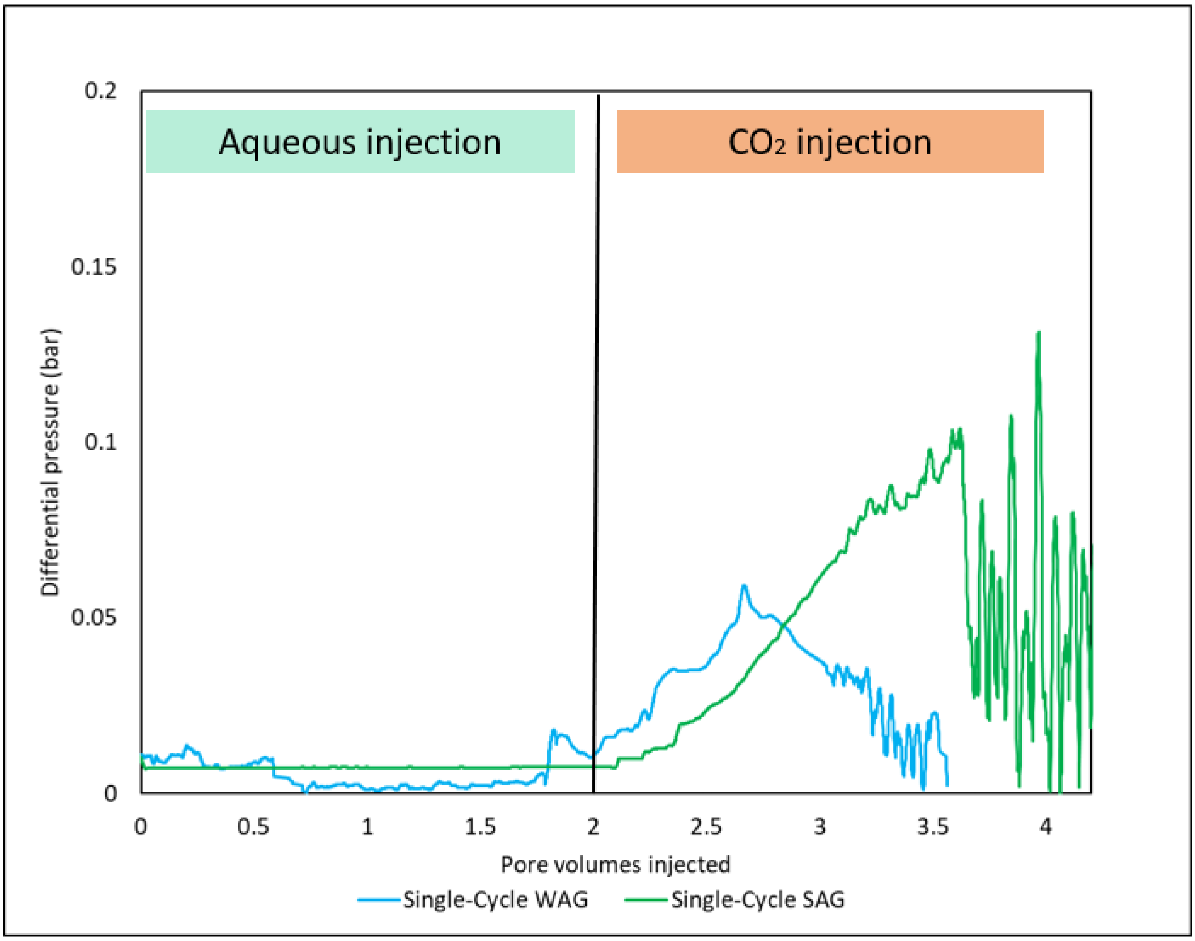

Figure A.1 Differential pressure as a function of pore volumes injected during Single-Cycle WAG (blue curve) and SAG (green curve).

B. Pressure Fluctuations During Steady-State Co-Injection

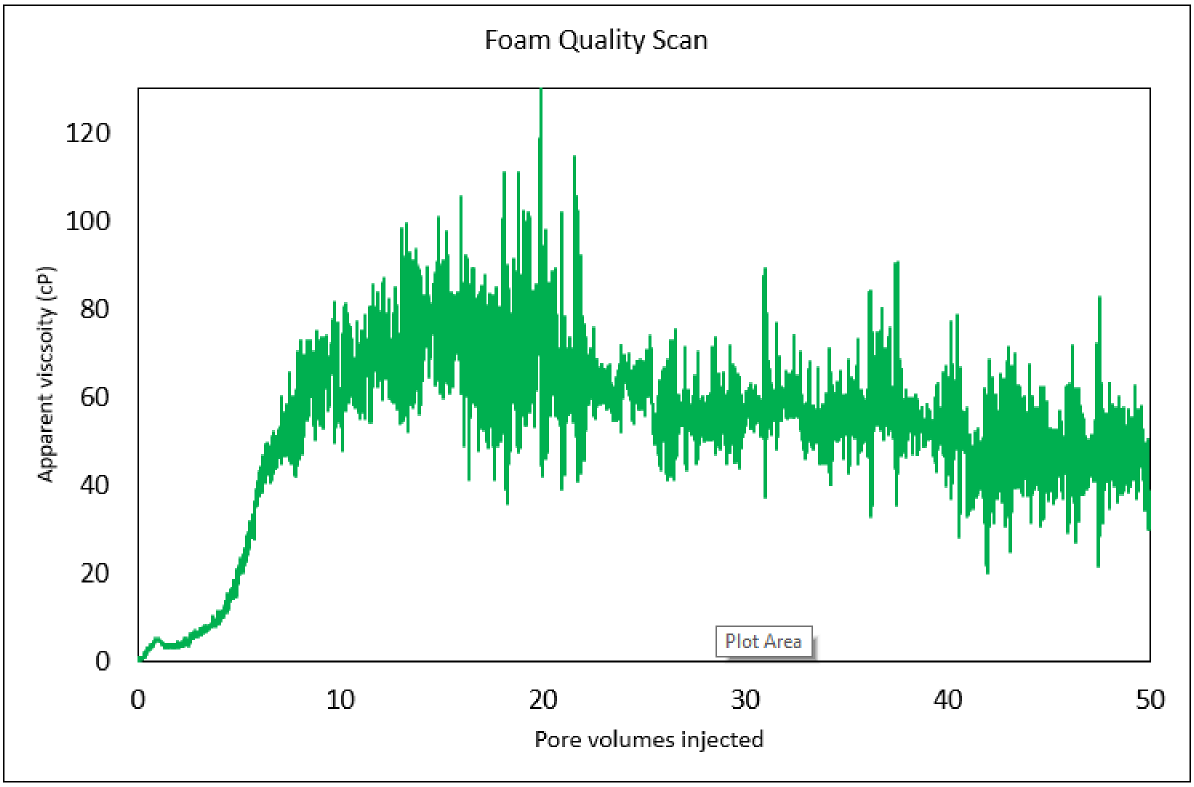

Figure B.1 Apparent viscosity as a function of pore volumes injected during co-injection of foaming solution and CO_2 at different gas fractions. The figure shows the fluctuations in pressure during experiments. Apparent viscosity is a function of the pressure and accurately demonstrates the pressure fluctuations.

C. Numerical Simulation File – Co-injection of Surfactant and CO_2

```
RUNSPEC


--NOSIM


NOECHO


TITLE

HIST CO2 INJECTION AND PILOT WITH POST PILOT INJ


FIELD
```

```
OIL
GAS
WATER

COMPS
6 /

COMPW
2 /

START
1 JAN 2018 /

DIMENS
75 1 54 /

WELLDIMS
5 60 4  5 /

UNIFOUT
UNIFIN

MESSAGES
6* 2* 1000000 1000000 /

UDQDIMS
10 10 5* 10 /

UDQPARAM
```

```
4* /

TABDIMS
3 /

--***********************
GRID

TOPS
75*5360 /

DX
4050*10 /

DY
4050*50 /

DZ
75*7.45
225*3
225*2.44
75*2.49
150*2.36
75*15.71
375*2.94
150*1.83
75*0.08
150*2.88
150*2.86
75*0.03
```

```
150*1.86
75*8.03
150*2.89
150*1.93
75*5.22
150*2.67
150*2.26
150*2.64
75*11.14
300*2.99
75*19.47
450*2.6
75*0.79
75*0.64
75*0.74
75*2.17
/

PORO
75*0
225*0.056
225*0.062
75*0.113
150*0.074
75*0
375*0.109
150*0.188
75*0.11
150*0.132
150*0.094
```

```
75*0.075
150*0.103
75*0
150*0.109
150*0.089
75*0
150*0.104
150*0.129
150*0.044
75*0
300*0.065
75*0
450*0.106
75*0
75*0.016
75*0
75*0.023
/

PERMX
75*0
225*0.1
225*0.1
75*21.6
150*2.5
75*0
375*1.9
150*117.8
75*0.7
150*15.9
```

```
150*1.8

75*0.9

150*0.1

75*0

150*4.7

150*13.8

75*0

150*4.3

150*8.7

150*0

75*0

300*1.1

75*0

450*5.5

75*0

75*1.6

75*0

75*1.3

/


COPY

PERMX PERMY /

PERMX PERMZ /

/


MULTIPLY

PERMZ 0.16  1 75  1 1   1   1 /

PERMZ 0.6   1 75  1 1   2   4 /

PERMZ 0.16  1 75  1 1   5   7 /

PERMZ 0.6   1 75  1 1   8   8 /
PERMZ 0.6   1 75  1 1   9  10 /

PERMZ 0.16  1 75  1 1  11  11 /

PERMZ 0.6   1 75  1 1  12  16 /

PERMZ 0.6   1 75  1 1  17  18 /

PERMZ 0.16  1 75  1 1  19  19 /

PERMZ 0.6   1 75  1 1  20  21 /

PERMZ 0.6   1 75  1 1  22  23 /

PERMZ 0.16  1 75  1 1  24  24 /

PERMZ 0.6   1 75  1 1  25  26 /

PERMZ 0.16  1 75  1 1  27  27 /

PERMZ 0.6   1 75  1 1  28  29 /

PERMZ 0.6   1 75  1 1  30  31 /

PERMZ 0.16  1 75  1 1  32  32 /

PERMZ 0.6   1 75  1 1  33  34 /

PERMZ 0.6   1 75  1 1  35  36 /

PERMZ 0.6   1 75  1 1  37  38 /

PERMZ 0.16  1 75  1 1  39  39 /

PERMZ 0.6   1 75  1 1  40  43 /

PERMZ 0.16  1 75  1 1  44  44 /

PERMZ 0.6   1 75  1 1  45  50 /

PERMZ 0.16  1 75  1 1  51  51 /

PERMZ 0.6   1 75  1 1  52  52 /

PERMZ 0.16  1 75  1 1  53  53 /

PERMZ 0.6   1 75  1 1  54  54 /

/


GRIDFILE

0 1 /


INIT
```

```
--MINPV
--1 /

--MINDZNET
--0.05 /

--RPTGRID
--DX DY DZ PORO PORV /

--***********************
EDIT

--***********************
PROPS

NCOMPS
6 /

EOS
PR /

RTEMP
104 /

STCOND
60   14.696  /

CNAMES
CO2 N2C1 H2SC2C3 C4C5C6 PC1 PC2 /
```

```
TCRIT

547.6 340.6 610.9 827.1 1374.3 1324.7 /


PCRIT

1069.9 663.8 706.3 509.8 323.0 248.9 /


VCRIT

1.506 1.583 2.625 4.719 8.746 19.607 /


MW

44.01 16.29 36.19 70.01 148.24 374.21 /


ACF

0.2250 0.0086 0.1202 0.2278 0.4133 0.9618 /


OMEGAA

6*0.45723553 /


OMEGAB

6*0.077796074 /


SSHIFT

6*0 /


TBOIL

350.5 206.2 395.1 552.2 866.1 1368.1 /


PARACHOR

78.0 76.3 122.3 217.1 416.4 865.8 /
```

```
BIC
0.1029
0.1285  0.0029
0.1156  0.0136  0.0040
0.1001  0.0327  0.0164  0.0044
0.1146  0.0685  0.0447  0.0229  0.0075
/

PEDERSEN

PEDTUNER
0.5120  1.1240  0.9456  0.5832  0.01062 /

DENSITY
1* 62.4 1* /

PVTW
3000 1* 1.6E-6 0.75 /

ROCK
3000 10E-6 /

STONE

SWFN
-- W -> O
0.100    0.000    0
0.101    0.000    0
0.200    0.001    0
```

```
0.235   0.007   0
0.270   0.028   0
0.305   0.063   0
0.340   0.112   0
0.375   0.175   0
0.410   0.252   0
0.445   0.343   0
0.480   0.448   0
0.515   0.567   0
0.550   0.700   0
1.000   1.000   0 /
/
/

SGFN
0.000   0.000   0
0.001   0.000   0
0.050   0.000   0
0.100   0.063   0
0.135   0.106   0
0.170   0.150   0
0.205   0.194   0
0.240   0.238   0
0.275   0.281   0
0.310   0.325   0
0.345   0.369   0
0.380   0.413   0
0.415   0.456   0
0.450   0.500   0
0.583   0.667   0
```

```
0.717   0.833   0
0.850   1.000   0  /
/
/

-- SORG=5%
SOF3
0.000   0.000   0.000
0.050   0.000   0.000
0.183   0.000   0.157
0.317   0.000   0.314
0.450   0.000   0.471
0.485   0.0003  0.512
0.520   0.003   0.553
0.555   0.009   0.594
0.590   0.021   0.635
0.625   0.041   0.676
0.660   0.071   0.718
0.695   0.113   0.759
0.730   0.169   0.800
0.765   0.240   0.841
0.800   0.329   0.882
0.899   0.700   0.999
0.900   1.000   1.000  /
/
/

--SOR
--0.05 /
--0.05 /
```

```
TRACER
GS1 CO2 /
GS2 CO2 /
GS3 CO2 /
WT1 WATER /
WT2 SURFACT /
/

--------------------------------------------

WNAMES
WATER SURFACT /

MWW
18.015 18.015 / SURF PROPERTIES = WATER PROPERTIES (ACTS AS TRACER)

PREFW
2360 2360 /

DREFW
62.4 62.4 /

CREFW
1.6E-6 1.6E-6 /

VREFW
0.75 0.75
0    0    /
```

```
CWTYPE
1* SURFF /

FOAMFRM
--fmmob
0 /
630 /
1200 /

FOAMFSW
--fmdry epdry
0.32 500 /
0.27 100 /
0.22 25 /

FOAMFCN
---fmcap epcap
7.8E-07 0.65 /
7.8E-07 0.65 /
7.8E-07 0.65 /

FOAMFSC
-- lb/stb, ,lb/stb,
0.35 1 0.175 0.20 /
0.35 1 0.175 0.20 /
0.35 1 0.175 0.20 /

FOAMFST
--lb/stb,lbf/in.
0    0.0001616
```

```
3.54  0.0000418 /
0     0.0001616
3.54  0.0000418 /
0     0.0001616
3.54  0.0000418 /

FOAMFSO
0.28 1 /
0.28 1 /
0.28 1 /

__***********************
REGIONS

SATNUM
1 74*1
1 74*1 1 74*1 1 74*1
1 74*1 1 74*1 1 74*1
1 74*2
1 74*1 1 74*1
1 74*1
1 74*1 1 74*1 1 74*1 1 74*1 1 74*1
1 74*3 1 74*3
1 74*1
1 74*2 1 74*2
1 74*1 1 74*1
1 74*1
1 74*1 1 74*1
1 74*1
1 74*1 1 74*1
```

```
1 74*2 1 74*2
1 74*1
1 74*1 1 74*1
1 74*1 1 74*1
1 74*1 1 74*1
1 74*1
1 74*1 1 74*1 1 74*1 1 74*1
1 74*1
1 74*1 1 74*1 1 74*1 1 74*1 1 74*1 1 74*1
1 74*1
1 74*1
1 74*1
1 74*1
/

--**********************
SOLUTION

PRESSURE
4050*3200 /

---SWAT FROM 1 JAN 2018
INCLUDE
SWAT_XSECTION.INC /

SGAS
4050*0 /

ZMF
4050*0.0247 4050*0.2516 4050*0.1863
```

```
4050*0.1277 4050*0.2723 4050*0.1374 /


DATUM

5360 /


RPTRST

'BASIC=2' FOAM FOAMMOB FOAMCNM DENG DENO DENW VGAS VOIL VWAT FLORES PRESSURE
SGAS SOIL SWAT AMF XMF YMF ZMF GS1 /


TBLKGS1

4050*0  /


TBLKWT1

4050*0  /


TBLKGS2

4050*0  /


TBLKWT2

4050*0  /


WMF

4050*1

4050*0

/


__***********************

SUMMARY


RPTONLY
```

```
INCLUDE
'SUMMARYFOAM.INC' /

PERFORMA

COPR
P1 /
/

CGPR
P1 /
/

CWPR
P1 /
/

CWCT
P1 /
/

CGOR
P1 /
/

CGIR
I1G /
I1W /
/
```

WTPRGS1

/

WTPTGS1

/

WTIRGS1

/

WTITGS1

/

CTPRGS1

P1 /

/

CTIRGS1

P1 /

/

WUSCTPT

/

WUSCTPR

/

WTPRWT1

/

WTPTWT1

/

WTIRWT1

/

WTITWT1

/

CTPRWT1

P1 /

/

CTIRWT1

P1 /

/

WTPRGS2

/

WTPTGS2

/

WTIRGS2

/

WTITGS2

/

CTPRGS2

P1 /

/

CTIRGS2

P1 /

/

WTPRWT2

/

WTPTWT2

/

WTIRWT2

/

WTITWT2

/

CTPRWT2

P1 /

/

CTIRWT2

P1 /

/

WTPRGS3

/

WTPTGS3

/

WTIRGS3

/

WTITGS3

/

CTPRGS3

P1 /

/

CTIRGS3

P1 /

/

```
__***********************

SCHEDULE


--TUNING

--1 7 0.5 0.5 2 /

--/

--/


RPTRST

'BASIC=2' FOAM FOAMMOB FOAMCNM DENG DENO DENW VGAS VOIL VWAT FLORES PRESSURE
SGAS SOIL SWAT AMF XMF YMF ZMF GS1 /


WELSPECS

P1   PROD  75  1 5360  OIL /

I1W  WINJ   1  1 5360  WATER /

I1G  GINJ   1  1 5360  GAS /

/


COMPDAT

P1   2*  1  54  OPEN  2*  .725  1*  0  1*  Z /

I1W  2*  1  54  OPEN  2*  .725  1*  0  1*  Z /

I1G  2*  1  54  OPEN  2*  .725  1*  0  1*  Z /

/


--#############################################

WCONINJE

I1W  WATER  SHUT  RESV  1*   0  4000 /

I1G  GAS    OPEN  RESV  1*  18.9  4000 /

/
```

```
WCONPROD

P1  OPEN  RESV  4*  17.7  1000  /

/

--###############################################


WELLSTRE

SOLVENT 1 0 0 0 0 0 /

/


WELLSTRW

WATONLY 1.0 0.0 /

WATSURF 0.995 0.005 / 0.5 WT%

/


WINJGAS

I1G STREAM SOLVENT /

/


WINJW

I1W STREAM WATONLY /

/


--WPIMULT

--I1G 0.002 /

--I1W 0.008 /

--/


DATES

2 JAN 2018 /
```

```
9 JAN 2018 /
/

UDQ
DEFINE WUSCTPT WTPTGS1 P1 / WTITGS1 I1G /
DEFINE WUSCTPR WTPRGS1 P1 / WTITGS1 I1G /
/

WTRACER
I1G GS1 0.0015 /
/

DATES
10 JAN 2018 /
/

WTRACER
I1G GS1 0 /
/

DATES
11 JAN 2018 /
15 JAN 2018 /
 1 FEB 2018 /
15 FEB 2018 /
28 FEB 2018 /
/

--############# L14: WATER INJ ############
WCONINJE
```

```
I1W  WATER  OPEN  RESV  1*   17  4000 /
I1G  GAS    SHUT  RESV  1*    0  4000 /
/

WCONPROD
P1  OPEN  RESV  4*  10.8  1000  /
/
--############################################

DATES
 1 MAR 2018 /
 2 MAR 2018 /
/

--############## L14: WATER INJ (LOWER RATE) #############
WCONINJE
I1W  WATER  OPEN  RESV  1*   9.5  4000 /
I1G  GAS    SHUT  RESV  1*   0    4000 /
/
--############################################

DATES
 3 MAR 2018 /
 5 MAR 2018 /
15 MAR 2018 /
 1 APR 2018 /
15 APR 2018 /
 1 MAY 2018 /
15 MAY 2018 /
 1 JUN 2018 /
```

```
15 JUN 2018 /
 1 JUL 2018 /
 18 JUL 2018 /
/

--############# L14: HIST CO2 INJ (JULY 19 2018 - NOV 20 2018) ##############
WCONINJE
I1W  WATER  SHUT  RESV  1*   0   4000 /
I1G  GAS    OPEN  RESV  1*   18.9 4000 /
/

WCONPROD
P1  OPEN  RESV  4*  17.7  1000  /
/
--#########################################

DATES
 19 JUL 2018 /
 2 AUG 2018 /
 3 AUG 2018 /
 5 AUG 2018 /
10 AUG 2018 /
 1 SEP 2018 /
 1 OCT 2018 /
 1 NOV 2018 /
 20 NOV 2018 /
/

--########### L14: HIST WATER INJ (22 NOV 2018 -  22 DEC 2018) ############
WCONINJE
```

```
I1W  WATER  OPEN  RESV  1*   17  4000 /
I1G  GAS    SHUT  RESV  1*   0    4000 /
/

UDQ
DEFINE WUSCTPT WTPTWT1 P1 / WTITWT1 I1W /
DEFINE WUSCTPR WTPRWT1 P1 / WTITWT1 I1W /
/


WTRACER
I1W WT1 1 /
/

DATES
21 NOV 2018 /
/

WTRACER
I1W WT1 0 /
/

DATES
22 NOV 2018 /
/

DATES
 25 NOV 2018 /
 30 NOV 2018 /
 1 DEC 2018 /
 22 DEC 2018 /
/


--############ L14: HIST WATER INJ (22 DEC 2018 - 4 APRIL 2019 LOW RATE) #############
WCONINJE
I1W  WATER  OPEN  RESV  1*   9.5  4000 /
I1G  GAS    SHUT  RESV  1*   0    4000 /
/



DATES
 23 DEC 2018 /
 1  JAN 2019 /
 1  FEB 2019 /
 28 FEB 2019 /
 1  MAR 2019 /
 30 MAR 2019 /
 4  APR 2019 /
/




--############ L14: HIST WATER INJ (4 APRIL 2019 - 22 APR 2019 HIGH RATE) #############
WCONINJE
I1W  WATER  OPEN  RESV  1*   20  4000 /
I1G  GAS    SHUT  RESV  1*   0    4000 /
/


DATES
 5 APR 2019 /
 12 APR 2019 /
 21 APR 2019 /
/

--############# L14: HIST CO2 INJ (22 APR 2019 - 21 MAY 2019) ##########
WCONINJE
I1W  WATER  SHUT  RESV  1*   0    4000 /
I1G  GAS    OPEN  RESV  1*   9.5  4000 /
/

DATES
 22 APR 2019 /
 24 APR 2019 /
 1 MAY 2019 /
 21 MAY 2019 /
/

--############ L14: HIST WATER INJ (1000 BBL INJ BEFORE PILOT MAY 22 2019) #############
WCONINJE
I1W  WATER  OPEN  RESV  1*   18  4000 /
I1G  GAS    SHUT  RESV  1*   0    4000 /
/

DATES
22 MAY 2019 /
/
--------------------------------------------------------------------------------

--############# PILOT ##########
-- ### 183 DAYS OF CO-INJECTION OF SURFACTANT AND CO2 WITH FOAM QUALITY 60% ###
-- ### XXX DAYS OF CO2 INJECTION
--######### HM RUN: OBS RATE CONVER = 0.027 BASED UPON XSECTION PV #########


WCONHIST
---------CTRL  OIL   WATER  GAS
P1 OPEN LRAT  0.70  9.23   24.70  /
/


WCONINJH
I1W  WATER  OPEN  3.69  3646 6* RATE /
I1G  GAS    OPEN  14.98  3218 6* RATE /
/

WELLSTRE
SOLVENT 1 0 0 0 0 0 0 /
/

WELLSTRW
WATONLY 1.0 0.0 /
WATSURF 0.995 0.005 / 0.5 WT%
/

WINJW
I1W STREAM WATSURF /
/

WINJGAS
I1G STREAM SOLVENT /
```

```
/

-- ### CO2 TRACER GS2)

UDQ
DEFINE WUSCTPT WTPTGS2 P1 / WTITGS2 I1G /
DEFINE WUSCTPR WTPRGS2 P1 / WTITGS2 I1G /
/

WTRACER
I1G GS2 0.0015 /
/

DATES
23 MAY 2019 /
/

WTRACER
I1G GS2 0 /
/

DATES
24 MAY 2019 /
/

TSTEP
3*3 /


TSTEP
```

1 3*3 /

TSTEP

1 3*3 /

TSTEP

1 3*3 /

TSTEP

1 3*3 /

TSTEP

1 3*3 /

TSTEP

1 3*3 /

TSTEP

1 3*3 /

TSTEP

1 3*3 /

```
TSTEP

1 1 3*2 /



TSTEP

1 1 1 /



TSTEP

1 3*3 /


TSTEP

24*3 1/



-- ######### START OF PURE CO2 INJECTION #########

-- ### CO2 INJECTION USED HISTORY MATCHED INJECTION RATES ###


-- ##### 20 DAYS CO2 ##### --CO2 TRACER GS2


WCONHIST

---------CTRL OIL   WATER   GAS

P1 OPEN LRAT 0.57   9.28   21.70 /

/


WCONINJH

I1W  WATER  SHUT  9.83  3646 6* RATE /

I1G  GAS    OPEN  23.86  3574 6* RATE /

/
```

```
TSTEP
1 1 6*3 /



-- ##### 20 DAYS CO2 #####

WCONHIST
---------CTRL OIL   WATER  GAS
P1 OPEN LRAT 0.34  3.82   8.82 /
/

WCONINJH
I1W  WATER  SHUT  9.83  3646 6* RATE /
I1G  GAS    OPEN  20.69  3469 6* RATE /
/

-- ### REMOVED 3 SLUGS + 13 DAYS

TSTEP
2*3 1/



-- ##### 20 DAYS CO2 #####

WCONHIST
---------CTRL OIL   WATER  GAS
```

```
P1 OPEN LRAT 0.27  3.12   6.53 /
/

WCONINJH
I1W  WATER  SHUT  9.83  3646 6* RATE /
I1G  GAS    OPEN  23.22  3560 6* RATE /
/

TSTEP
1 6*3 1 /



-- ##### 10 DAYS CO2 #####

WCONHIST
---------CTRL OIL   WATER  GAS
P1 OPEN LRAT 0.37  3.59   8.37 /
/

WCONINJH
I1W  WATER  SHUT  9.83  3646 6* RATE /
I1G  GAS    OPEN  21.55  3505 6* RATE /
/

TSTEP
3*3 1 /
```

```
-- ##### 10 DAYS CO2 #####

WCONHIST
---------CTRL OIL   WATER  GAS
P1 OPEN LRAT 0.37  3.59   8.37 /
/

WCONINJH
I1W  WATER  SHUT  9.83  3646 6* RATE /
I1G  GAS    OPEN  21.55  3505 6* RATE /
/

TSTEP
1 3*3 /



-- ##### 20 DAYS CO2 #####

WCONHIST
---------CTRL OIL   WATER  GAS
P1 OPEN LRAT 0.23  3.60   7.70 /
/

WCONINJH
I1W  WATER  SHUT  9.83  3646 6* RATE /
I1G  GAS    OPEN  23.12  3378 6* RATE /
/

TSTEP
```

```
1 6*3 1 /



-- ##### 7 DAYS CO2 #####

WCONHIST
---------CTRL OIL   WATER  GAS
P1 OPEN LRAT 0.35  3.60   8.70 /
/

WCONINJH
I1W  WATER  SHUT  9.83  3646 6* RATE /
I1G  GAS    OPEN 23.34  3218 6* RATE /
/

TSTEP
1 2*2 1 1/



-- ##### 13 DAYS CO2 #####

WCONHIST
---------CTRL OIL   WATER  GAS
P1 OPEN LRAT 0.35  3.60   8.70 /
/

WCONINJH
```

```
I1W  WATER  SHUT  9.83  3646 6* RATE /

I1G  GAS    OPEN 23.34  3218 6* RATE /

/


TSTEP

1 5*2 1 1/



-- ##### 20 DAYS CO2 #####


WCONHIST

---------CTRL OIL   WATER  GAS

P1 OPEN LRAT 0.35  3.60   8.70 /

/


WCONINJH

I1W  WATER  SHUT  9.83  3646 6* RATE /

I1G  GAS    OPEN 23.34  3218 6* RATE /

/


TSTEP

1 6*3 1 /




-- ##### 20 DAYS CO2 ##### -- CO2 TRACER GS3


WCONHIST

---------CTRL OIL   WATER  GAS

P1 OPEN LRAT 0.35  3.60   8.70 /
```

```
/

WCONINJH
I1W  WATER  SHUT  9.83  3646 6* RATE /
I1G  GAS    OPEN 23.34  3218 6* RATE /
/

UDQ
DEFINE WUSCTPT WTPTGS3 P1 / WTITGS3 I1G /
DEFINE WUSCTPR WTPRGS3 P1 / WTITGS3 I1G /
/

WTRACER
I1G GS3 0.0015 /
/

TSTEP
1 /

WTRACER
I1G GS3 0 /
/

TSTEP
1 /


TSTEP
6*3 /
```

```
--############# POST PILOT ##### --

--############# P1: VRR - 1 ##############

WCONPROD
P1  OPEN  RESV  4*  17.7  1000  /
/

WINJW
I1W STREAM WATONLY /
/

--## 14 DAYS WATER ##--
WCONINJH
I1W  WATER  OPEN  9.83  3346 6* RATE /
I1G  GAS    SHUT 23.34  3218 6* RATE /
/

TSTEP
1 1 7*2 /

--## 14 DAYS CO2 ##--
WCONINJH
I1W  WATER  SHUT 9.83  3346 6* RATE /
I1G  GAS    OPEN 23.34  3218 6* RATE /
/

TSTEP
```

```
1 1 7*2 /



--## 90 DAYS WATER ##--
WCONINJH
I1W  WATER  OPEN  9.83  3346 6* RATE /
I1G  GAS    SHUT 23.34  3218 6* RATE /
/

TSTEP
1 116*1 1/



--## 365 DAYS WATER ##--
WCONINJH
I1W  WATER  OPEN  9.83  3346 6* RATE /
I1G  GAS    SHUT 23.34  3218 6* RATE /
/

TSTEP
1 363*1 /



END
```